UNIVERSITY OF ALBERTA

Interaction of Picosecond KrF Laser Pulses with Gas Target Plasma

by ©

Yanmin Li

A thesis submitted to Faculty of Graduate Studies and Research
in partial fulfillment of the requirements for the degree of
Doctor of Philosophy

Department of Electrical Engineering

Edmonton, Alberta

Fall, 1995

National Library
of Canada

Acquisitions and
Bibliographic Services

395 Wellington Street
Ottawa ON K1A 0N4
Canada

Bibliothèque nationale
du Canada

Acquisitions et
services bibliographiques

395, rue Wellington
Ottawa ON K1A 0N4
Canada

Your file Votre référence

Our file Notre référence

The author has granted a non-exclusive licence allowing the National Library of Canada to reproduce, loan, distribute or sell copies of this thesis in microform, paper or electronic formats.

The author retains ownership of the copyright in this thesis. Neither the thesis nor substantial extracts from it may be printed or otherwise reproduced without the author's permission.

L'auteur a accordé une licence non exclusive permettant à la Bibliothèque nationale du Canada de reproduire, prêter, distribuer ou vendre des copies de cette thèse sous la forme de microfiche/film, de reproduction sur papier ou sur format électronique.

L'auteur conserve la propriété du droit d'auteur qui protège cette thèse. Ni la thèse ni des extraits substantiels de celle-ci ne doivent être imprimés ou autrement reproduits sans son autorisation.

0-612-22153-9

Canada

University of Alberta

Release Form

Name of Author:	Yanmin Li
Title of Thesis:	Interaction of Picosecond KrF Laser Pulses With Gas Target Plasma
Degree:	Doctor of Philosophy
Year This Degree Granted:	1995

Permission is hereby granted to the University of Alberta to reproduce single copies of this thesis and to lend or sell such copies for private, scholarly or scientific research purpose only.

The author reserves all other publication and other rights in association with the copyright in the thesis, and except as hereinbefore provided neither the thesis nor any substantial proportion thereof may be printed or otherwise reproduced in any material form without the author's written permission.

Department of Electrical Engineering
University of Alberta
Edmonton, Alberta
T6G 2G7
Canada

25 June 1995

UNIVERSITY OF ALBERTA

FACULTY OF GRADUATE STUDIES AND RESEARCH

The undersigned certify that they have read, and recommended to the Faculty of Graduate Studies and Research for acceptance, a thesis entitled **Interaction of Picosecond KrF Laser Pulses with Gas Target Plasma** submitted by Yanmin Li in partial fulfillment of the requirements for the degree of Doctor of Philosophy.

Robert Fedosejevs
Dr. R. Fedosejevs

A Offenberger
Dr. A. A Offenberger

J N McMullin
Dr. J. N. McMullin

Dr. W. Rozmus

J. Meyer
Dr. J. Meyer

Abstract

A comprehensive study of the formation of high density plasma columns by means of above threshold ionization of gaseous medium and the propagation of ultrashort KrF laser pulses through such plasmas has been carried out. A first series of experiments studied the absorption and scattering of 6 ps laser pulses and the size and shift in the breakdown region as a function of incident energy in static gas. The results from time resolved shadowgraphy were in agreement with multiphoton ionization initiated breakdown with subsequent collisional ionization and evolution of a 400-900 μm long cylindrical blast wave channel. Refraction of the laser pulses was identified as a limitation to achieving high intensity at the focus and obtaining long plasma channels. Subsequent experiments were carried out with 1 ps duration KrF laser pulses together with a gas jet target which had allowed the study of high intensity interaction in a new regime where $\upsilon_{osc}/\upsilon_{th} > 1$ at electron densities of up to 0.1 n_c and laser intensities up to 10^{17} W/cm^2. An autocorrelator was developed to characterize the KrF laser pulse duration using the visible as opposed to UV fluorescence of BaF_2 for the first time. A high density gas jet was developed and characterized for the target experiments. Gas densities of up to 6×10^{20} cm^{-3} at a distance of 200 μm above the nozzle tip were obtained. The refraction of the laser pulse was measured using CCD camera imaging. The asymptotic refraction angles of the laser beam through helium and nitrogen gas jets were determined as a function of gas pressure. The transmitted KrF laser radiation in helium, neon, argon and nitrogen gas jets was characterized in terms of the energy transmission within an F/2.5 cone angle and the ionization induced blue shifted spectra were measured systematically for the first time for such high intensities and gas densities. He II emission at 468.5 nm and UV laser side scattering were also used to study the propagation of high intensity KrF laser pulse through high density helium gas jet.

Acknowledgment

It has been a great privilege for me to work and study under the guidance of Dr. Robert Fedosejevs for the past five and half years. I would like to thank him for his advice and encouragement during the course of thesis project. His enthusiasm and dedication to science always inspire me to strive for excellence.

I am very grateful to Dr. Allan Offenberger for allowing me to conduct some experiments using the e-beam pumped KrF laser facility and many valuable discussion and suggestions. I would also like to thank Drs. C. Capjack, W. Rozmus, N. H. Burnett for many interesting ideas and discussions, and my dissertation committee for a thorough reading of the thesis and for many useful suggestions.

I have greatly benefited from the excellent technical assistance of Blair Harwood and Alois Haromy. Thanks also go to Drs. R. Bobkowski, P. Naik, Y. Y. Tusi, D. Vick, J. Broughton, M. Fujita, X. Sun and fellow graduate students Jin Li, Baolian Xu, Bing Shen, Qing Ji, C. Kam, R. Tam, R. Newton, and Yunlei Li for your kind help to make my stay in Edmonton enjoyable.

Finally, I thank my mother and my later father for their love, encouragement and support to make it possible for me to pursue studies all the way along. Special thanks go to my wife Dr. Qinyue Liu for her love, understanding, and support for tolerating many long and late working hours. Our adorable daughter, Lucy, has brought us much joy. I am in debt to her for putting up with being staying away from us in order for me to concentrate and finish my study.

Table of Contents

Chapter

1. Introduction **1**

1.1 Introduction and Motivation 1
1.2 Objective of Present Thesis 5

Bibliography 8

2. Theory **10**

2.1 XUV and X-ray lasers 10
2.2 Multiphoton ionization 14
2.3 Heating of electrons 18

2.3.1 ATI heating 18
2.3.2 Ponderomotive force and heating 21
2.3.3 Inverse Bremsstrahlung at high intensities 23
2.3.4 Refraction and self-focusing 26
2.3.5 Ionization induced blueshift 28

Bibliography 30

3. General Experimental Methods and Instrumentation **34**

3.1 Outline of the experiments 34

3.1.1 Visible single-shot two-photon autocorrelator of KrF laser pulse in BaF_2 34
3.1.2 Multiphoton ionization formed plasma columns in a static fill gas cell. 34
3.1.3 Characterization of a high density gas jet 35
3.1.4 Laser plasma interaction in high density gas jet 35

3.2 Picosecond laser facility 38
3.3 Laser diagnostics 42
3.4 Target Chamber and Diagnostics 43

Bibliography 44

4. A Visible Femtosecond Single Shot Autocorrelator in BaF_2 for KrF Lasers 47

4.1 Visible single shot autocorrelator in BaF_2 48
4.2 Two photon absorption coefficient in BaF_2 51

Bibliography 54

5. Formation of Plasma Columns in Atmospheric Pressure Gases by Picosecond KrF Laser 61

5.1 Introduction 61
5.2 Experimental details 64
5.3 Experimental results 68

5.3.1 Breakdown thresholds 68
5.3.2 Absorption and scattering 70
5.3.3 Axial behavior 71
5.3.4 Radial Expansion 74

5.4 Discussion 74

5.4.1 Breakdown, Ionization and Heating 74
5.4.2 Refraction 81
5.4.3 Blast Wave 83

5.5 Conclusions 84

Bibliography 85

6. Density Measurements of a High Density Pulsed Gas Jet for Laser Plasma Interaction Studies 96

Bibliography 104

7. Propagation of Ultrashort Intense Pulse through High Density Gas Jet 112

7.1 Introduction 112
7.2 Experimental details 113
7.3 Laser beam profile 114
7.4 Refraction 115
7.5 Visible emission and UV side scattering 119
7.6 Spectral diagnostics of beam propagation 123
7.7 Energy transmission 126
7.8 Discussion 127

Bibliography 131

8. **Ionization Induced Blue-shifting of KrF Laser Pulse in Underdense Plasma** **157**

8.1 Introduction 157
8.2 Experimental setup 159
8.3 Experimental results 160
8.4 Discussion 162

Bibliography 165

9. **Numerical Modeling Calculations** **173**

9.1 Refraction 173
9.2 Numerical ionization modeling code 178

Bibliography 187

10. **Conclusion** **203**

List of Tables

Table 2-1 ATI heating for ionization rates of 10^{12}, 10^{13}, and 10^{14} s^{-1} and ionization energies of 10 to 200 eV calculated for a laser wavelength of 0.25 μ m 20

Table. 5-1 Breakdown thresholds for argon, air, and helium. (Intensities in units of Wcm^{-2}, $h\nu = 5.0$ eV) 70

Table. 9-1 Parameters of a power law fit to the ionization potentials of the outer shell electrons for the various gases. 176

List of Figures

Fig. 2-1 Energy levels for simple three level model 32
Fig. 2-2 Multiphoton Ionization 32
Fig. 2-3 Potential barrier suppression and electron tunneling 33
Fig. 3-1 Picosecond KrF front end laser system 45
Fig. 3-2 Electron beam pumped KrF laser amplifiers 46
Fig. 4-1 Measured spectrum of two-photon excited fluorescence from BaF_2 56
Fig. 4-2 Dependence of the BaF_2 fluorescence at 400 nm on the exciting laser intensity. The solid line is a least squares best fit with a slope of 1.98 ± 0.05 57
Fig. 4-3 Layout of the autocorrelator used for two photon pulse width measurements of KrF laser pulses 58
Fig. 4-4 Oscilloscope display of a measured autocorrelation trace. The measured full width of the fluorescence signal is 1.2 ps, yielding a pulsewidth of 850 fs assuming a Gaussian pulse shape 59
Fig. 4-5 A fluorescence trace across the BaF_2 crystal irradiated from one side with a KrF laser pulse 60
Fig. 5-1 Schematic diagram of experimental layout 87
Fig. 5-2 Fractional energy loss of the laser beam in the plasma columns: (a) absorption in argon and air and combined absorption and scattering in argon and air; (b) absorption in helium and combined absorption and scattering in helium. 88
Fig. 5-3 Beam profile in vacuum (a) and scattered radiation in argon (b) recorded on UV sensitive paper at the position of calorimeter C2 for 5 shots at an average energy of E_{in}=5.0 mJ 89
Fig. 5-4 Shadowgrams of the plasma columns: (a) energy E_{in}=1.2 mJ and probe time t_p=0.5 ns, (b) E_{in}=3.4 mJ and t_p=2 ns,and (c) E_{in}=4.5 mJ t_p=3.9 ns. The geometrical focal point is at the right hand edge of the image. 90
Fig. 5-5 Outlines of the argon plasma at times of 0.5 ns, 2 ns and 3.9 ns (solid lines from inside to outside respectively) for an input energy of 3.3 mJ. Also shown are isointensity contours at levels of 2%, 3%, 5%, 10%, and 50% of peak intensity (dashed lines from outside to inside). 91
Fig. 5-6 Shadowgram of the breakdown plasma in helium for an input energy of 7.3 mJ at a probe time of 90 ps. The geometric focal point is 100 μm in from the right hand edge of the image -6 92
Fig. 5-7 Motion of the plasma column as a function of input energy determined from shadowgrams taken at 0.7 ns. Marked are the 93

front edge (closest to the focussing lens), middle point (thickest part of the plasma), and back edge. The solid line through the open circles is a least squares fit to the data proportional to $E_{in}^{1/2}$ corresponding to a constant breakdown threhold intensity. The other solid lines are visual fits to the data

Fig. 5-8 Schematic diagram of refraction from a plasma column of length L. The electron density, n_e, and refractive index, n_r, profiles are also shown across the plasma column 94

Fig. 5-9 Radius of the evolving argon plasma for an incident laser enrgy of 3.3 mJ at times of 0.5, 2.0 and 3.9 ns at two axial positions: at the geometric focal position and 300 mm towards the laser from the geometric focal point. 95

Fig. 6-1 Schematic diagram of gas jet solenoid and nozzle tip 106

Fig. 6-2 (a). Schematic diagram of the wave front shearing interferometer using a wedged quartz plate. The image is viewed by a vidicon camera, VID. (b). Typical interferogram obtained at a time of $t_0 = 10$ ms after the start of the solenoid pulse for nitrogen gas at a reservoir pressure of 104 bar. 107

Fig. 6-3 Time dependence of the fringe shifts observed at a distance of 0.2 mm from the tip of the nozzle for times of 0 to 25 ms after the start of the solenoid pulse for nitrogen gas at a reservoir pressure of 56 bar. 108

Fig. 6-4 (a). Spatial profiles of gas jet density for nitrogen at a reservoir pressure of 104 bar. (b). Corresponding contour plot of density. The contour pressures are given in bars. The dashed line outlines the region where the density falls off to half of the peak value on axis 109

Fig. 6-5 Axial pressures of the nitrogen gas jet as a function of the distance from the nozzle tip for reservoir pressures of 15, 29, 56, and 104 bar of nitrogen respectively and for helium gas jet at a reservoir pressure of 104 bar. The full curves are exponential profiles which have been fit to the data as discussed in the text 110

Fig. 6-6 Dependence of gas jet pressure on the reservoir pressure at seven different positions from the tip of nozzle. These are 120 μm, 320 μm, 520 μm, 820 μm, 1020 μm, 1520 μm, and 2020 μm away from the nozzle tip 111

Fig. 7-1 Experimental setup for beam propagation study 132

Fig. 7-2 Laser beam profile passing focus in vacuum 133

Fig. 7-3 Plot of peak vacuum intensity vs. position through gas jet region 134

Fig. 7-4 Radial density profile at a distance of Z=300 μm above nozzle tip 135

Fig. 7-5 Focusing and imaging geometries 136

Fig. 7-6 Beam spots at the center of the gas jet for helium as a function of neutral density when the laser beams were focused at the center of the gas jet. (a) 49, (b) 32, (c) 16, (d) 6.5, (e) 3.2 times 10^{19} cm^{-3}, and (f) vacuum. 137

Fig. 7-7 Beam spots at the exit of the gas jet for helium as a function of neutral density when the laser beams were focused at the center of the gas jet. (a) 49, (b) 32, (c) 16, (d) 6.5, (e) 2.3 times 10^{19} cm^{-3}, and (f) vacuum. 138

Fig. 7-8 Refractive beam diameters as a function of density for helium when a laser beam is focused at the center of the jet for imaging center and exit 139

Fig. 7-9 Geometry of asymptotic refracted angle 140

Fig. 7-10 Asymptotic refractive angle as a function of atomic density for helium when a laser beam is focused at the center of the jet for imaging center and exit. The dashed line is the theoretical prediction using Eqn. 7-1. 141

Fig. 7-11 Beam spots at the exit of the gas jet for helium as a function of neutral density when the laser beams were focused at the exit of the gas jet. A ring-shaped structure is developed at the density of 4.9×10^{20} cm^{-3}. (a) 49, (b) 32, (c) 16, and (d) 8.1 times 10^{19} cm^{-3}. 142

Fig. 7-12 Refractive beam diameters as a function of density for helium when imaging exit for a laser beam is focused at the exit and center 143

Fig. 7-13 Beam spots at the exit of the gas jet for nitrogen as a function of neutral density when the laser beams were focused at the entrance of the gas jet. (a) 4.5 and (b) 16 10^{19} cm^{-3}. 144

Fig. 7-14 Beam spots at the exit of the gas jet for nitrogen as a function of neutral density when the laser beams were focused at the center of the gas jet. (a) 49, (b) 32, (c) 6.5, (d) 2x attenuated in vacuum, and (e) vacuum. 145

Fig. 7-15 Beam spots at the exit of the gas jet for nitrogen as a function of neutral density when the laser beams were focused at the exit of the gas jet. (a) 49, (b) 32, (c) 9.7, (d) 8.1, (e) 3.1 times 10^{19} cm^{-3}, and (f) 10x attenuated in vacuum. 146

Fig. 7-16 Refractive beam diameters as a function of density for nitrogen when imaging at exit for a laser beam focusing at front, center, and exit 147

Fig. 7-17 Asymptotic refractive angle as a function of density for nitrogen when imaging at exit for a laser beam focusing at front, center, and exit 148

Fig. 7-18 Plasma channel in helium of density of 4.9×10^{20} cm^{-3} imaged by He II line at 468.5 nm (bottom image) and the corresponding UV laser light side scattering (top image) for a laser pulse of peak intensity of 1x 10 17 W/cm^2 with a clean pulse. Two images have the same dimensions. For each image the horizontal and vertical dimensions are identical 149

Fig. 7-19 Plasma channel in helium of density of 4.9×10^{20} cm^{-3} imaged by He II line at 468.5 nm (bottom image) and the corresponding UV laser light side scattering (top image) for a laser pulse of peak intensity of $1\text{x } 10^{17}$ W/cm^2 with a small prepulse of 18 % of energy 150 of the main pulse. The two images have the same dimensions. For each image the horizontal and vertical dimensions are identical

Fig. 7-20 Plasma channel in helium (bottom image) of density of 4.9×10^{20} cm^{-3} imaged by He II line at 468.5 nm and the corresponding UV laser light side scattering (top image) for a laser pulse of peak intensity of 1×10^{17} W/cm^2 with an ASE prepulse of 35% of energy of the main pulse. Two images have the same dimensions. For each image the horizontal and vertical dimensions are identical 151

Fig. 7-21 He II emission spectra at 135, 90, and 0 degrees with a density of 4.9×10^{20} cm^{-3} for an intensity of 1×10^{17} W/cm^2 imaged at the entrance, center, and exit of the gas jet respectively 152

Fig. 7-22 He II spectra at the exit of the gas jet viewed at 0 degree. Enhanced He II at 468.5 nm with elongated plasma column vs. weak He II emission and He I emission (at 471.3 nm) with short plasma column at density of 4.9×10^{20} cm^{-3} and intensity of 1×10^{17} W/cm^2. 153

Fig. 7-23 Plasma channels in helium at density of 4.9×10^{20} cm^{-3} corresponding to the two spectra in Fig. 7-22. The top (a) and bottom (b) images have ASE prepulses of 35% and 20% of energy of the main pulse. 154

Fig. 7-24 He II emission spectra at the exit of the gas jet viewed at 0 degrees at densities of 4.9×10^{20} cm^{-3} ,3.7×10^{20} cm^{-3} , 2.2×10^{20} cm^{-3} for an intensity of 1×10^{17} W/cm^2 155

Fig. 7-25 Energy transmission of KrF laser pulses through He, Ne, N_2, and Ar as a function of density. Note that it is molecular density for N_2. 156

Fig. 8-1 Experimental setup for blueshifting measurement 166

Fig. 8-2 Blue shifted spectra in He as a function of gas density at a vacuum intensity 8×10^{16} W/cm^2. The top three curves also show their 5 times magnified curves of each. 167

Fig. 8-3 Blue shifted spectra in Ne as a function of density at a vacuum intensity 8×10^{16} W/cm^2. 168

Fig. 8-4 Blue shifted spectra in N_2 as a function of density at a vacuum intensity 8×10^{16} W/cm^2. The top two curves also show their 5 times magnified curves of each. 169

Fig. 8-5 Blue shifted spectra in Ar as a function of density at a vacuum intensity 8×10^{16} W/cm^2. The top five curves also show their 5 times magnified curves of each. 170

Fig. 8-6 Blue shifted spectra with a beam stop for He as a function of density at a vacuum intensity 8×10^{16} W/cm^2. The bottom curve is 10 times attenuated 171

Fig. 8-7 Blue shifted spectra with a stop for N_2 as a function of molecular density at a vacuum intensity 1×10^{17} W/cm^2. The bottom curve is 10 times attenuated 172

Fig. 9-1 Beam radius calculated as a function of axial position for a laser power of P=0.2 TW in a nitrogen gas jet target with peak atomic densities of (a) 5×10^{20} cm^{-3}, (b) 2×10^{20} cm^{-3}, and (c)1×10^{20} cm^{-3}. 189

The outline of the gas jet density profile is also shown at the bottom of each plot for reference.

Fig. 9-2 Calculated peak intensities as a function of atomic gas jet density for (a) helium, (b) nitrogen, (c) neon, and (d) argon. Also shown are the vacuum intensity (dotted line) and the peak intensity which would be achieved in a static gas target (dashed line). 190

Fig. 9-3 Comparison of experimentally measured diameters of the outer refraction ring at the exit of the gas jet (solid symbols) with the calculated diameters (lines) for (a) He and (b) N_2. 191

Fig. 9-4 Contour plot of average charge state as a function of position in the laser frame of reference in nitrogen gas for (a) ATI ionization based on Ammosov's rates and (b) the threshold ionization potential given by Eqn. 9.5. Intensity contours for the laser pulse are also superimposed in (a). The peak intensity is 3x10^{16} W/cm^{2} at 1500 fs and the half intensity radius is 15 μm. Each contour represents a step of 0.1 in ionization stage. 192

Fig. 9-5 Geometry of 1D simulation. (a) density profile and (b) beam profile. 193

Fig. 9-6 Spectral blueshift for helium as a function of time for a density of 5x10^{19} cm^{-3} and laser powers of (a) 0.025 TW and (b) 0.25 TW. Also shown is the input laser power and the laser power after absorption. 194

Fig. 9-7 Distribution of ionization states and electron temperature across the gas jet for helium at a peak density of 5x10^{19} cm^{-3} for peak vacuum powers of (a) 0.025 TW and (b) 0.25 TW. 195

Fig. 9-8 Blue shifted spectrum for helium at a density of 5x10^{19} cm^{-3} for peak powers of (a) 0.025 TW and (b) 0.25 TW. Also shown is the input beam spectrum.). 196

Fig. 9-9 Spectral blueshifts for He, N_2, Ne, and Ar as a function of time for a laser power of 0.2 TW at gas densities of (a) 5x10^{19} cm^{-3} and (b) 5x10^{20} cm^{-3}. Note that for N_2 it is molecular gas density. Also shown is the input power and the output laser power after absorption. Beam profiles calculated using the refraction model are used in these calculations. 197

Fig. 9-10 Distribution of ionization states and electron temperature across the gas jet for laser power of 0.2 TW at densities of (a) 5x10^{19} cm^{-3} and (b) 5x10^{20} cm^{-3} for He, N_2, Ne and Ar respectively. 198

Fig. 9-11 Blue shifted spectrum for a laser power of 0.2 TW at densities of (a) 5x10^{19} cm^{-3} and (b) 5x10^{20} cm^{-3} for He, N_2, Ne and Ar respectively. Also shown is the input beam spectrum. 199

Fig. 9-12 Calculated energy transmission of KrF laser pulses through He, Ne, N2, and Ar as a function of density using the experimentally measured beam profile as shown in Fig. 7-2 for a laser power of 0.02 TW (i.e. an effective intensity 10 times reduced form the vacuum intensity). Also shown are the measured transmission data as in Fig. 7-25. Note that for nitrogen the molecular density is used. 200

Fig. 9-13 Calculated energy transmission of KrF laser pulses through He, Ne, N2, and Ar as a function of density using the calculated beam profile from Fig. 9-1 for a laser power of 0.02 TW. Also shown are the measured transmission data as in Fig. 7-25. 201
Fig. 9-14 Calculated electron temperature as a function of gas density in the same conditions as in Fig. 9-13. Note that for nitrogen the molecular density is used. 202

Chapter 1

Introduction

1.1 Introduction and Motivation

Research and development of shorter wavelength lasers into the extreme ultraviolet (XUV) and X-ray regions has been an area of great interest in recent years [1-5]. Due to their short wavelength, high brightness, and great ability to penetrate samples a few microns thick, such lasers will give potentially powerful tools for a number of applications in imaging of biological samples [6,7], diagnostics of fusion plasmas [8-10], and microlithography [11]. The study of XUV and X-ray lasers has motivated the need for a greater understanding of the physics of ionization and recombination in dense plasma. In addition, the propagation of the laser beam through the plasma is an important issue.

One of the promising techniques for pumping of XUV/X-ray lasers using small laboratory size laser systems is by means of above threshold ionization using high intensity subpicosecond pulses. Such ionization can result in a highly ionized cold plasma which subsequently recombines generating population inversions on a number of transitions. Analysis of such schemes was initially carried out by Gudzenko et al.[12], Peyraud et al. [13], and Ali and Jones [14-17] and more recently by Burnett, Enright and Corkum [4,5]. Central to the characterization of such laser schemes is the detailed understanding of the interaction of high intensity ultrashort laser pulses with plasmas.

The possibility of obtaining XUV and X-ray lasing in a cold recombining plasma was studied theoretically and numerically in the past [13-17,4]. It has been numerically shown that gains up to 70 cm^{-1} can be achieved if the plasma temperature is low, on the order of few eV [4]. To generate such a cold plasma, several methods of rapid cooling were attempted such as by plasma expansion [18,19] and radiation by high-Z plasmas [3]. Recently with the availability of picosecond and subpicosecond intense laser pulses, cold plasma production by multiphoton ionization has been proposed and studied numerically [4,5]. It has been shown that gains can be obtained from such a plasma with densities of order of 10^{19} - 10^{21} cm^{-3} produced by multiphoton ionization pumping. However, to achieve an elongated lasing medium in such a moderate to high density, the refraction of ultrashort pulse in the plasma is an important issue.

Another important application of plasmas generated by ultrashort laser pulses is the laser wake-field accelerator [21], in which a short ($\tau_L << 1$ ps), high-power ($P > 10^{12}$ W) laser pulse propagates in a plasma to generate a large-amplitude ($E > 1$ GV/m) wake field, which can trap and accelerate a trailing electron bunch. To have efficient wake field acceleration, a long interaction length is necessary which requires that the self refraction of the laser pulse be reduced [22].

The goal of achieving laser driven inertial confinement fusion (ICF) has been a major driving force for laser plasma research for over two decades [8-10]. Indirect drive schemes using high intensity lasers focused into gas filled hohlraum targets have recently been declassified. The propagation of high intensity laser pulses (at $I \geq 10^{15} W / cm^2$) over millimeter lengths of underdense plasma is a major issue in such schemes. Another new concept [23,24] called the fast ignitor requires the formation of a plasma guiding channel in the underdense coronal plasma and overdense ablation plasma and the subsequent propagation of an ultrahigh intensity 1-10 ps pulse through this guiding channel. This pulse will interact with the high density compressed core to produce a beam of energetic electrons which will ignite the fusion reaction in the core.

The study of the interaction of ultrashort high intensity laser pulses with matter is itself an active research area [25] . As a high intensity laser pulse is focused, the electrical field at the focus can be comparable to the Coulomb field that an electron experiences within an atom. As such, there are many interesting new nonlinear phenomena which can occur such as multiphoton absorption and ionization, above threshold ionization, self-phase modulation, relativistic self-focusing and channel formation [26,27], wake-field acceleration [21-22], and parametric instabilities [29] . Multiphoton ionization is a process in which an atom can be ionized by absorbing more than one photon simultaneously [30]. Above threshold or tunneling ionization is the process of multiphoton ionization at higher intensities where more photons than the minimum number of photons determined by the ionization energy of the ionized species are absorbed or equivalently the electric field of the laser is strong enough to lower the potential barrier binding the electron allowing it to tunnel out. The extra photons absorbed make the electrons released have significant residual energies [5,31] . Once being released from the atom, electrons oscillate in the laser field with quiver or pondermotive energy of $e^2E^2/4m_e\omega^2$, which is a function of the amplitude of the laser field and its frequency. Experimentally, it has been shown [32]that pulses with duration less than 1 ps can interact with electrons adiabatically, leaving the electrons cold because the electrons return their pondermotive energies to the pulse as it terminates. In the long pulse case the pondermotive energy will be converted to the translational energy of the electron as they escape the high intensity region. It is the former regime which is of interest for the potential creation of population inversion in an X-ray laser through fast recombination in a cold plasma. Most recently, Offenberger et al. [33] have carried out experiments to measure the heating of the electrons. Cold plasma (< 50 eV) has been achieved for a laser pulse of 12 ps at 268 nm at densities of the order of 10^{19} cm^{-3} and intensities of order of 10^{17} W/cm^2 [33].

As a high intensity laser pulse is focused into gaseous medium, the spatial nonuniformity of the focused beam produces a nonuniform radial electron density profile in the plasma which has its highest density and thus lowest refractive index on the axis. The plasma behaves like a diverging lens refracting the beam off the axis. Thus refraction is an important issue in studying the propagation of ultrashort high intensity laser pulses in plasma. At the same time, the laser pulse itself will experience a rapid change of refractive index in the ionization front as the ionizing plasma causes a negative time rate of change of the refractive index. This rapid change of refractive index modulates the phase velocity of the laser pulse, known as self-phase modulation which in this case induces a blue shift of the laser spectrum [35] .

1.2 Objective of Present Thesis

The objective of the present study is to investigate the formation of high density plasma columns by means of above threshold ionization of a gaseous medium and the propagation of ultrashort KrF laser pulses through such plasmas. As such, the investigation involves four experimental projects as outlined below.

1) *Multiphoton ionization formed plasma channels in static gas fill targets*:

The formation of plasma columns via multiphoton ionization in argon, helium and air was studied experimentally using 5 mJ, 6 ps KrF laser pulses focused by an f/10 12.5 cm focal length lens. The absorption and scattering of incident radiation and size and shift in the breakdown region was measured as a function of incident energy. Also time resolved shadowgraphy was employed to study the evolution of the resultant channels. The results were in agreement with multiphoton ionization initiated breakdown with subsequent collisional ionization and evolution of a 400-900 μm long cylindrical blast wave channels. Refraction of the laser pulses in the static fill gas cell was identified as a limitation to achieving high intensity at the focus and obtaining long plasma channels.

2). *Measurement of the KrF laser pulse width using a single shot visible autocorrelator*

A single shot autocorrelator based on the visible emission of two photon fluorescence spectra of the KrF laser radiation in BaF_2 was developed and characterized. A comparison was made with a simple two photon absorption measurement technique in quartz which was used for routine pulsewidth monitoring. With optimum adjustment of the KrF laser, subpicosecond laser pulse widths were measured. A novel method using the fluorescence emission intensity was also developed to measure the two photon absorption coefficient of BaF_2.

3). *Characterization of a high density gas jet target*

In order to reduce the refraction of the laser pulse prior to reaching its high intensity focus, a high density gas jet was developed. Its spatial density profile was characterized using laser interferometry and Abel inversion of the fringe profiles. Gas densities of up to 6×10^{20} cm $^{-3}$ at a distance of 200 μm above the nozzle tip were measured.

4). *Propagation of ultrashort KrF laser pulses through a high density gas jet*

The interaction of a picosecond high intensity (10^{17} W/cm $^{-2}$ in vacuum) KrF laser pulse with the high density gas jet was studied experimentally using several diagnostics. First, the refraction of the laser pulse was measured using CCD camera imaging. The asymptotic refraction angles of the laser beam through helium and nitrogen gas jets were determined as a function of gas pressure. Secondly the transmitted KrF laser radiation in helium, neon, argon and nitrogen gas jets was characterized in terms of the energy transmission within an F/2.5 cone angle and the ionization induced blue shifted spectrum was measured systematically for the first time for such high intensities and gas densities. The plasma formed in the helium jet was studied in more detail by imaging the emission in the direction perpendicular to the direction of the incident laser beam. One diagnostic involved imaging onto a CCD camera using a narrow band filter with a center wavelength of 468.5 nm (the 4-3 transition of He II) and thus images of the highly ionized helium plasma regions could be recorded. Along the same direction, the scattered UV laser radiation was imaged onto a streak camera which gave an indication of the propagation of the laser pulse through the gas jet. A third diagnostic involved the spectroscopic measurement of emission from the helium plasma. The lineshapes of He II emission at 468.5 nm were measured at the entrance, middle and exit of the gas jet target.

The remainder of this thesis is organized as follows. In Chapter 2, relevant background theory for the interaction of an ultrashort high intensity laser pulse with underdense plasma will be presented. This includes multiphoton ionization, above threshold ionization, inverse Bremsstrahlung, the pondermotive force and heating, and recombination dynamics.

Chapter 3 deals with the general experimental methods and instrumentation. A subpicosecond KrF laser system and various plasma diagnostics will be described. The visible two photon pulse width measurement technique for KrF laser pulse using BaF_2 is presented in Chapter 4.

In Chapter 5, the investigation of multiphoton ionization formed plasma columns in static gas targets is presented including: a) characterization of multiphoton ionization thresholds; b) refraction, absorption, and scattering of the laser pulse; and c) the evolution of the plasma column. Characterization of the high density gas jet is presented in Chapter 6. In Chapter 7, the experimental results of the emission studies from helium plasma are presented. These include visible emission spectra at 468.5 nm, imaging of the plasma channels, the 90 degree laser side scattering, and refraction of the laser beam. The energy transmission of the laser pulse through the gas jet is also measured. In Chapter 8, the ionization induced blue-shifted spectra will be presented for helium, neon, nitrogen, and argon for various pressures. In Chapter 9, simple 1D modeling code calculations are compared to the results and the conclusion of the present research is presented in Chapter 10.

References

1. M. D. Rosen, P. L. Hagelstein, D. L. Matthews, E. M. Campbell, A. U. Hazi, B. L. Whitten B. J. MacGowan, R. E. Turner, and R. W. Lee, Phys. Rev. Lett. 54, 106 (1985).
2. D. L. Matthews, P. L. Hagelstein, M. D. Rosen, M. J. Eckart, N. M. Ceglio, A. U. Hazi, H. Medecki, B. J. MacGowan, J. E. Trebes, B. L. Whitten, E. M. Campbell, C. W. Hatcher, A. M. Hawryluk, R. L. Kauffman, L. D. Pleasance, G. Rambach, J. H, Scofield, G. Stone, and T. A. Weaver, Phys. Rev. Lett. 54, 110 (1985).
3. S. Suckewer, C. H. Skinner, H. Milchberg, C. Keane, and D. Voorhees Phys. Rev. Lett. 55, 1753 (1985).
4. N. H. Burnett and G. D. Enright, IEEE J. Quan. Electron. 26, 1797 (1990).
5. N. H. Burnett and P. B. Corkum, J. Opt. Soc. Am. B 6, 1195 (1989).
6. T. Tomie, H. Shimizu, T. Majima, M. Yamada, T. Kanayama, H. Kondo, M. Yano, and M. Ono, Science 252, 691 (1991).
7. A. G. Michette, J. X-ray Sci. Tech 2, 1 (1990).
8. W. L. Kruer, The Physics of Laser Plasma Interactions, Addison-Wesley Publishing Company, Inc., 1988.

9. C. Yamanaka, in Physics of Laser Plasma, ed. a. Rubenchik and S. Witkowski, North Holland, New York (1991).
10. H. Hora, Physics of Laser Driven Plasmas, John Wiley & Son, 1981.
11. H. I. Smith and M L. Schattenburg, IBM Journal of Research and Development, 37, 319 (1993).
12. L. I. Gudzenko and L. A. Shelepin, Sov. Phys. JETP 18, 998 (1964); B. F. Gordiets, L. I. Gudzenko, and L. A. Shelepin, Sov. Phys. JETP 28, 489 (1969).
13. J. Peyraud and N. Peyraud, J. Appl. Phys., 43, 2993 (1972).
14. W. W. Jones and A. W. Ali, Appl. Phys. Lett. 26, 450 (1975).
15. W. W. Jones and A. W. Ali, J. Appl. Phys. 48, 3118 (1977).
16. W. W. Jones and A. W. Ali, J. Phys. B: Atom. Molec. Physics. 11, L87 (1978).
17. A. W. Ali and W. W. Jones, Phys. Lett. 55A, 462 (1976).
18. T. Hara, K. Kodera, M. Hamagaki, K. Matsunaga, M. Inutake, and T. Dote, Jan. J. Appl. Phys. 19, L606 (1980).
19. T. Hara, K. Kodera, M. Hamagaki, K. Matsunaga, M. Inutake, and T. Dote, Jan. J. Appl. Phys. 19, L386 (1980).
20. T. Usui, , Jan. J. Appl. Phys. 23, 468 (1984).
21. C. E. Clayton, K. A. Marsh, A. Syson, M.Evertt, A. Lal, W. P. Leemans, R. Williams, and C. Joshi, Phys. Rev. Lett. 70, 37 (1993).
22. J. Krall, A. Ting, E. Esarey, and P. Sprangle, Phys. Rev. E 48, 2157 (1993).
23. S. C. Wilks, W. L. Kruer, M. Tabak, and A. B. Langdon, Phys. Rev. Lett. 69, 1383 (1992).
24. M. Tabak, J. Hammer, M. E. Glinsky, W. L. Kruer, S. C. Wilks, Phys. Fluids 1,1626 (1994).
25. C. J. Joshi and P. Corkum, Phys. Today January, 36 (1995).
26. Guo-Zheng Sun, E. Ott, Y. C. Lee, and P. Guzdar, Phys. Fluids. 30, 526 (1987).
27. A. B. Borisov, A. V. Borovskiy, O. B. Shiryaev V. V. Korobkin, A. M. Prokhorov, J. C. Solem, T. S. Luk, K. Boyer, and C. K. Rhodes, Phys. Rev. A 45, 5830 (1992).
28. R. Rankin, C. E. Capjack, N. H. Burnett, and P. B. Corkum, Opt. Lett. 16, 835 (1991).
29. W. Rozmus, R. P. Sharma, J. C. Samson, W. Tighe, Phys. Fluids 30, 2181 (1987).
30. G. Mainfray and C. Manus, Rep. Prog. Phys. 54, 1333 (1991).
31. B. M. Penetrante and J. N. Bardsley, Phys. Rev. A 43, 3100 (1991).
32. R. R. Freeman and P. H. Bucksbaum, J. Phys. B 24, 325 (1991).
33. A. A. Offenberger, W. Blyth, A. E. Dangor, A. Djaoui, M. H. Key, Z. Najmudin, and J. S. Wark, Phys. Rev. Lett. 71, 3983 (1993).
34. W. J. Blyth, S. G. Preston, A. A. Offenberger, M. H. Key, J. S. Wark, Z. Najmudin, Phys. Rev. Lett. 74, 554 (1995).
35. W. M. Wood, C. W. Siders, and M. C. Downer, IEEE Trans. Plasma Sci. 21, 20 (1993).

Chapter 2

Theory

In this chapter, theoretical background relevant to multiphoton ionization pumped X-ray lasers and the interaction of ultrashort intense lasers with plasma is presented. The main aspects involve the rate equations for plasma ionization and recombination. In terms of ionization rates, Keldysh and tunneling formulas will be discussed. The heating of plasma will also be taken into account by ATI heating and IB heating. Refraction and defocusing of the laser beam is described. Finally the ionization induced blueshift will be elucidated. Throughout this thesis, the cgs units will be used.

2.1 XUV and X-ray lasers

The historical beginning of X-ray laser research dates back to 1964 when Gudzenko and Shelepin [1] suggested that a cold dense plasma could lead to population inversions due to rapid recombination into high lying bound levels. There is, however, no discussion about how to generate such a super cool highly ionized plasma. In 1972, Peyraud and Peyraud [2] did a theoretical study of such a lasing scheme in terms of a rate equation analysis. They also proposed that an intense laser beam be used to produce such a cold plasma via multiphoton ionization. The fundamental idea behind this scheme is that the multiphoton ionization does not heat the electrons. They realized that if a plasma could be formed in a time period which is shorter than the collisional time (e-i or e-atom), the electrons will not be heated by collisional heating, a process known as inverse Bremsstrahlung (IB).

In the following years, this concept has been further analyzed by Jones, Ali, and others [3-6] using time dependent rate equations. The calculations have taken into account the atomic physics, such as radiative recombination, three-body recombination, and electron collisional excitation, deexcitation, and ionization of each level. Here a simple three level model is presented [2] . The graphic representation of the energy levels is shown in Fig. 2-1, where the i , 1, and 0 are the ionization, excited, and ground levels respectively. The populations of the three levels are n_i, n_1, n_0 and the electron density is n_e. The laser transition energy of interest is $E_{01} = h\nu_{01}$ where ν_{01} is the emission frequency.

The appropriate rate equations can be written down with the following assumptions and transition rates:

a). Three-body recombination : $n_e^2 n_i R_{i1}$, $n_e^2 n_i R_{i0}$

where n_e is the electron density.

b). Spontaneous transitions: $n_1 A_{10}$

c). Stimulated emission and absorption rates: $n_1 B_{10} U_{\nu 01}$, $n_0 B_{01} U_{\nu 01}$

where B_{10} and B_{01} are the Einstein coefficients and $U_{\nu 01}$ is the radiation energy density at ν_{01} .

d). Collisional deexciation: $n_1 R_{cd\ 1\rightarrow 0}$

e). Excitation processes ignored under the assumption of a cold plasma.

These lead to the rate equations

$$
\begin{aligned}
\frac{\partial n_1}{\partial t} &= n_e^2 n_i R_{i1} - n_1 (R_{cd\,1\to 0} + A_{10} + B_{10} U_{v01}) \\
\frac{\partial n_0}{\partial t} &= n_1 (R_{cd\,1\to 0} + A_{10} + B_{10} U_{v01}) + n_e^2 n_i R_{i0} \qquad (2.1) \\
\frac{\partial n_i}{\partial t} &= -\, n_e^2 n_i (R_{i1} + R_{i0})
\end{aligned}
$$

To solve the set of equations, the rates for various processes need to be known. Fortunately, these rates have been studied over many years for astrophysical purpose. A detailed discussion of the rates may be found in Ref. 11. The following gives the relevant rates for Eqn. 2.1.

The rate of three-body recombination is

$$R_{3B} = 4.93 \times 10^{-28} \frac{g_j\, \xi \exp(\chi_i / T_e) E_1(\chi_i / T_e)}{g_{j+1}\, \chi_i\, T_e^2} \qquad \frac{\text{cm}^6}{\text{s}} \qquad (2.2)$$

where χ_i is the ionization potential from the bound state in eV while T_e is the electron temperature in eV. The g_j and g_{j+1} are the statistical weights of the final level and ground state of the ionized level. The ξ is the number of electrons in the outer shell of the ionizing species and the E_1 is the exponential integral of the first kind defined by

$$E_1(y) = \int_y^{\infty} \frac{\exp(-s)}{s}\, ds \qquad (2.3)$$

Note that $\exp(y)E_1(y) \to 1/y$ as $y \to \infty$.

The rate of the radiative recombination is [11]:

$$R_{rad} = \bar{g}_i 5.2 \times 10^{-14}\, Z \left(\frac{\chi_i}{T_e}\right)^{3/2} \exp\left(\frac{\chi_i}{T_e}\right) E_1\left(\frac{\chi_i}{T_e}\right) \qquad \frac{cm^3}{s} \qquad (2.4)$$

here $\bar{g}_i$ is the Gaunt factor which is close to unity. χ_i is the Rydberg energy for the bound level of i in hydrogenic ion of charge Z, and T_e is the temperature in eV. For plasmas of interest above and investigated in the present thesis the radiative recombination rates are much less than three-body recombination and thus can be ignored. The spontaneous emission rate from a upper state i to a lower state j is

$$A_{ij} = \frac{6.67 \times 10^{15}}{\lambda_{ij}^2} \frac{g_j}{g_i} f_{ji} \qquad sec^{-1} \qquad (2.5)$$

Here the g_i and g_j are the statistical weights of the states and λ_{ij} is the wavelength of the transition in angstroms. The (absorption) oscillator strength f_{ji} can be obtained from published data [12].

The absorption and stimulated emission coefficients B_{ji} and B_{ij} are related to the spontaneous decay rate A_{ij} as follows [11,13,14]

$$A_{ij} = \frac{8\pi h \nu_{ij}^3}{c^3} B_{ij}$$
$$g_i B_{ij} = g_j B_{ji} \qquad (2.6)$$

The collisional deexcitation rate is [11]

$$R_{cd} = 2.5 \times 10^{-5} \frac{(g_j/g_i) f_{ji}}{E_{ij} T_e^{1/2}} \qquad \frac{cm^3}{s} \qquad (2.7)$$

Here the g_j and g_i are the statistical weights of the energy levels, E_{ij} is the difference in energies of the two levels in eV and T_e is the electron temperature in eV.

Based on these rate equations it has been shown that significant population inversions are possible on the 3-2 and even 2-1 transitions of ions [3-6]. More recent calculations taking into account the ionization process and residual plasma temperature have also shown that population inversions are possible on the 3-2 and 2-1 transitions for ions up to Boron [15].

2.2 Multiphoton ionization

Multiphoton ionization is a process in which an atom with an ionization potential χ will be ionized by the absorption of N photons with energy $\hbar\omega$, where N is the first integer for which $N\hbar\omega$ exceeds the ionization potential. Multiphoton ionization has been studied extensively both theoretically and experimentally not long after the invention of lasers in early 1960s [16,17]. The initial experiments could be described by lower order perturbation theory. However, as the laser intensity increases, the perturbation becomes comparable to the primary interaction, which occurs when the electrical field of the laser approaches that of Coulomb field of the atom itself. At this stage, perturbation theory breaks down and the process can be described better as a tunneling process through the reduced potential barrier.

In 1965, Keldysh [17] developed a theory accounting for the generalized treatment of ionization of atoms and solid matter in a strong laser field. A schematic diagram of the multiphoton ionization process is shown in Fig. 2-2 and the lowering of the potential barrier and the electron tunneling process is shown in Fig. 2-3. In Fig. 2-2 the process of absorption of n photons simultaneously to achieve ionization is shown. In Fig. 2-3 the time averaged lowering of the Coulomb barrier confining the electron is shown. Once the barrier is lowered sufficiently the probability of the electron tunnelling through the remaining barrier becomes very large.

The Keldysh theory showed that multiphoton ionization was one limiting case of a general solution for the ionization probability. The regimes of multiphoton ionization are determined by the Keldysh parameter given by $\gamma = \omega(2m_e\chi_0)^{1/2} / eE$, where χ_0 is the field-free ionization potential of the atom, E the electric field strength, and e and m_e are the charge and mass of an electron. The Keldysh parameter is the ratio of the frequency of the applied electromagnetic field, ω, to the tunneling frequency ω_t, where $\omega_t = eE / (2m_e\chi_0)^{1/2}$. The regime of multiphoton ionization is given by $\gamma >> 1$. In this case the time required to tunnel through the potential barrier is long compared to the period of oscillation for the electric field. The other limiting case resembles autoionization due to tunneling in a low frequency alternating field and occurs for $\gamma << 1$. Thus tunneling can be expected to occur in the strong-field, low-frequency limit, while multiphoton ionization occurs in the weak-field, high-frequency regime. Keldysh stressed that the two processes were not competing mechanisms but merely two limiting cases of the same ionization process. The transition from one to the other occurs when the tunneling time through the potential barrier was of the order of the oscillation period of the applied field.

The Keldysh ionization rate for atoms is given by [17,18]

$$W = A\,\omega \left(\frac{\chi_0}{\hbar\omega}\right)^{3/2} \left(\frac{\gamma}{\sqrt{1+\gamma^2}}\right)^{5/2} S\!\left(\gamma, \frac{\chi_\omega}{\hbar\omega}\right) \times \exp\left(-\frac{2\chi_\omega}{\hbar\omega}\left(\sinh^{-1}\gamma - \gamma\,\frac{\left(1+\gamma^2\right)^{1/2}}{1+2\gamma^2}\right)\right) \qquad (2.8)$$

Where

$$\chi_\omega = \chi_0 + \frac{e^2E^2}{4m_e\omega^2},$$

$$S\!\left(\gamma, \frac{\chi_\omega}{\hbar\omega}\right) = \sum_{m=0}^{\infty} \exp\left(-2\left(\left\langle\frac{\chi_\omega}{\hbar\omega}+1\right\rangle - \frac{\chi_\omega}{\hbar\omega} + m\right)\left(\sinh^{-1}\gamma - \frac{\gamma}{\left(1+\gamma^2\right)^{1/2}}\right)\right) \times \Phi\left(\left(\frac{2\gamma}{\left(1+\gamma^2\right)^{1/2}}\left(\left\langle\frac{\chi_\omega}{\hbar\omega}+1\right\rangle - \frac{\chi_\omega}{\hbar\omega} + m\right)\right)^{1/2}\right),$$

$$\Phi(x) = \int_0^x e^{t^2-x^2}\,dt \quad ,$$

Where $\left\langle\left(\chi_\omega / \hbar\omega\right)+1\right\rangle$ is the minimum number of photons required to ionize and A is a numerical factor of order unity to account for a weak dependence upon the details of the atom.

In the tunneling limit, Ammosov [19] has derived a formula which is considered to be more suitable to the tunneling problem.

$$W = 4.134 \times 10^{16} \left(\frac{3e}{\pi} \right)^{1/2} \frac{Z^2}{\left(n^*\right)^{4.5}} \left(\frac{4\, e\, Z^3}{\varepsilon \left(n^*\right)^4} \right)^{2n^* - 1.5} \exp\left(- \frac{2\, Z^3}{3 \left(n^*\right)^3 \varepsilon} \right) \quad S^{-1} \qquad (2.9)$$

where Z is the charge of the ionized atom and

$$n^* = Z \left(\frac{13.605}{\chi} \right)^{1/2} \qquad \text{with } \chi \text{ given in eV}$$

$$\varepsilon = \left(\frac{I}{3.51 \times 10^{16}} \right)^{1/2} \qquad \text{with I given in } W / cm^2$$

Many experiments investigating the pure multiphoton ionization process deal with a low density of atoms so that collisional effects can be excluded. By measuring the ejected electron energy spectra, a multi-peak electron energy distribution has been revealed. The higher energy peaks are spaced evenly apart by one photon energy. This suggests that the electron can absorb more photons than the minimum number of photons to reach ionization. This has come to be known as the Above-threshold-ionization (ATI). The extra energy acquired by the electron will be of importance to the heating of the plasma produced and will be discussed below.

2.3 Heating of electrons

As mentioned above, the minimization of heating of the electrons is important in order to obtain a cold recombining plasma for XUV and X-ray lasing. There are several heating mechanisms such as ATI, ponderomotive, SRS and IB heating. In the following, three of these will be discussed. SRS heating will not be discussed since the threshold for onset of SRS is above the intensities studied in the present investigation.

2.3.1 ATI heating

As the laser intensities are increased above $I\lambda^2 \sim 10^{16}\ \mathrm{W\,\mu m^2/cm^2}$, the electrons resulting from ATI have surplus energies in excess of the energy due to the coherent oscillation of the free electron in the electromagnetic wave. The coherent energy of oscillation of the electron, also called the ponderomotive energy, is adiabatically returned to the propagating wave packet as it departs and leaves no excess energy in the electron iteself. The amount of surplus energy can be calculated from semiclassical considerations. Burnett and Corkum [21] have shown that the excess electron energy can be attributed to the mismatch between the phase at the instant of ionization and the crest of the electromagnetic wave. With a plane-polarized electromagnetic wave given as $E_L=E\sin(\omega t)$, an electron released from rest at the crest of the wave moves with only the ponderomotive energy at all subsequent times. However, an electron created at some arbitrary phase mismatch will oscillate out of phase with the laser field, resulting in a residual kinetic energy $\varepsilon = 2E_q \sin^2 \Delta\phi$, where $E_q = e^2E^2/4m\omega^2$ is equal to the quiver or ponderomotive energy. This residual energy can be considered as the work done by the field on the electron. The average ATI energy can be calculated by weighting the excess energy by the probability of an electron being created at a given phase angle of the field. In the limit of high fields the ionization event occurs over a short period of an oscillation and the ionization probability can be evaluated using the static DC field ionization rate [22]

$$W_{st}(E_s,\chi_i) = 4\omega_a\left(\frac{\chi_i}{\chi_h}\right)^{5/2}\frac{E_a}{E_s}\exp\left[-\frac{2}{3}\left(\frac{\chi_i}{\chi_h}\right)^{3/2}\frac{E_a}{E_s}\right] \tag{2.10}$$

Where ω_a is the atomic frequency unit of $4.1\text{x}10^{16}$ sec^{-1}, χ_i is the ionization potential, χ_h is the ionization potential of hydrogen, E_a is the atomic field strength at the Bohr radius of hydrogen (E_a=5.1 x 10^9 V/cm), and E_s is the static field strength. In this case the average ATI energy becomes

$$\langle\varepsilon\rangle = \frac{\int_0^{\pi/2} 2E_q W_{st}(E_L,\chi_i)\cos^2\phi \, d\phi}{\int_0^{\pi/2} W_{st}(E_L,\chi_i)\, d\phi} \tag{2.11}$$

Some calculated values of ATI heating as a fraction of the ponderomotive energy based on these equations are given in table 2.1. It can be seen that $\langle\varepsilon\rangle$ is on the order of 10-18% of the quiver energy for the above range of parameters. Thus it can be kept well below the ionization potential for ionization energies up to 100 eV for UV lasers [21].

Table. 2.1 ATI heating for ionization rates of 10^{12}, 10^{13}, and 10^{14} s^{-1} and ionization energies of 10 to 200 eV calculated for a laser wavelength of 0.25 μ m

	10^{12} s^{-1}			10^{13} s^{-1}			10^{14} s^{-1}		
χ_i (eV)	I (W/cm^2)	$\frac{\langle\varepsilon\rangle}{E_{quiver}}$	E_{quiver} (eV)	I (W/cm^2)	$\frac{\langle\varepsilon\rangle}{E_{quiver}}$	E_{quiver} (eV)	I (W/cm^2)	$\frac{\langle\varepsilon\rangle}{E_{quiver}}$	E_{quiver} (eV)
10	3.57E13	0.125	0.209	5.35E13	0.148	0.312	8.9E13	0.181	0.521
20	2.57E14	0.120	1.5	3.76E14	0.14	2.19	6.02E14	0.169	3.51
50	3.52E15	0.113	20.5	5.0E15	0.131	29.2	7.69E15	0.156	44.9
100	2.56E16	0.109	149.5	3.58E16	0.125	208.6	5.35E16	0.148	312.2
200	1.87E17	0.105	1094	2.57E17	0.12	1500	3.75E17	0.140	2191

2.3.2 Ponderomotive force and heating

Due to the motivation of inertial confinement fusion studies, the interaction of intense laser pulses with plasma has been studied extensively [23,24]. One important factor in the interaction process is the ponderomotive force which can accelerate electrons out of high field regions. The ponderomotive force arises from the potential gradient of the laser field in the focal region. An electron ejected from the parent atoms or ions starts immediately oscillating in the laser field with an average oscillatory energy given by

$$E_{osc} = \left\langle \frac{e^2 E_L^2(t)}{2m\omega^2} \right\rangle = \frac{e^2 E_L^2}{4m\omega^2} \qquad (2.12)$$

where the brackets $\langle\ \rangle$ denote a time average over one optical cycle, $E_L(t) = E_L \sin\omega t$, where E_L is the peak electric field amplitude of the laser, and ω is the laser frequency. The oscillatory energy E_{osc} is also called the ponderomotive potential E_{pm} and the gradient in this potential leads to the ponderomotive force [25] given in terms of the gradient in the electric field by

$$f_p = -\nabla\left\langle \frac{e^2 E_L{}^2}{4m\omega^2} \right\rangle = -\frac{e^2}{4m\omega^2}\nabla\langle E_L{}^2\rangle \qquad (2.13)$$

It can be seen from equation (2.13) that the force depends on the gradient of the square of the field and not on the field polarization. In terms of intensity, I, and laser wavelength, λ, the pondermotive force is proportional to the product in $I\lambda^2$.

The electrons released from the parent atom or ion are free to move in response to the nonlinear force and can be accelerated out of the laser beam to high energies. For a cylindrically symmetric field intensity, the electron motion should be the same along all radii. For high laser intensities (i.e., I $\lambda^2 > 10^{14}$ Wμm^2/cm^2), given sufficient time, a number of electrons will be expelled from the interaction region. The final energy thus acquired by an electron which completely escapes the high field region can be simply described in the multiphoton ionization regime by

$$E = n\hbar\omega - \chi_0 + E_{pm} \qquad (2.14)$$

where n is the number of photons absorbed, and χ_0 is the field free ionization potential. The average energy carried by the expelled electron will contribute partially to the plasma temperature.

The expulsion of electrons also depends on the laser pulse length. The ponderomotive potential will be converted to the translational kinetic energy of the electrons when the pulse is longer than tens of picoseconds. While for picosecond or subpicosecond pulses, the electrons do not have enough time to escape the focal volume. In the latter case the electron returns its oscillatory energy adiabatically to the field as the laser pulse passes. In this way, cold electrons may be expected. This behavior may be appropriate for intensities up to $I\lambda^2 \sim 10^{18}$ Wμ^2/cm^2 [26,28]. For higher intensities $I\lambda^2 >$

10^{18} W μ^2/cm^2, the electron motion becomes relativistic and the expulsion of the electrons will be significantly modified [29,30] as will be discussed later.

2.3.3 Inverse Bremsstrahlung at high intensities

The heating in laser produced plasmas for longer pulse interactions arises mainly from collisional or so called inverse Bremsstrahlung heating. Inverse Bremsstrahlung is a process involving elastic electron-ion collisions which increase the residual energy by transferring energy from ordered quiver motion to random motion. The IB absorption coefficient is given by [32,33]

$$\alpha = \frac{7.8\times10^{-9}\, Z\, n_{ecm}^2 \ln\Lambda(\omega)}{\nu^2\, T_{eV}^{3/2}\left[1-\frac{\omega_p^2}{\omega^2}\right]^{1/2}} \quad \text{cm}^{-1} \qquad (2.15)$$

which is calculated from the electron ion collision frequency given by

$$\nu_{ei}^{u} = \frac{4\sqrt{2\pi}}{3}\,\frac{Z^2 n_i e^4 \ln\Lambda(\omega)}{m_e T_e^{3/2}} = 2.91\times10^{-6}\,\frac{Z\, n_{ecm} e^4 \ln\Lambda(\omega)}{T_{eV}^{3/2}} \quad \text{s}^{-1} \qquad (2.16)$$

which in turn is found to be averaging the monoenergetic electron collision frequency over a Maxwellian velocity distribution, where Z is the charge of the ions, n_{ecm} is the electron density in cm^{-3}, ν is the laser frequency in Hz, T_{eV} is the electron temperature in eV and $\ln\Lambda(\omega)$ is the frequency dependent Coulomb logarithm.

In the limit of high laser intensities and cold plasma temperatures, the oscillatory velocity of the electron can become comparable to or greater than its thermal velocity. In this regime two effects alter the collisional heating rates. Firstly, the effective velocity of the electrons is increased by the oscillatory motion in the applied field. This reduces the collision frequency significantly when the oscillatory velocity, $\upsilon_{osc} = eE_0/m_e\omega$ is greater than the thermal velocity $\upsilon_{th} = \sqrt{kT/m_e}$. Both quantum mechanical and plasma kinetic theory calculations of the correction to the collision frequency have been carried out for Maxwellian velocity distribution [33-35] yielding a correction factor in terms of integrals over modified Bessel functions. An adequate approximation to this more exact result can be obtained by using an effective temperature given by the total energy of the electron in the applied field, where

$$\begin{aligned}\frac{3}{2}k_BT_{eff} &= \frac{3}{2}k_BT_e + \frac{1}{2}m\left\langle \upsilon_{osc}^2(t)\right\rangle \\ &= \frac{3}{2}k_BT_e\left[1+\frac{1}{6}\frac{\upsilon_{osc}^2}{\upsilon_{th}^2}\right] \qquad (2.17)\end{aligned}$$

Substituting this effective temperature into the absorption coefficient gives an intensity dependent correction factor of

$$F = \frac{1}{\left[1+\frac{1}{6}\frac{\upsilon_{osc}^2}{\upsilon_{th}^2}\right]^{3/2}} \qquad (2.18)$$

where υ_{osc} and υ_{th} can be given in practical units by

$$\upsilon_{osc} = \frac{eE_0}{m_e\omega} = 2.6 \times 10^8 \ \lambda_{\mu m} \sqrt{I_{14}} \qquad \text{cm / s} \qquad (2.19)$$

$$\upsilon_{th} = \sqrt{\frac{kT}{m_e}} = 4.2 \times 10^7 \sqrt{T_{eV}} \qquad \text{cm / s} \qquad (2.20)$$

where I_{14} is the laser intensity in units of 10^{14} W/cm^2. This correction factor was suggested by Faehl [37] and agrees with the more exact integral expressions [33,34] to within approximately 10%.

The second factor is the generation of non-Maxwellian velocity distributions in these strongly driven plasmas. The above absorption coefficients were all calculated based on Maxwellian velocity distributions. Chichkov [38,39] has discussed the regimes where non-Maxwellian velocity distributions are expected. For very low intensities and very high intensities, given by $\upsilon_{osc}/\upsilon_{th} < 1/\sqrt{Z}$ or $\upsilon_{osc}/\upsilon_{th} > Z$, Maxwellian distribution are expected. For intensities in the range of $1/\sqrt{Z} < \upsilon_{osc}/\upsilon_{th} < 1$ non-Maxwellian distributions of the type $\exp(-\upsilon^5/\upsilon_m^5)$ are expected as first pointed out by Langdon [40]. For the intensities in the range of $1 < \upsilon_{osc}/\upsilon_{th} < Z$ different non-maxwellian electron energy distributions are expected in the directions parallel and perpendicular to the polarization of the driving electric field. However, the development of the non-Maxwellian Langdon type distributions takes some period of time on the order of picoseconds as determined by Fokker Planck simulations [41,42]. Once a "Langdon" distribution has been formed the absorption coefficient is reduced by the factor

$$F_{\text{Langdon}} = 1 - \frac{0.553}{\left(1 + \frac{0.27}{Z\left(\frac{\upsilon_{osc}}{\upsilon_{th}}\right)^2}\right)^{0.75}} \tag{2.21}$$

The fully corrected high field absorption coefficient for non-Maxwellian distributions has yet to be reported. Calculations of the non-Maxwellian electron energy distributions is beyond the scope of the present thesis. In the following discussions the approximate factors given by Eqn. 2.18 and 2.21 will be employed where necessary.

2.4 Refraction and self-focusing

When a laser beam is focused into a gas, to the lowest order approximation the focal intensity can be assumed to have a Gaussian profile. The nonuniform radial intensity distribution will give a non-uniform electron density profile with the highest electron density being on the axis. This electron density increase causes a decrease of refractive index on axis as seen by the relation between electron density and the refractive index given by

$$n_r = \sqrt{1 - \frac{\omega_p^2}{\omega^2}} = \sqrt{1 - \frac{n_e}{n_c}} \approx 1 - \frac{n_e}{2n_c} \tag{2.22}$$

for underdense plasma, where $\omega_p = \left(4\pi n_e e^2 / m_e\right)^{1/2}$ is the plasma frequency. This leads to refraction of the beam away from the axis since the plasma has the characteristic of a negative lens. Assuming that the laser is propagating in the z direction and is deflected in the y direction, then the integrated deflection angle, θ, for a single light ray can be calculated by the relation:

$$\theta = \int \frac{dn_r}{dy} dz \qquad (2.23)$$

This ionization induced refractive defocusing makes it very difficult to propagate high intensity picosecond laser pulses over long lengths through plasma, an effect which has been studied numerically [43] and is one of the areas of studies in the present thesis. To overcome this drawback, a preformed plasma channel with a high electron density off axis has been proposed [44-46] based on both earlier studies of CO_2 laser and recent picosecond laser induced channel formation, heating, and propagation.

As laser intensities become high ($I\lambda^2 > 10^{18}$ W μm/cm ^{2}) and the pulses becomes very short (< 1 ps), two important effects may become dominant in contributing to an increase of refractive index on axis [29,30]. Firstly, the motion of the electrons becomes relativistic since the oscillatory velocity of electrons in intense electromagnetic fields approaches the speed of light. The resultant increase of the electron mass decreases the local plasma frequency and thus causes an increase of refractive index which is larger on axis than in the outer region. This is reflected in the modified plasma frequency given as [47]

$$\omega_{prel} = \frac{\omega_p}{\sqrt{1+\frac{e^2 E_L^2}{m_e^2 c^2 \omega^2}}} \qquad (2.24)$$

Where E_L is the peak amplitude of the electric field. Secondly, the electrons will be rapidly expelled out of the axial region due to the very large poderomotive force [29]. This in turn makes the refractive index increase on axis relative to the surrounding plasma region. This latter effect of ponderomotive expulsion of electrons is also important for longer laser pulses propagating through large scale length plasmas and is known as ponderomotive self focusing. These two effects combine, depending on the input laser parameter and plasma conditions, giving a nonuniform refractive index across the beam which acts now as a waveguide which will confine and guide the laser pulse itself. The formation of such a self-guiding channel has been theoretically studied and has been pursued experimentally [48,49].

At high fields the final result of the above effects is electron cavitation that is complete expulsion of electrons from the core of the plasma column, and self-focusing of the laser beam to a micron or submicron diameter channel. This result occurs above a laser power which is known as the critical power for relativistic self-focusing. Theoretical calculation and numerical analysis [29] have shown that this power is of the order of

$$P = 1.6 \times 10^{10} (\omega / \omega_p)^2 \quad \text{W} \qquad (2.25)$$

2.5 Ionization induced blueshift

As a laser pulse is focused into gases, the laser pulse experiences a rapid decrease in the refractive index due to the fast growth of electron density in the ionization front.

This change of refractive index causes an additional phase shift in the electric field of the ionizing laser pulse, resulting in a higher phase velocity. As such, the transmitted spectra of the incident laser beam will broaden and shift to higher frequencies (a blueshift in wavelength). For a homogeneous and underdense plasma produced by a monochromatic plane wave, the ionization induced wavelength shift can be calculated from the time rate of change of the refractive index given by [50]

$$\delta\lambda = \frac{2\pi}{\omega_0} \int \frac{\partial n_r}{\partial t}(l)\, dl \qquad (2.26)$$

In terms of experimental parameters the shift is given by

$$\delta\lambda = \frac{e^2 N_0 L \lambda^3}{8\pi^2 \varepsilon_0 m_e c^3} \frac{dZ}{dt} = 4.48 \times 10^{-39}\ N_{0cm}\ L_{mm}\ \lambda_{nm}^3 \frac{dZ}{dt} \qquad \text{nm} \qquad (2.27)$$

here N_{0cm} is the atom density in cm^{-3}, L_{mm} is the interaction length in mm, λ_{nm} is the laser wavelength in nm, and Z the degree of ionization.

The shift depends on the laser intensity, its spatial distribution at the focus, pulse duration, gas density and the state of ionization. By measuring the shifted spectra one can probe the ionization dynamics in the creation of the plasma. In addition, as the focused beam has its highest intensity on the axis and falls off radially, different radial portions of the pulse front will experience different shifts since the ionization rate is sensitive to the intensity. This complicates the ionization problem. Eqn. 2.27 does not include the propagation effects which are important for a short pulse. To take account of these effects in detail, one needs to solve the equations for propagation of the laser pulse and ionization of the background medium together. A full solution using the Maxwell equations coupled with the ionization rates has been reported [51]. A simple solution taking into account the axial propagation of the laser pulse and ionization dynamics will be presented and utilized in the discussion of experimental measurements given in this thesis.

References

1. L. I. Gudzenko and L. A. Shelepin, Sov. Phys. JETP 18, 998 (1964); B. F. Gordiets, L. I. Gudzenko, and L. A. Shelepin, Sov. Phys. JETP 28, 489 (1969).
2. J. Peyraud and N. Peyraud, J. Appl. Phys., 43, 2993 (1972).
3. W. W. Jones and A. W. Ali, Appl. Phys. Lett. 26, 450 (1975).
4. W. W. Jones and A. W. Ali, J. Appl. Phys. 48, 3118 (1977).
5. W. W. Jones and A. W. Ali, J. Phys. B: Atom. Molec. Physics. 11, L87 (1978).
6. A. W. Ali and W. W. Jones, Phys. Lett. 55A, 462 (1976).
7. T. Hara, K. Kodera, M. Hamagaki, K. Matsunaga, M. Inutake, and T. Dote, Jan. J. Appl. Phys. 19, L606 (1980).
8. T. Hara, K. Kodera, M. Hamagaki, K. Matsunaga, M. Inutake, and T. Dote, Jan. J. Appl. Phys. 19, L386 (1980).
9. T. Usui, , Jan. J. Appl. Phys. 23, 468 (1984).
10. R. W. Lee, RATION Manual, Lawrence Livermore Laboratory (1990).
11. I. H. Hutchinson, Principles of plasma diagnostics, Cambridge University Press, (1990).
12. G. A. Martin and W. L. Wiese, J. Chem. Ref. Data 15, 537 (1983).
13. D. R. Bates., A. E. Kingston and R. W. Mcwhirter, Proc. Roy. Soc. A267, 297 (1962).
14. D. R. Bates., A. E. Kingston and R. W. Mcwhirter, Proc. Roy. Soc. A270, 155 (1962).
15. N. H. Burnett and G. D. Enright, IEEE J. Quan. Electron. 26, 1797 (1990).
16. G. Mainfray and C. Manus, Rep. Prog. Phys. 54, 1333 (1991).
17. L. V. Keldysh, Sov. Phys. JETP 20, 1307 (1965).
18. M. D. Perry, O. L. Landen, A. Szoke, and E. M. Campbell, Phys. Rev. A 37, 747 (1988).
19. M. V. Ammosov, N. B. Delone, and V. P. Krainov, Sov. Phys. JETP 64, 1191 (1986).
20. A. M. Perelomov, V. S. Popov, and M. V. Terentev, Sov. Phys. JETP 23, 924 (1966).
21. N. H. Burnett and P. B. Corkum, J. Opt. Soc. Am. B 6, 1195 (1989).
22. L. D. Landau and E. M. Lifshitz, Quantum Mechanics, 3rd ed. (Pergamon, London, 1978).
23. W. L. Kruer, The Physics of Laser Plasma Interactions, Addison-Wesley Publishing Company, Inc., 1988.
24. C. Yamanaka, in Physics of Laser Plasma, ed. a. Rubenchik and S. Witkowski, North Holland, New York (1991).
25. F. F. Chen, Introduction to plasma physics, Plenum Press (1974).

26. W. J. Blyth, S. G. Preston, A. A. Offenberger, M. H. Key, J. S. Wark, Z. Najmudin, Phys. Rev. Lett. 74, 554 (1995).
27. B. M. Penetrante and J. N. Bardsley, Phys. Rev. A 43, 3100 (1991).
28. A. A. Offenberger, W. Blyth, A. E. Dangor, A. Djaoui, M. H. Key, Z. Najmudin, and J. S. Wark, Phys. Rev. Lett. 71, 3983 (1993).
29. Guo-Zheng Sun, E. Ott, Y. C. Lee, and P. Guzdar, Phys. Fluids. 30, 526 (1987).
30. A. B. Borisov, A. V. Borovskiy, O. B. Shiryaev V. V. Korobkin, A. M. Prokhorov, J. C. Solem, T. S. Luk, K. Boyer, and C. K. Rhodes, Phys. Rev. A 45, 5830 (1992).
31. D. Umstadter, E. Esarey, and K. Kim, Phys. Rev. Lett. 72, 1224 (1994).
32. T. W. Johnson and J. M. Dawson, Phys. Fluids 16, 722 (1973).
33. V. P. Silin, Sov. JETP 20, 1510 (1966).
34. H. Brysk, J. Phys. A: Math. Gen., 8, 1260 (1975).
35. C. D. Decker, W. B. Mori, and J. M. Dawson, Phys. Plasmas 1, 4043 (1994).
36. F. V. Bunkin and M. V. Fedorov, Sov. JETP, 22, 844 (1966).
37. R. J. Faehl and N. F. Roderick, Phys. Fluids 21, 793 (1978).
38. B. N. Chichkov J. Phys. B: At. Mol. Opt. Phys. 23, L333 (1990).
39. B. N. Chichkov, S. A. Shumsky, ans S. A. Uryupin, Phys. Rev. A 45, 7475 (1992).
40. A. B. Langdon, Phys. Rev. Lett. 44, 575 (1990).
41. J. P. Mate, M. Lamoureux, C. Moller, R. Y. Yin, J. Delettrez, J. Virmont and T. W. Johnston, Plasma Phys. and Controlled Fusion 30, 1665 (1988).
42. P. E. Pulsifer and K. G. Whitney, Phys. Rev. E 50, 4926 (1994).
43. R. Rankin, C. E. Capjack, N. H. Burnett, and P. B. Corkum, Opt. Lett. 16, 835 (1991).
44. N. H. Burnett, Private Communication.
45. Y. M. Li, J. N. Broughton, R. Fedosejevs, and T. Tomie, Opt. Comm. 93, 366 (1992).
46. C. G. Durfee III and J. M. Milchberg, Phys. Rev. Lett. 71, 2409 (1993).
47. J. C. Solem, T. S. Luk, K. Boyer, and C. K, Rhodes, IEEE J.Quant. Electron. 25, 2423 (1989).
48. A. B. Borisov, A. V. Borovskiy, V. V. Korobkin, A. M. Prokhorov, O. B. Shiryaev, X. M. Shi, T. S. Luk, A. M. McPherson, J. C. Solem, K. Boyer, and C. K. Rhodes, Phys. Rev. Lett. 68, 2309 (1992).
49. A. Sullivan, H. Hamster, S. P. Gordon, and R. W. Falcone, Optics Lett. 19, 1544 (1994).
50. W. M. Wood, C. W. Siders, and M. C. Downer, IEEE Trans. Plasma Sci. 21, 20 (1993).
51. S. C. Rae and K. Burnett, Phys. Rev. A 46, 1084 (1992).
52. P. Monot, T. Auguste, P. Gibbon, F. Jakober, and G. Mainfray, A. Dulieu, M. Louis-Jacquet, G. Malka, and J. L. Miquel, Phys. Rev. Lett. 74, 2953 (1995).
53. P. Monot, T. Auguste, L. A. Lompre, G. Mainfray, and C. Manus, J. Opt. Soc. Am. B 9, 1579 (1992).

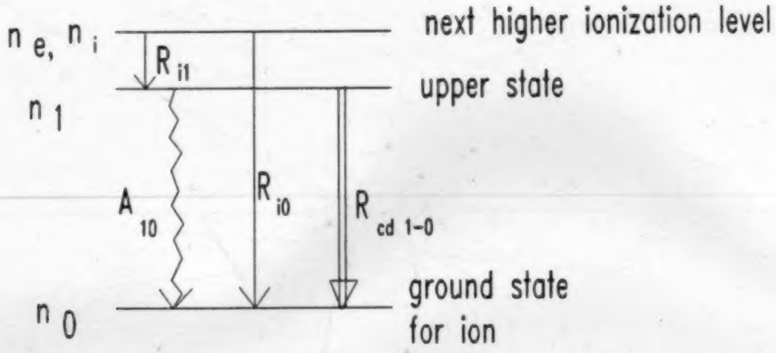
n e, n i
R i1
n 1
A 10
R i0
R cd 1-0
n 0
next higher ionization level
upper state
ground state
for ion

Fig. 2-1. Energy levels for simple three level model.

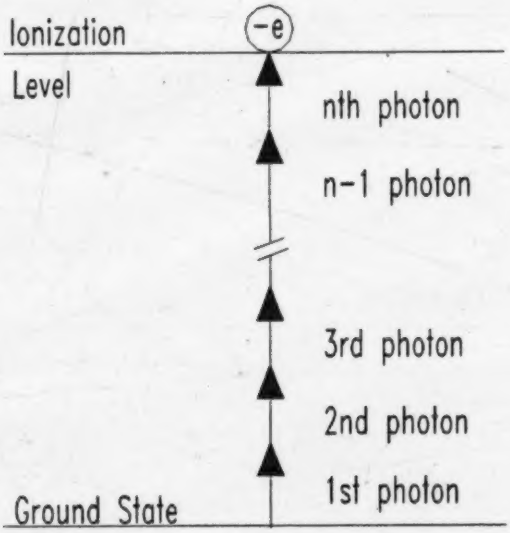
Ionization
Level
-e
nth photon
n-1 photon
3rd photon
2nd photon
1st photon
Ground State

Fig. 2-2 Multiphoton Ionization

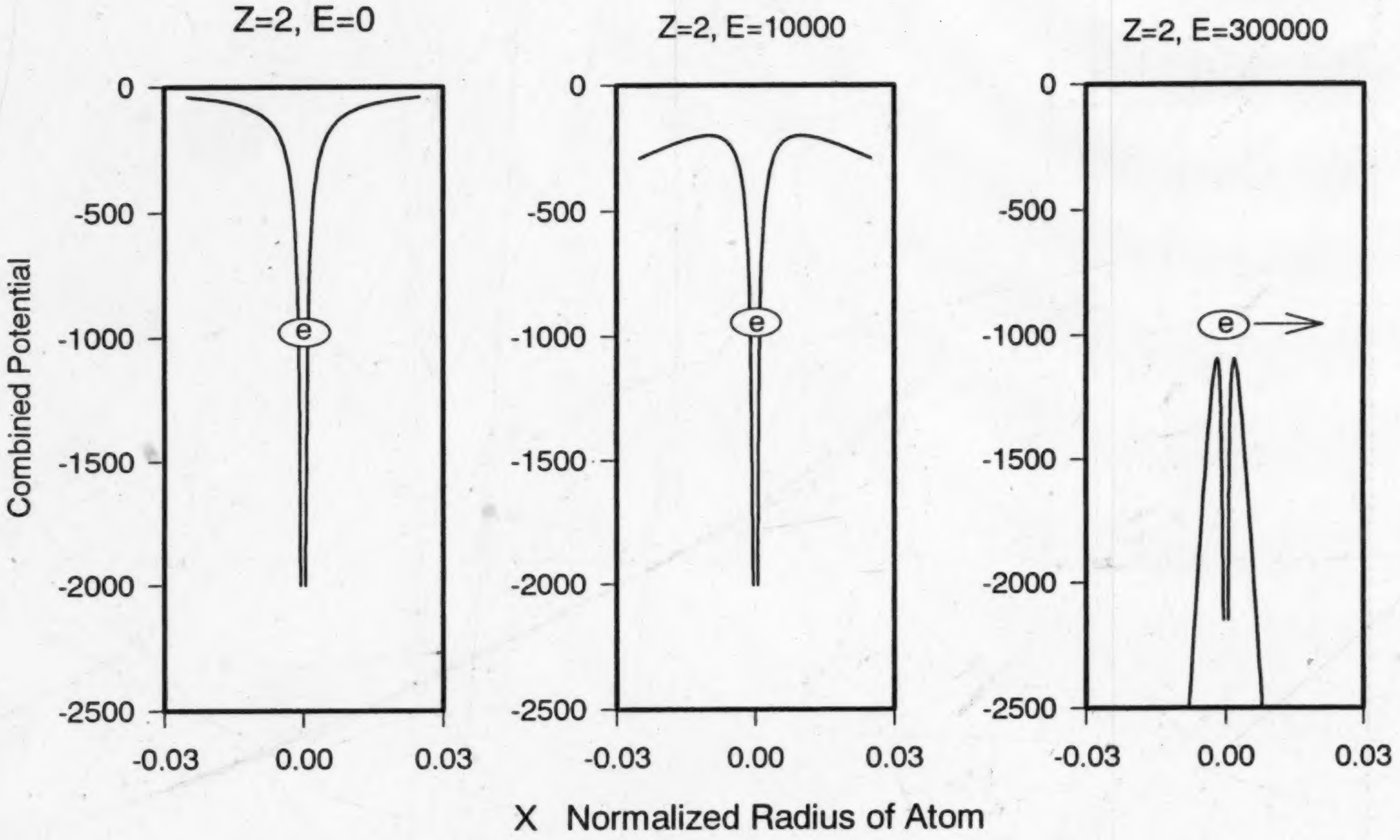

Fig. 2-3. Potential barrier suppression and electron tunneling. E is the normalized electric field strength.

Chapter 3

General Experimental Methods and Instrumentation

3.1 Outline of the experiments

The experimental measurements presented in this thesis involve four separate projects. They are briefly outlined in the following and described in more detail in following chapters of the thesis.

3.1.1. Visible single-shot two-photon autocorrelator of KrF laser pulse in BaF_2

In this project, a single shot autocorrelator was developed to measure the pulsewidth of the subpicosecond KrF laser pulses. This technique utilized the two photon fluorescence in BaF_2 crystal in a colliding pulse geometry. However, instead of using the ultraviolet fluorescent emission, the visible emission ranging from 400 to 450 nm was used for the first time in such a measurement. The measurement was carried out by imaging the visible emission onto a 1-D array optical multichannel analyzer (OMA) system. The fluorescence spectrum of BaF_2 was first characterized under irradiation with high intensity KrF laser light. A novel method utilizing the two photon fluorescence itself was also used to obtain the two photon absorption coefficient for BaF_2.

3.1.2 Multiphoton ionization formed plasma columns in a static fill gas cell.

Initial interaction experiments were carried out in a large chamber filled with a number of gases at pressures of a few torr up to one atmosphere. In these experiments, the breakdown thresholds of helium, air and argon were first measured. Then the plasma columns formed in helium, air and argon with a 6 ps KrF laser pulse at irradiation intensities of 10^{14}-$1.2\text{x}10^{15}$ were studied by using a 496 nm probe beam to record shadowgrams of the evolving plasma profiles over a time period of several nanoseconds after initial breakdown. The absorption and scattering of laser radiation were subsequently measured as a function of the input laser energy. The shift of the breakdown point and refraction of the laser beam due to defocusing in the plasma were identified and characterized.

3.1.3 Characterization of a high density gas jet

To reduce the refraction of ultrashort high intensity laser beams propagating through a static gas cell, a high density gas jet was developed for the laser plasma interaction experiments. The 3-dimensional density profiles of the 1 mm diameter high density gas jet were characterized using laser interferometry and Abel inversion of the resultant interferograms. A simple empirical formula for the density along the axis of the jet was found in terms of the reservoir fill pressure.

3.1.4 Laser plasma interaction in a high density gas jet

A series of experiments were conducted to examine the propagation of ultrashort high intensity laser pulses (1 ps, 10^{17} W/cm^2 vacuum intensity) through the high density gas jet.

- Beam propagation

  UV side scattering. Along the direction perpendicular to laser beam, the side scattered laser light was imaged onto a streak camera to monitor the beam propagation. The camera was streaked to give a framing image of the picosecond scattered light in order to discriminate against the scattered light from within the chamber.

  Visible emission. To monitor the subsequent formation of the plasma columns in helium gas, the visible emission profile was imaged onto a silicon intensified target (SIT) camera using the emission of He II 4-3 transition line at 468.5 nm. Only emission around this wavelength was observed by placing an interference filter with a 1.5 nm bandwidth in front of the camera. In this way, the region of highly ionized helium can be found since the emission occurs primarily upon recombination of fully ionized helium in the cold multiphoton ionized plasma.

- Spectral diagnostics of beam propagation

  The emission line of He II at 468.5 nm was measured using a 0.57 m monochromator in three directions of 0, 90, and 135 degrees relative to the forward direction of the incident laser beam which was taken as 0 degrees. The aim was to monitor the He II emission from the rear, middle, and front of the gas jet and to infer the beam interaction with the plasma. Particularly, the spectra at 0 degrees which monitors plasma at the exit of the gas jet reveals whether ionization has occurred throughout the gas jet to the exit point or whether the beam is refracted to such a degree that the intensity is not sufficient to fully ionize helium.

- Refraction

  The refraction of the input laser beam was measured by imaging the transmitted laser radiation at various positions through the gas jet onto a CCD camera. There were two kinds of experiments. First, with the laser beam being focused at the center of the jet, the center of the gas jet was imaged onto a CCD camera. This setup checked whether the entire laser beam comes to a focus at the mid point of the gas jet as it would in vacuum. If not, an enlarged image would indicate refraction of the input beam prior to the focal point, thus leading to the reduction of the peak intensity. Second, to determine the asymptotic angle of refraction, the beam spot size at the exit of the jet was also measured. By analysis of the spot size at these two positions, the refraction of the beam after exiting the plasma can be determined.

- Absorption and energy transmission

  When the laser beam ionizes the gas, the energy in the laser beam is reduced because of absorption and scattering. To monitor the overall reduction of transmission of the pulse energy through the gas jet, a pair of calorimeters were used. One of them measured the input energy while the other measured the transmitted energy. By cross-calibration with vacuum shots, the absolute transmission was obtained.

- Spectral blueshift of the transmitted radiation

The modification of the spectrum of the laser beam after propagating through and ionizing the gas was measured using a monochromator coupled with an OMA. This diagnostic revealed information on the rapid ionization dynamics of the laser plasma interaction which leads to a blue shift in the transmitted spectrum. The blue-shifted spectrum of the KrF laser radiation was measured at various gas densities for helium, neon, argon and nitrogen gases. The blue-shifted spectrum of the angularly scattered radiation was also measured.

3.2 Picosecond laser facility

Ultrashort excimer laser pulses at 248 nm are generally obtained by amplification of seed pulses generated by frequency mixing or tripling of pulses from mode-locked lasers. Such systems are quite complex and require several laser modules which must work together properly. The laser system used in the present project is a simple ultrashort pulse system fabricated at the University of Alberta [1]. The front end of the system, shown in Fig. 3-1, is based on a XeCl laser pumped dye laser system and is similar to the system developed by Szatmari and Schafer a few years ago [2]. This system differs from other systems mainly in that the generation of a subpicosecond pulse is accomplished by the cascade shortening of pulse length through a quenched resonator (QR), short cavity dye laser (SCDL), and distributed feedback dye laser (DFDL). The output of this system is frequency doubled and amplified in a KrF discharge laser module to obtain a short pulse (~ 0.8 ps) at 248.5 nm. An earlier version of this system running with a pulse length of 6 ps was used for the initial experiments in a static gas cell (presented in Chap. 5). For the final set of experiments using the gas jet target, an e-beam amplifier system was used to further amplify the UV short pulse to higher powers of ~ 0.25 TW. In the following, each part of the system will be described briefly.

The short pulse generation starts with a QR dye laser pumped by a XeCl excimer laser module whose output at 308 nm is split four times to pump different stages of dye amplifiers. The QR begins by generating a train of pulses at the wavelength of 340 nm due to the relaxation oscillation following gain Q switching. The first spike of the oscillation can be selected by placing a slightly tilted long resonator outside the inner short resonator (in this case the dye cell itself) . In this way, the inner short cavity has a low Q and begins to generate the first pulse very quickly while the long cavity with high Q (hence high round trip gain) and long rise time is designed such that it will take over and deplete the gain completely after the production of the first short cavity pulse, thus suppressing the rest of the oscillation in the inner cavity. The pulses from the two cavities can be spatially separated because of the angular misalignment of the two cavities. The output pulse length is on the order of 150 ps.

The next stage of pulse length reduction employs a short cavity dye laser (SCDL) which has a cavity length of 0.5 mm and hence a rise time of ~10 ps. The resonator of SCDL is formed by two dichroic mirrors (edge filters) the first of which has high transmission for the incoming beam (approximately 10% reflectivity at 340 nm), but has near 100% reflectivity at 465 nm, the lasing wavelength of the dye. The second dichroic mirror has a high reflectivity for the pump beam and partial reflectivity at the lasing wavelength to allow output of the lasing radiation. These two mirrors act as dye cell windows with a 0.5 mm teflon spacer separating them. It is known from the theory of gain switched lasers that SCDL is capable of generating significantly shorter pulses than the pump pulse. The output pulse from this stage which is of the order of 30 ps in duration is amplified once (by AMP1) to raise its energy to such a level that it can pump the following DFDL efficiently.

The final stage of generating a subpicosecond pulse takes advantage of the DFDL, the part enclosed by a dashed box as shown in Fig.3-1. As the name implies the optical feedback is provided by Bragg reflection from a periodic spatial structure in the complex refractive index in the gain medium rather than the conventional mirror cavity. This spatially periodic structure can be created by the interference of two pumping beams. In the implementation of this technique, the pump beam from the SCDL is expanded through a cylindrical lens telescope to form a pencil-like illumination of an amplitude transmission grating. A microscope objective is used to create an image of the grating in the dye solution. In normal operation, the zeroth order is blocked by a stop and the plus and minus first orders are transmitted through the microscope objective and emerge as two beams with an angle between them to produce an interference pattern (image of the grating). The laser wavelength is determined by the period of the interference pattern and the refractive index of dye solution. The laser wavelength can be tuned by changing the position of transmission grating relative to the microscope objective which effectively changes the demagnification ratio. An important feature of the DFDL is that its output is significantly reduced in pulse width compared to the duration of the pump pulse. A pulse with duration of 500 femtosecond can be achieved, being 60 times shorter than the pump pulse.

It can obviously be seen that all of the above mentioned lasing and amplifying systems are synchronously pumped by one XeCl excimer laser, thus avoiding the complexity of synchronization among a number of different laser modules as is necessary for other systems. Another advantage of the present system is that only one pulse is generated per laser shot, requiring no electro-optic switching techniques.

The output of the DFDL is usually very low in energy. It undergoes two stages of amplification which increase its energy enough to obtain efficient frequency conversion to the ultraviolet at 248 nm. In the amplifier chain, a saturable absorber is added to suppress the amplified spontaneous emission and clean up the pulse shape. The frequency-doubled pulse is subsequently amplified in a double pass geometry through a KrF amplifier module. A spatial filter in an evacuated chamber is inserted in between the passes to block amplified spontaneous emission generated in the first pass and improve the spatial quality of the beam. With the above front end system, a pulse of 800 femtoseconds with energy of up to 50 mJ at 248 nm can be generated.

For the gas jet target experiments the ultrashort laser pulse from the front end is fed into an electron beam pumped amplifier [3] as shown in Fig. 3-2. It consists of two pulse power modules (Marx banks and Blumlein pulse forming lines) which generate electron beams to pump the laser cavity from opposite sides. By triple passing the amplifier, the system can deliver a pulse energyof ~250 mJ at the target chamber with a duration of 1 ps at 248.5 nm. The output beam has a size of 4.1 cm by 5.2 cm at the entrance to the target chamber. The experiments were conducted inside a sealed vacuum chamber which was evacuated to a base pressure of ~ 10 mTorr prior to back filling with gas or firing on the short pulse gas jet. When the laser beam was focused by an aspheric quartz doublet lens of 20 cm focal length, it produced a spot size in vacuum of 18 μm, giving an intensity of ~ 10^{17} W/cm^2 . The whole laser system is controlled by a computer controlled firing system. The energy and pulse length were monitored every shot and the data was captured by a computerized data acquisition system.

3.3 Laser diagnostics

The accurate determination of the laser parameters is important in order to properly interpret the experimental data. The focal spot size of the laser beam was measured using the same imaging system as for refraction measurements. This will be discussed in detail in Chapter 7 together with the axial intensity distribution through the interaction region. The pulse length measurement will be presented in Chapter 4.

3.4 Target Chamber and Diagnostics

During the course of the project, two main target chambers were used. The detailed layout of diagnostics and their operating conditions will be discussed in the corresponding experimental sections. For the gas jet target experiments an additional gas exhaust system was developed on one of the chambers in order to maintain a reasonable vacuum. A funnel with a solenoid driven shutter was placed 3 mm above the nozzle tip of the gas jet. The funnel collected and diverted the gas plume through a plastic tube of 5 cm in diameter to a separate large evacuated chamber of roughly the same size as the target chamber. The solenoid shutter was designed such that it would close the tip of the funnel after the main gas jet finished puffing, avoiding backstreaming of the gas from the secondary chamber. The solenoid was triggered 120 ms after firing the gas jet to have the smallest amount of gas leaking back out into the main chamber. In this manner the vacuum was kept below 80 mTorr when firing the gas jet at the highest working reservoir pressure of 1500 psi.

References

1. J. N. Broughton and R. Fedosejevs, J. Appl. Phys. 71, 1153 (1992). J. B. Broughton, Ph. D thesis, University of Alberta, 1993.

2. S. Szatmari and F. P. Schafer, Opt. Commun. 68, 196 (1988).

3. D. C. Thompson, R. Fedosejevs, A. A. Offenberger, J. P. Santiago, and H. R. Manjunath, IEEE Quantum Electron. 25, 2161 (1989).

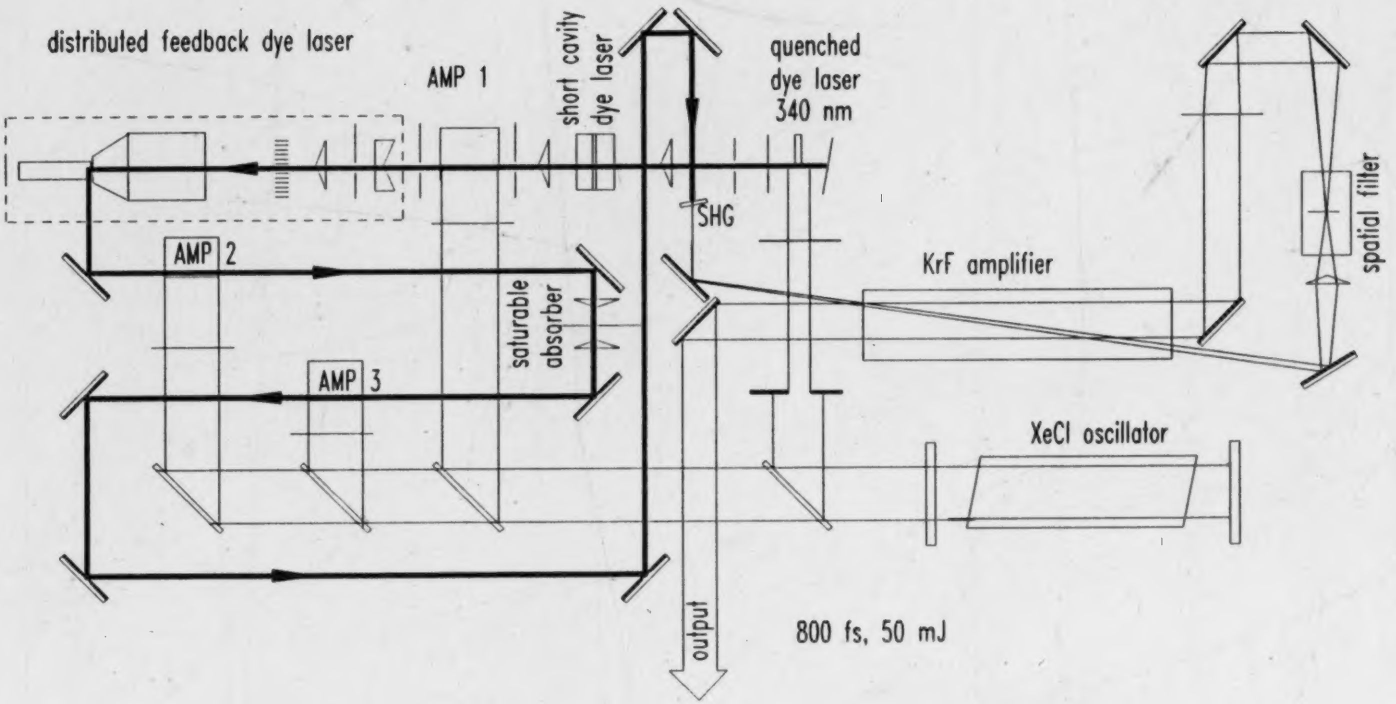
distributed feedback dye laser
AMP 1
short cavity dye laser
quenched dye laser 340 nm
SHG
AMP 2
saturable absorber
AMP 3
KrF amplifier
spatial filter
XeCl oscillator
output
800 fs, 50 mJ

Fig. 3-1 Picosecond KrF front end laser system

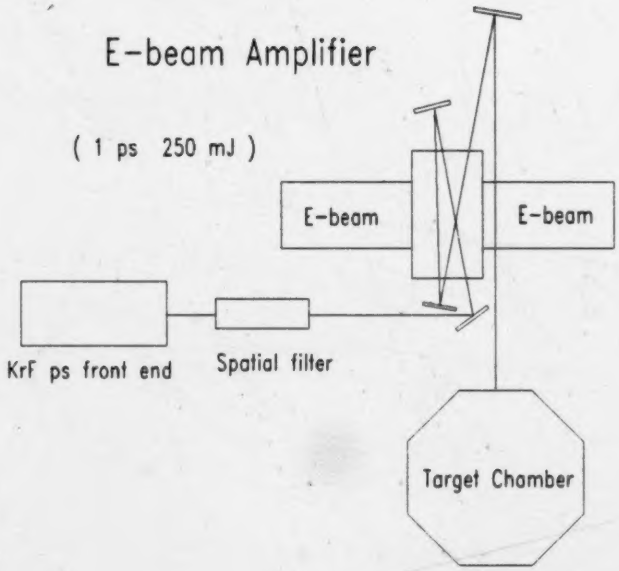
E-beam Amplifier
(1 ps 250 mJ)
E-beam
E-beam
KrF ps front end
Spatial filter
Target Chamber

Fig. 3-2 Electron beam pumped KrF laser amplifiers

Chapter 4

A Visible Single Shot Autocorrelator in BaF_2 for Subpicosecond KrF Laser Pulses

The study of high power KrF lasers has been an area of interest in recent years motivated by potential applications such as the pumping of X-ray lasers and the study of high-field radiation-matter interaction. As the laser pulse widths employed become shorter, into the femtosecond regime, there is a great need to quantitatively characterize the temporal duration in a simple way on a daily basis. Many multi-shot and single shot correlation techniques have been developed for ultrashort pulse measurements [1-4]. For high power KrF lasers at 248 nm, it is generally not convenient to use a multi-shot technique which requires many shots to finish one measurement since most of the high power KrF laser systems are operated at relatively low repetition rates. Single shot methods have been developed to overcome this problem based on detection of visible three-photon fluorescence at 480 nm of XeCl [4], two photon fluorescence at 508 nm of metal vapor in a heat pipe [5], or two photon fluorescence of Xe in the ultraviolet at 172 nm in a gas cell [6]. Most recently, UV emission of two-photon-excited excitonic fluorescence (TPEF) of BaF_2

at 310 nm was used as a detector for phase-sensitive UV autocorrelators [7,8]. These systems either have to deal with a gas cell and associated filling system or must use a UV detection system which is not so convenient to work with.

In this chapter we present an extension of the technique based on emission of TPEF in BaF_2 to the visible region for the first time. This results in a visible autocorrelator for KrF lasers based on the emission of TPEF of BaF_2 crystal in the range of 400-450 nm. The measured spectrum shows broad band emission from 280-450 nm. Using a narrower band of this emission either around 400 nm or 310 nm we have observed a quadratic dependence of TPEF on the pumping intensity. Nearly 3:1 contrast ratio in the correlation traces based on emission around 400 nm was achieved confirming the quadratic dependence. In the course of this investigation, a novel method based on the TPEF intensities was also developed to measure the two photon absorption coefficient.

4.1 Visible single shot autocorrelator in BaF_2

The luminescence of self trapped excitons in alkali halides has been studied by Beaumont [9] and Williams [10] in detail using X-ray and electron beam excitation respectively. The self-trapped excitons formed by two-photon absorption have also been investigated by using the fourth harmonic of a Nd:YAG laser [11] and a subpicosecond KrF laser [12]. In reference 12, Hata et al. studied the luminescence spectra of self-trapped excitons in CaF_2 and MgF_2. They demonstrated that the fluorescence intensity of self-trapped excitons in CaF_2 shows a nearly quadratic dependence (slope 1.9) on the input KrF laser intensity. This result was used to construct an autocorrelator and measure the pulsewidth of their subpicosecond KrF laser.

For BaF_2, with a band gap of 9.1 eV, it is expected that there will be more efficient two photon excitation for KrF photons of energy 5eV compared to the 10 eV band gap of CaF_2. [13,14] . There may be other mechanisms for loss of laser energy as a result of two photon excitation other than self-trapped excitonic fluorescence, such as photon-phonon interaction and color center formation. The intensity dependence of these other mechanisms may alter the quadratic dependence of two photon absorption. In addition, the two photon absorption itself can broaden the pulse width as the input intensity becomes very high.

To take advantage of the two photon fluorescence in BaF_2, the spectrum of the KrF laser induced fluorescence was measured. The KrF laser system is a hybrid system utilizing a distributed feedback front end dye laser and a double pass KrF amplifier module [15] . It can generate a pulse of 800 fs duration and energy up to 50 mJ at 248 nm. The laser beam has a uniform area of $32x12\ mm^2$. Only a part of the output beam, 6 mm in diameter, was used in the present experiments. The beam was weakly focused onto the BaF_2 sample giving intensities in the range of 10-100 GW/cm^2 . The fluorescence was imaged onto a prism spectrograph which has a 50 μm wide slit, giving a resolution of 0.2 nm. The spectrum was recorded on a Kodak 103 photographic plate which was sensitive from 200 - 500 nm. The exposed plate was scanned with a scanning microdensitometer and processed to give a corrected spectrum after all the response functions were taken into account. A typical spectrum is shown in Fig. 1. It is similar to those obtained before [7,8,11,12]. It has a peak around 290 nm and has a long tail reaching up to 450 nm into the visible region.

In order to use the autocorrelation technique from the visible spectra around 400 nm, the square law of fluorescence yield against the incident laser intensity on the sample was verified. The most recent published references [7,8] have checked the square law dependence for wavelengths from 290 nm to 370 nm. The present experiment checked the whole spectral range up to 440 nm. Similar results were obtained for spectra below 370 nm as reported previously. The measured fluorescence yield at 400 nm is plotted in Fig. 2 as a function of laser intensity. In this case a bandwidth of 5 nm was used to increase the detection efficiency. It can be seen that a slope of 1.98 ± 0.05 is obtained which is nearly 2. Thus, the square law is well satisfied around 400 nm for intensities below 100 GW/cm^2.

A single shot autocorrelator using the visible fluorescence at 400 nm was constructed with a triangular configuration as shown in Fig. 4-3. The laser beam was gently focused before being split into two beams of equal intensity. The two beams were steered to collide collinearly inside a BaF_2 crystal, resulting in an autocorrelation trace. The trace was imaged using a visible f/1.8 camera lens with a filter of 5 nm bandwidth at a central wavelength of 400 nm onto an optical multichannel analyzer (OMA) and the resultant trace displayed on an oscilloscope. A typical trace is shown in Fig. 4-4. It corresponds to a pulse width of 850 fs assuming a Gaussian pulse shape profile. The shoulder part of the trace reflects the total length of the crystal and thus gives an absolute calibration of the pulse length. The time resolution of the system is mainly limited by the imaging system. The present system has a resolution corresponding to a pulse width of 100 fs. With a higher magnification imaging system, less than 50 fs resolution should be obtainable.

4.2 Two photon absorption coefficient in BaF_2

The nonlinear absorption coefficient of BaF_2 is an important parameter in studying two photon absorption phenomena. With the square law of the two photon fluorescence, a novel method using the fluorescence intensity was employed to measure the two-photon absorption coefficient in BaF_2. It used the same setup as shown in Fig. 3 for the autocorrelation measurement except that only one beam was allowed to be incident on the crystal while the other beam was blocked. A typical fluorescence trace is shown in Fig. 5 for a laser beam incident from the left on the crystal. The horizontal direction is the distance along the crystal and the vertical axis is the fluorescence yield. If a coordinate system is chosen with an origin such that x=0 is at the left edge of the crystal and x=L at the right edge of the crystal. With the above square law, we have the following relation

$$I_F(0^+) = \alpha I_L^2(0^+) \qquad (1)$$

$$I_F(L^-) = \alpha I_L^2(L^-) \qquad (2)$$

where $I_F(0^+)$ and $I_F(L^-)$ are the fluorescence intensities at just inside the left and right edges of the crystal respectively. $I_L(0^+)$ and $I_L(L^-)$ are the laser intensities at just inside the left and right edges of the crystal respectively and α is a constant. Thus we have

$$I_L(L^-)/I_L(0^+) = \sqrt{I_F(L^-)/I_F(0^+)} \qquad (3)$$

The ratio of $I_F(L^-)/I_F(0^+)$=0.49, which is obtained from the fluorescence intensities in Fig. 5. Thus, $I_L(L^-)/I_L(0^+)$=0.70. For an initial analysis, assume that the pulse is spatially uniform, temporally flat-topped and that two photon absorption dominates following the relation of $dI/dz = -\beta I^2$. For a sample of thickness L with reflectivity R at each surface, the resultant ratio of the laser intensities inside the crystal is

$$\frac{I_L(L^-)}{I_L(0^+)} = \frac{1}{1 + I_{in}(1-R)\beta L} \qquad (4)$$

Where I_{in} is the laser intensity incident on the crystal surface and β is the absorption coefficient. Taking the appropriate parameters for the case shown in Fig. 5, with L =.509 mm, R=0.04, and I_{in}=10 GW/cm^2 we obtain β=9x10^{-11} cm/W. If a more realistic assumption is made that the incident beam has a Gaussian temporal profile given as $I(t) = I_0 \exp(-t/\tau)^2$ but is still spatially uniform, then the fluorescence intensity ratio is given by integrating over the pulseshape:

$$\frac{I_F(x=L^-)}{I_F(x=0^+)} = \frac{\displaystyle\int_{-\infty}^{\infty}\left(\frac{e^{-x^2}}{1+\beta L\,(1-R)\,I_0\,e^{-x^2}}\right)^2 dx}{\displaystyle\int_{-\infty}^{\infty} e^{-2x^2}\,dx} \tag{5}$$

Using the same parameters as above, this yields the absorption coefficient $\beta = 1.1 \times 10^{-10}$ cm / W. This is 30% larger than that obtained using a flat-top pulse shape. In the present setup, there was a systematic error due to the focusing of the beam where the crystal was located 83.5 cm away from the focusing lens of 100 cm focal length. Using geometric ray tracing, the beam area at X=L is reduced by 6%, thus yielding an increase of the fluorescence yield at the exit face of 6%. Taking account of this correction by equation (5), we have $\beta = 1.26 \times 10^{-10}$ cm / W. The other source of error of the measurement is mainly from the uncertainty of the absolute input laser intensity I_{in}. In the present experiment, the energy of the incident laser beam was monitored by a photodiode which was calibrated against a Gentec calorimeter. The pulsewidth was measured as above and the diameter calculated by geometric ray tracing. The estimated absolute uncertainty for the absorption coefficient is 30 %. In terms of above best estimates, we have $\beta = 1.3 \pm 0.4 \times 10^{-10}$ cm / W which is in good agreement with the value reported by Taylor et al.[13] ($\beta = 1.1 \times 10^{-10}$ cm / W with an uncertainty of 50 %).

In conclusion the two photon fluorescence spectrum of BaF_2 crystal induced by KrF laser pulses has been measured. The square law dependence of the fluorescence yield is verified for the entire emission spectral range, particularly for the visible spectra around 400 nm. A single shot autocorrelator using the visible emission at 400 nm is successfully implemented with a resolution of 100 fs for pulse width measurement and a method using the two photon fluorescence intensity is employed to measure the two photon absorption coefficient for BaF_2 at 248 nm.

References

1.J. A. Giordmaine, P. M. Rentzepis, S. L. Shapiro, and K. W. Wecht, Appl. Phys. Lett. 11, 216 (1967). J. R. Klauder, M. A. Duguay, J. A. Giordmaine, and S. L. Shapiro, Appl. Phys. Lett. 13, 174 (1968).

2.S. Szatmari and F. P. Schafer, Opt. Commun. 68, 196 (1988).

3.H. E. Rowe and Tingye Li, IEEE Quantum Electron. QE-6, 49 (1970).

4. N. Sarukura, M. Watanabe, A. Endoh, and S. Watanabe, Opt. Lett. 13, 996 (1988).

5. A. Tunnermann, H. Eichmann, R. Henking, K. Mossavi, and B. Wellegehausen, Opt. Lett. 16, 402 (1991).

6.M. H. R. Hutchinson, I. A. McIntyre, G. N. Gibson, and C. K. Rhodes, Opt. Lett. 12, 102 (1987).

7.S. P. Le Blanc, G. Szabo, and R. Sauerbrey, Opt. Lett. 16, 1508 (1991).

8.K. Osvay, I. N. Ross, C. J. Hooker, J. M. D. Lister, Appl. Phys. B59, 361 (1994).

9.J. H. Beaumont, W. Hayes, D. L. Kirk and G. P. Summers, Proc. Roy. Soc. Lond. A 315, 69 (1970).

10. R. T. Williams and M. N. Kabler, Phys. Rev. B 14, 725 (1976).

11. R. T. Williams, J. N. Bradford, and W. L. Faust, Phys. Rev. B 18, 7038 (1978).

12.K. Hata, M. Watanabe, and S. Watanabe, Appl. Phys. B 50, 55 (1990).

13. A. J. Taylor, R. B. Gibson, and J. P. Roberts, Opt. Lett. 13, 814 (1988).

14. P. Simon and H. Gerhardt, and S. Szatmari, Opt. Lett. 14, 1207 (1989).

15. J. Broughton, Ph. D. thesis, University of Alberta, 1992.

16. J. I. Dadap, G. B. Focht, D. H. Reitze, and M. C. Downer, Opt. Lett. 16, 499 (1991).

17. H. Sakai, K. Miyazaki, and G. U. Kim, J. Opt. Soc. Am. B 9, 2015 (1992).

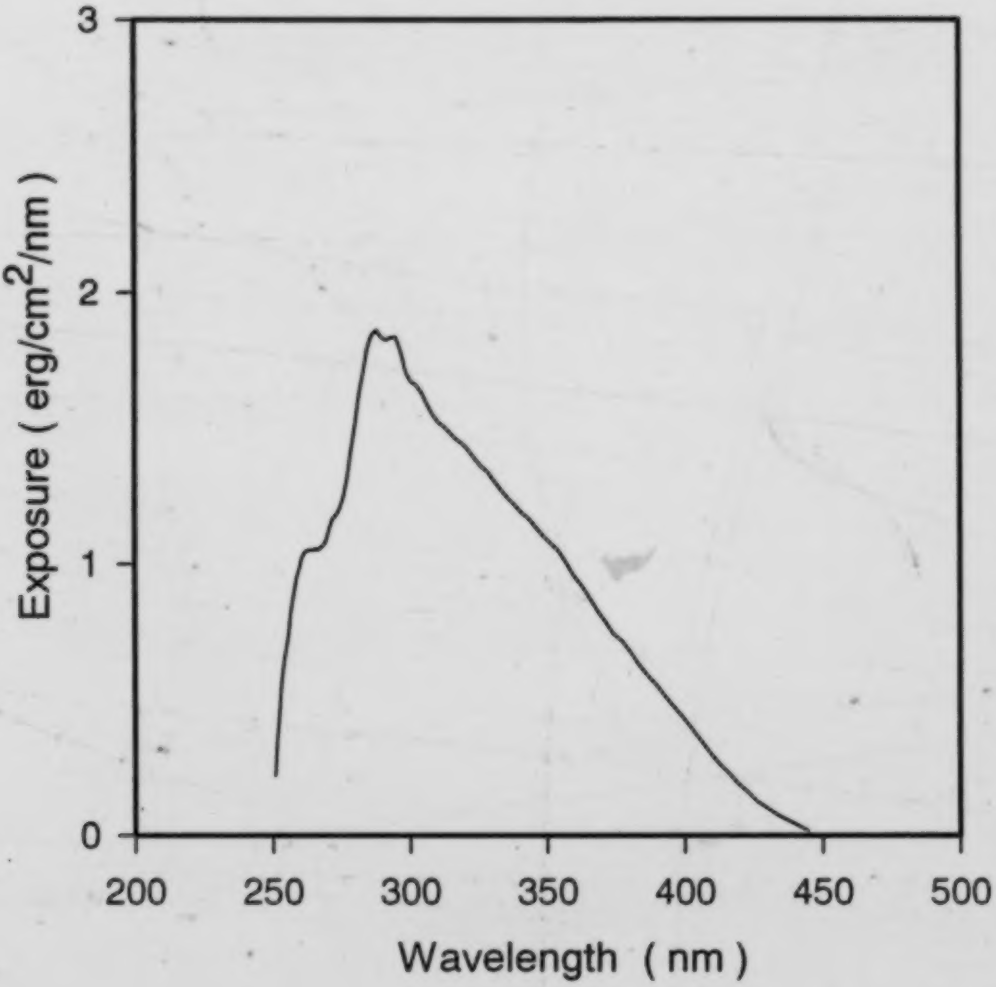

Fig. 4-1 Measured spectrum of two-photon excited fluorescence from BaF_2.

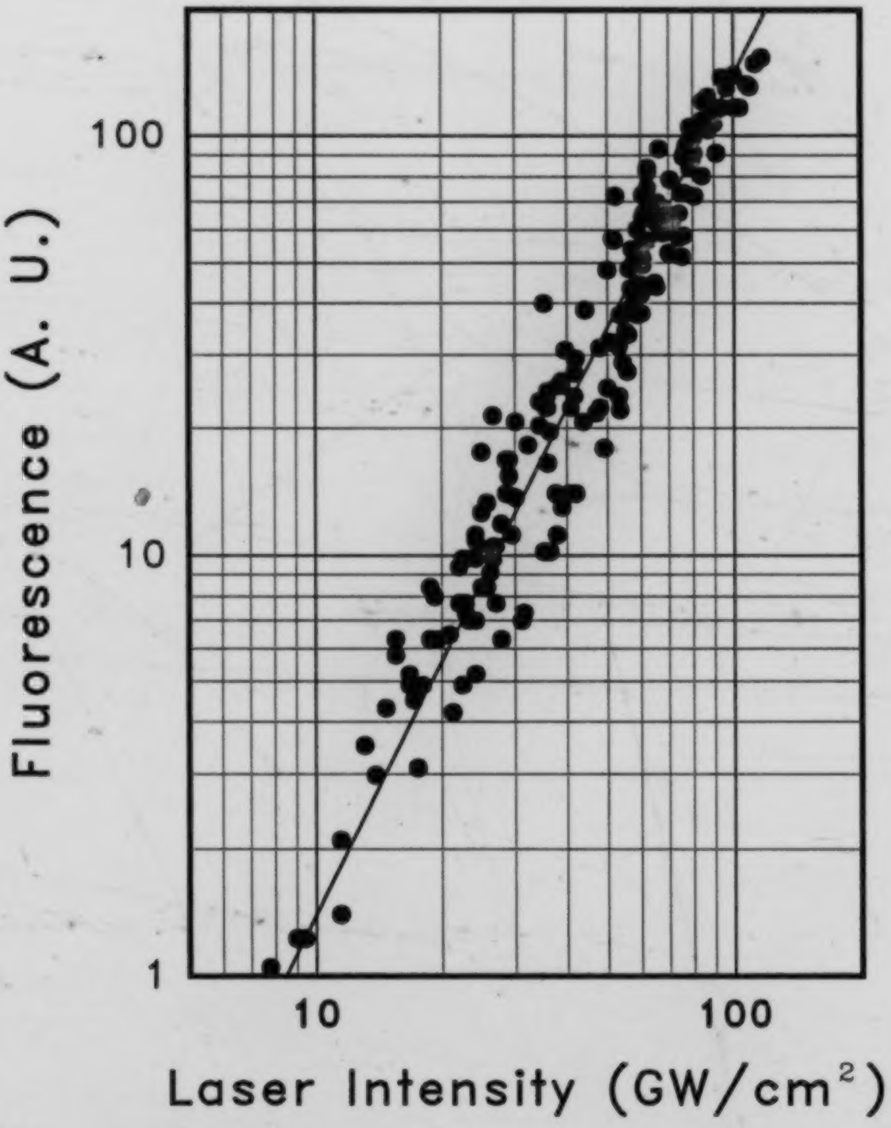

Fig.4–2 Dependence of the BaF_2 fluorescence at 400 nm on the exciting laser intensity. The solid line is a least square best fit with a slop of 1.98± 0.05.

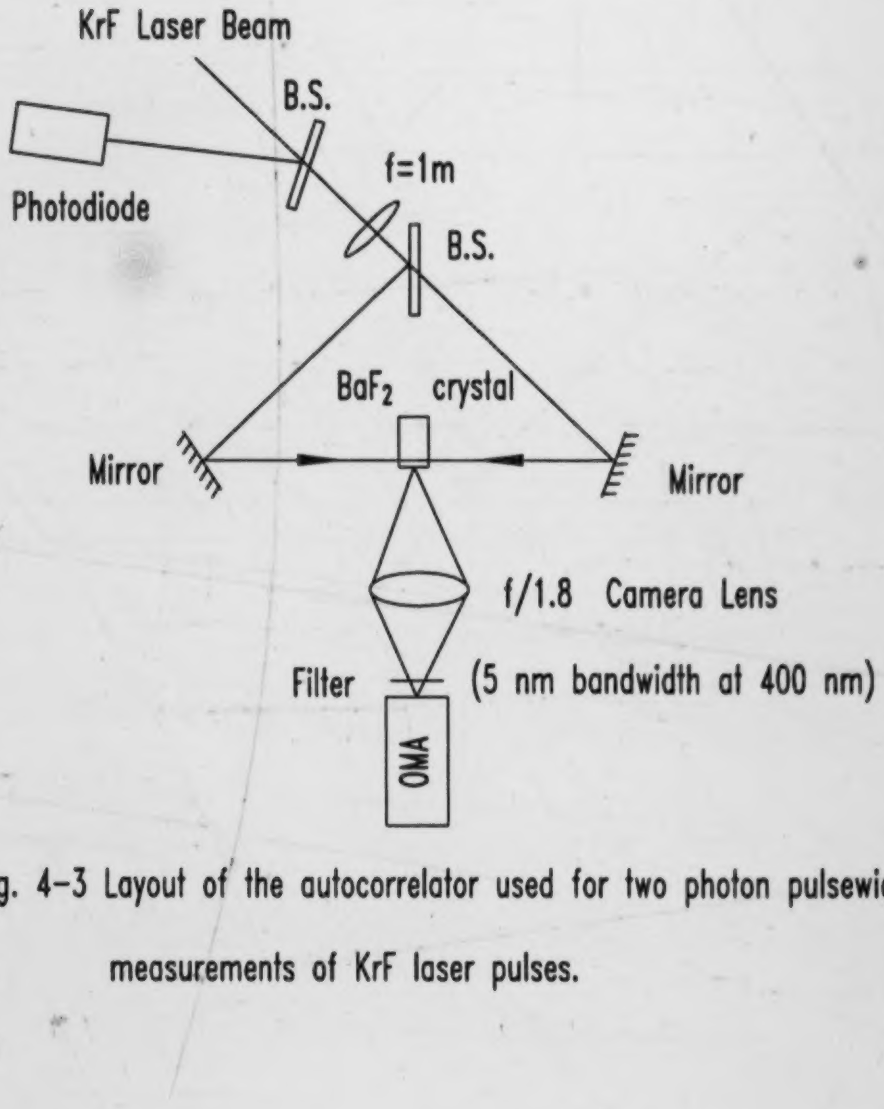
KrF Laser Beam
B.S.
Photodiode
f=1m
B.S.
BaF$_2$ crystal
Mirror
Mirror
f/1.8 Camera Lens
Filter
(5 nm bandwidth at 400 nm)
OMA

Fig. 4-3 Layout of the autocorrelator used for two photon pulsewidth measurements of KrF laser pulses.

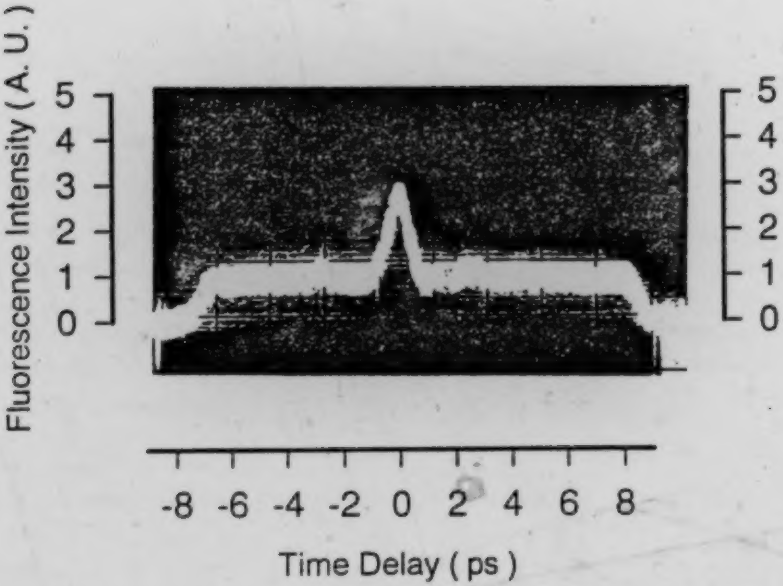

Fig.4-4 Oscilloscope display of a measured autocorrelation trace. The measured full width of the fluorescence signal is 1.2 ps, yielding a pulsewidth of 850 fs assuming a Gaussian pulse shape.

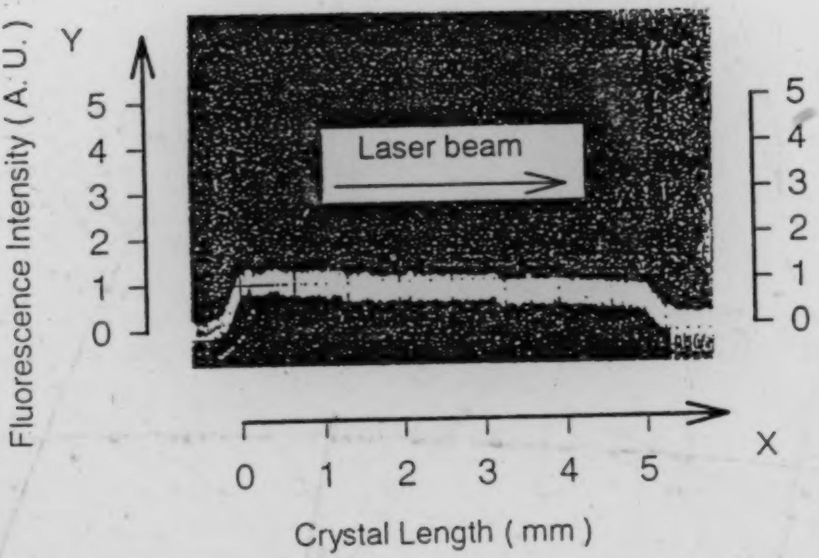

Fig. 4-5 A fluorescence trace across the BaF_2 crystal irradiated from one side with a KrF laser pulse.

Chapter 5

Formation of Plasma Columns in Atmospheric Pressure Gases by Picosecond KrF Laser

5.1. INTRODUCTION

In recent years there has been considerable interest in the process of multiphoton ionization of gases with ultrashort laser pulses at high intensities [1-6]. In particular, it may be possible to achieve very high ionization states in a cold background plasma and possibly achieve population inversion and gain in the XUV spectral region [7-10]. A multiphoton ionization pumped laser scheme has already been demonstrated at low pressures in cadmium vapour producing output at 508nm [11]. It has also been proposed that very high intensities ~10^{20} W cm^{-2} might be obtained using the process of relativistic self focusing [12-14]. The formation and stability of such self focussed channels has not as yet been demonstrated experimentally.

In order to achieve significant gain length products for radiation in the XUV range, plasmas with electron densities of $n \sim 10^{19}$ -10^{21} and gain lengths of $L_{mm} = 1$ - 10 mm will be required [10]. Such densities could be achieved in gaseous targets at pressures in the range of 1-10 atm which would be advantageous compared to solid targets for high repetition rate operation. The achievement of the required high pump intensities, $I > 10^{16}$ Wcm^{-2}, over a length L_{mm} millimeters in a standard sideways irradiated line focus geometry would require a pump laser power of $P > 500\ L_{mm}$ GW assuming a 5 μm focal width. The energy absorbed from the pump beam traversing a 5 μm interaction region for a gaseous target and resultant efficiency for such a line focus geometry would probably be very small. Alternatively, using an optimum diffraction limited axial focal geometry would require a pump laser power of $P > 12.4\ L_{mm}$ GW to achieve an intensity of $I > 10^{16}$ Wcm^{-2} over a length of L_{mm} for a wavelength of 248nm. However, diffraction limited propagation over a length of a few millimeters will be very difficult to achieve due to refraction as has been calculated numerically [14] and as will be shown below. The ideal pump scheme would be to focus the pump radiation into the end of a narrow lightguide which would maintain the pump intensity over a long gain length. In such a case a pump power of $P > 2$ GW would suffice to achieve $I > 10^{16}$ Wcm over absorption lengths of a few millimeters, again assuming a 5 μm focal spot. Clearly there is a significant advantage in pump efficiency for such a scheme if it could be achieved.

For gaseous target species one could create a plasma guiding channel of small transverse dimensions using multiphoton ionization by a precursor laser pulse in a line focus geometry or a larger diameter channel using an axial focal geometry. The subsequent radial expansion of the hot plasma will leave a lower gas density in the hot center and higher gas density on the walls. If this partially ionized density profile is further ionized through multiphoton ionization using a high intensity subpicosecond pulse the electron density profile will have a minimum density on axis giving a refractive index guiding channel similar to a light fiber. Generally a much lower intensity would be required for a precursor pulse to form such a channel so that the efficiency of absorption would not be a major concern. In order to explore some of the issues involved in the creation of such plasma columns and the refraction of light by a multiphoton ionized plasma we report here experimental investigations of the case of axial focussing using a large f/number lens.

In particular, the present paper describes experiments to investigate the breakdown of gas with high intensity short duration uv laser pulses in order to form plasma columns in gases at close to atmospheric pressure . The primary diagnostics used were energy balance measurements, time resolved shadowgraphic imaging of the plasma, time integrated images of plasma self emission and measurements of scattering of the transmitted radiation. Argon and helium were investigated because of the availability of data on multiphoton ionization of these gases and air was studied as an example of a more complex molecular gas system. The conditions required for XUV multiphoton ionization pumped recombination lasers generally require densities of 10^{19}-10^{21} cm^{-3}. These conditions are much different than the low pressure collisionless regime in which multiphoton ionization has recently been studied. It was expected that breakdown would be initiated by multiphoton ionization and given sufficient time would subsequently avalanche by collisional ionization [16-17] . At the same time the initial plasma electron density would form a refractive index gradient which would deflect the light from its original focal point. The present investigation was designed to study the interaction of these various processes and their effect on the formation of long plasma columns which would subsequently expand into plasma channels.

The rest of this paper is organized as follows: Section 2 deals with the details of the experimental system for plasma production, shadowgraphy and energy balance measurements, Section 3 presents the experimental results, Section 4 discusses the results and Section 5 presents some conclusions.

5.2. EXPERIMENTAL DETAILS

A schematic diagram of the experimental setup is shown in Fig. 5-1. There are two laser beams going into the target chamber, the main UV laser beam and a low energy green probe beam. The UV laser pulse was focused by a triplet lens to breakdown the gas inside the interaction chamber while the green probe beam was used to produce shadowgrams of the plasma formed. The images of the shadowgrams were recorded using a video digitizer and stored in a computer. The energies of the UV beam before and after the focal point were monitored by using two cross calibrated calorimeters, C1 and C2, respectively. The ultrashort, high intensity KrF laser system has been described in detail elsewhere [18] . However, for the present experiment the front end dye laser pulses have been further shortened with the addition of a short cavity dye laser and a distributed feedback laser [19] to produce uv pulses with energies up to 50 mJ and durations of around 6 ps. In order to ensure a uniform input beam and a well defined interaction geometry, the main UV pulse used in the present experiments was limited to 12 mm in diameter by an aperture, A1, in front of the entrance window of the chamber. The focusing optic was an aberration-corrected triplet lens with a focal length of 125 mm. The measured divergence of the laser beam was 60 μrad which gave a focal spot diameter of 8 μm.

The input UV beam energy was monitored by measuring the reflection from the tilted entrance window of the chamber using calorimeter C1. Since the laser beam was not diffraction limited the focal spot size could be calculated by means of a ray trace code assuming a uniform input beam with a Gaussian spread of starting ray angles with a divergence of 60 μrad (FWHM). From these calculations, the peak intensity at the focal point was 1.2×10^{15} W/cm^2 for an input energy of 5 mJ. A second detector, C2, was located inside the chamber to record the energy transmitted through the breakdown plasma. The calorimeter had a collection cone angle of f/3 and thus collected both transmitted and scattered radiation. When the chamber was evacuated the calorimeter C2 was cross calibrated over the full experimental intensity range with the input energy monitor C1. At high intensities two-photon absorption in the entrance window and triplet lens was observed and included in the intensity dependent cross calibration factor. In order to achieve the high measurement accuracy required to determine the absorption in the breakdown plasma the calorimeter C2 was also calibrated and corrected for its slightly different response in vacuum and each gas due to cooling of its surface. Another aperture, A2, could be placed 12.5 cm beyond the focal point in front of C2. The diameter of the aperture was the same as that of the input laser beam in order to let the beam through without being stopped when the chamber was evacuated. By taking measurements with and without the aperture in place, the fraction of laser radiation scattered outside the original beam diameter was measured. The distribution of scattered radiation at the aperture position was also measured by recording images on UV sensitive paper.

To identify any energy backscattered towards the laser system, a sensitive fluorescent plate was placed in a position to observe the reflection of the backscattered pulse from the target chamber entrance window. While reflected radiation from the antireflection coated focussing lens could be observed on this screen no indication of backscattered light from the breakdown plasma was observed. From the known visual sensitivity of the fluorescent plate it was estimated that any backscattering light, if present, was less than 1% of the incident laser energy.

To characterize the plasma channel, a green probe pulse was used to illuminate it from the side to produce shadowgrams. The 6 ps duration green probe pulse was obtained from the dye laser front end of the UV laser system and was, therefore, perfectly synchronized with the UV pulse. By varying the delay time of the probe pulse, one could observe the formation and evolution of the plasma channel. To obtain a high enough intensity to exceed the emission from the breakdown plasma a weak focusing lens of 1m focal length was used to demagnify the 1 cm diameter probe laser beam through the target plasma.

The resultant shadowgrams of the plasma channels were imaged onto a video digitizer system via a 10 x microscope objective. A shadowgraphic image was obtained by imaging a point 200-500 μm past the plasma column onto the vidicon. Thus the pattern of light after it had been deflected by refractive index gradients in the plasma was observed. The resultant video signals were processed by a computer and stored on disk. A narrow band filter with peak transmission at 497 nm, the wavelength of the green probe pulse, was placed in front of the video digitizer to block most of the plasma emission and background scattered light. In addition, in separate experiments, the plasma emission itself and lower resolution shadowgrams were observed using a 50 mm focal length f/16 camera lens imaging onto the same vidicon. The magnifications of both camera lens and microscope objective were calibrated against a standard microscope scale located at the position of the breakdown plasma. The resolution of the imaging system was also tested using a resolution test chart indicating a resolution of ~10 μm for the microscope objective in the shadowgraphic mode.

The target chamber could be evacuated down to 1 x 10 $^{-5}$ Torr. It was evacuated and flushed twice every time when filling the gas of interest. In the present experiment, argon and helium were studied at a pressure of 500 Torr while air was investigated at full atmospheric pressure.

5.3. EXPERIMENTAL RESULTS

5.3.1 Breakdown Thresholds

The breakdown threshold is one of the first parameters of interest in characterizing the formation of plasma in gas targets. There are two possible mechanisms for breakdown to proceed [16,17]: multiphoton ionization (MPI) and cascade ionization by electron collisions. For MPI to occur a high intensity is generally required since the electric fields in the laser beam at focus must be comparable to the atomic fields. However, once the threshold is reached the ionization rate can become very high since it is a very strong function of intensity. The electron density due to MPI will initially grow linearly with time for a constant input laser intensity. At the same time the MPI process for linearly polarized radiation produces little direct heating of the resultant plasma [9]. However, electrons can also gain thermal energy via electron-ion collisions, that is Inverse-Bremmstrahlung (IB) heating. The resultant energetic electrons can impact ionize the gas, leading to cascade breakdown. In this process, lower laser intensities over longer periods of time can form a fully ionized plasma with a relatively high electron temperature. The IB heating and cascade ionization processes require an initial source of electrons which for small focal volumes would probably be generated by MPI.

Thus in collisional plasmas heated by short pulses, it is expected that the threshold intensity will be determined by MPI to produce a starting electron density and the subsequent rate of ionization and heating will depend on a combination of the above processes.

The threshold intensity for breakdown in a collisional plasma is usually defined experimentally as that required in order to observe a faint spark at the focal point by human eye. Our experimentally observed threshold intensities determined by this criteria are given in Table 5-1.

For comparison, theoretical predictions [20] and previous pure MPI results from collisionless gases are also presented in the same table for an ionization rate of $W = 2 \times 10^{9} s^{-1}$. In the present experiment, pressures of 500 Torr for argon and helium were used while for air 700 Torr was used. The earlier collisionless MPI results of Gibson et al [5] were obtained at pressures of less than 10^{-5} Torr. It is seen that the present results show a threshold in agreement with that predicted by MPI [20] but lower than the collisionless MPI results of Gibson et al. The ionization rate chosen, $W = 2 \times 10^{9} s^{-1}$, would produce only a small fractional ionization to initiate the breakdown as will be discussed below.

Table 5-1

Breakdown thresholds for argon, air, and helium. (Intensities in units of Wcm^{-2}, hν = 5.0 eV)

Final species	Present experiment	Keldysh MPI theory [a]	Gibson et al. 500 fs KrF [b]
Ar $^{+1}$ (15.8 eV)	$4 \pm 2 \times 10^{13}$	2.9×10^{13}	1.3×10^{14}
Ar $^{+2}$ (27.6 eV)		2.1×10^{14}	5.3×10^{14}
Ar $^{+3}$ (40.9 eV)		1×10^{15}	1.2×10^{15}
Ar $^{+4}$ (59.8 eV)		3.2×10^{15}	2.0×10^{15}
He $^{+1}$ (24.6 eV)	$4 \pm 1 \times 10^{14}$	1.7×10^{14}	4.0×10^{14}
He $^{+1}$ (54.4 eV)		2.4×10^{15}	3.5×10^{15}
Air	$8 \pm 3 \times 10^{13}$	-	-

[a)] eqn. 1 of ref. 20, calculated at an ionization rate of W = 2x10 ^{9} s^{-1} (note: eqn.17 of ref. 3 for these same rates contains a typographical error)

[b)] Ref. 5, measured at an ionization rate of W = 2x10 ^{9} s $^{-1}$ (note: in ref.5 the intensities given were found by multiplying the "average" intensities by 3.67).

5.3.2. Absorption and Scattering

The energy absorption and scattering were measured by detectors C1 and C2. These results are shown in Fig. 5-2(a) for argon and air and Fig. 5-2(b) for helium.

Without the aperture A2 in place it can be seen that both air and argon absorb up to 13 % of the input laser energy. The fractional absorption peaks at an input energy of 3mJ and then falls off as the energy further increases. With the aperture A2 in place, the measurements gave the sum of radiation lost due to scattering and absorption. The scattering of the laser beam alone can be obtained by the difference of the two curves. It appears that air scatters more light than argon which in turn scatters more than helium.

The larger error bars for the scatter plus absorption measurement result from the larger shot to shot variation in the measured data. This indicates that the scattering process was varying somewhat more from shot to shot than the total integrated absorption. The scattering patterns were also recorded on UV sensitive paper at the position of A2. The vacuum beam profile and typical scattered radiation pattern for argon gas are shown in Fig. 5-3. It was observed that the scattered radiation was not evenly distributed with respect to the unperturbed beam with a detailed pattern which changes from shot to shot. For argon and air the light was deflected by approximately 32 mrad outside of the original cone angle. For helium the scattered light was deflected by approximately 7 mrad. As discussed below, the scattering is expected to be due to the refraction of the laser beam traversing the breakdown plasma.

5.3.3. Axial Behavior

Shadowgrams of the resultant plasma columns were taken by using the picosecond green probe pulse and a microscope objective imaging lens. They were taken at a variety of input laser energies from 1 to 10 mJ and over a variety of times from 0.04 to 4.0 ns. Typical shadowgrams of the argon plasma at various energies and times after breakdown are shown in Fig. 5-4. Each picture only shows part of the plasma column since the field of view is only 330 μm long. In order that a whole picture of plasma channel expansion can be seen, three shadowgrams taken along the length of the plasma column are combined and plotted together to give a composite picture, as shown in Fig. 5-5. Each curve was taken as an average of a number of shots taken at an input energy of 3.3 ± 0.4 mJ at the times of 0.5, 2.0 and 3.9 ns after breakdown. Direct plasma emission profiles were also recorded and the edge of emission volume for the same input laser energy of 3.3 mJ was slightly larger but corresponded approximately with the latest time shadowgram. To see the relation between the resultant plasma position and the original intensity distribution in the focal volume, isointensity contours calculated from the ray trace code are also overlaid on the diagram. The position of the geometric focal point, z = 0 μm, was determined to an accuracy of ± 50 μm from the center of the shadographic and plasma emission images at the limit of very low input intensities.

A shadowgram of a plasma column in helium is shown in Fig. 5-6 for an input energy of 7.3 mJ at a time of 90 ps after breakdown. The width of the plasma column ranges from 15 μm in the middle to 20 μm at each end in this case. The helium plasma appears to expand and dissipate more quickly than the argon or air breakdown plasmas and distinct shadograms of the helium plasma could only be obtained over the time interval of 0-200 ps.

A shift in the breakdown plasma from the focal point towards the focusing lens is expected at intensities well above threshold. With the f/16 50 mm focal length imaging lens, it was possible to record the shadowgrams of the entire plasma columns at a time of 0.7 ns on a single shot basis. The resulting positions of the front, middle (thickest region) and back of the argon plasma column are shown in Fig. 5-7. Again, time integrated direct images of plasma emission corresponded approximately with the shadowgram positions. From the figure, it is clear that plasma column length initially increases rapidly with input intensity, reaching a length of ~ 830 μm at 3 mJ input and increases more slowly thereafter. More importantly, the whole channel moves forward towards the incident laser beam, with the front edge being shifted dramatically. Assuming a constant breakdown threshold intensity, in the geometric optic limit the leading edge of the plasma is expected to shift forward proportional to the square root of the energy. A least square fit of such a curve to the leading edge of the plasma is shown in Fig. 5-7 (open circles). The threshold intensity corresponding to this curve is 2.0×10^{13} W cm^{-2}.

Both the scattering of radiation and shift in plasma position are related to the refraction of the incident laser beam in the electron density profile of the plasma as shown in Fig. 5-8. The higher electron density, n_e, in the plasma column initially leads to a reduced refractive index, n_r , on axis which will deflect the incident light rays outwards. Thus, at the geometric focal point the rays will already be diverging and intensity reduced from its vacuum value.

5.3.4. Radial Expansion

Upon the absorption of laser energy, the plasma channel heats rapidly and then expands outwards, resulting in a cylindrical shock wave. The shadowgrams measured at 0.5 ns, 2.0 ns and 3.9 ns delay time relative to the creation of the plasma give the rate of radial expansion. Two axial positions were measured with the first position at the geometric focal point and the second position at the point 300 μm towards the lens from the geometric focal point. The second position corresponded approximately to the thickest part of the plasma. The measured radius versus delay time for the two positions are shown in Fig. 5-9. The radial hydrodynamics will be discussed in next section.

5.4. DISCUSSION

5.4.1. Breakdown, Ionization and Heating

The breakdown of the gas begins with the generation of initial seed electrons. For very small focal volumes as in the present experiment the probability of initial free electrons in the gas is negligible and thus the initial electrons must be created by MPI.

The Keldysh parameter [20] $\gamma = \left(\chi_i / 2\phi_{PM}\right)^{1/2}$, where χ_i is the ionization energy and ϕ_{PM} is the ponderomotive potential, is usually used to distinguish the region of pure multiphoton ionization, $\gamma >> 1$, and tunnel ionization, $\gamma << 1$. The ponderomotive potential is defined as $\phi_{PM} = \left(e^2E^2 / 4m_e\omega^2\right)$) where E is the peak electric field, ω is the radial frequency of the radiation, and e and m are the charge and mass of the electron. For our range of intensities from 3×10^{13} W cm^{-2} to 2×10^{15} W cm^{-2} γ ranges from 6.8 to 0.8 for single ionization of argon. However, for lower intensities around the breakdown threshold γ is significantly greater than 1 which is the range of pure multiphoton ionization.

The experimental thresholds for breakdown were determined by reducing the laser pulse energy until a spark was just barely visible and are listed in Table I. If we define the ionization rate used to define threshold as 2×10^{9} s^{-1} as in reference 5 the values which we have observed for argon and helium are in agreement with the predictions for pure MPI according to the theory of Keldysh [20], given our experimental uncertainty. For our 6ps pulse the ionization rate of 2×10^{9} s^{-1} would give a fractional ionization of 0.012 resulting in an electron density of of 2.0×10^{17} cm^{-3} at the predicted threshold intensities. At intensities of 3 times above these threshold intensities the calculated ionization rates [20] for MPI at focus should approach 100% for both argon and helium.

A second measurement of the threshold intensity is found by taking the intensity at the leading edge of the breakdown plasma region towards the lens. From the shadowgram taken at 0.5 ns in Fig. 5-5 and from Fig. 5-7 we see that the leading edge of the argon plasma occurs at a point where the intensity is approximately 2×10^{13} W cm^{-2} which is lower than the value of 4×10^{13} W cm^{-2} observed at the focal point. The lower intensities observed from the leading edge of the plasma column may be due in part to additional ionization of the gas by VUV emission from the main breakdown region which would assist MPI in creating seed electrons for breakdown.

Our measured threshold intensities are a factor of two to three times lower than those measured with 500fs KrF laser pulses in low density collisionless gases by Gibson et al [5]. In their results the peak intensity was calculated by scaling the average intensity by a factor of 3.67. However, there was no discussion of how the average intensity was measured. In the present results the intensities given are the peak values in space and time. These are calculated assuming a gaussian pulse shape in time, using the measured beam divergence together with a ray trace calculation of the beam propagation through the lens system. The comparison of our data with that of Gibson might indicate a pressure dependence of the breakdown threshold. However, at threshold intensities, for a 6 ps pulse at a pressure of 500 Torr we do not expect any appreciable amount of collisional ionization as discussed below in detail. Thus, in our experiment the ionization should be dominated by MPI at threshold and the breakdown threshold should be independent of pressure. The difference in our results and those of Gibson et al. may only be a result of the large uncertainty in the measurement of intensity and differing experimental conditions. At higher pressures and for long nanosecond pulses collisional ionization becomes significant, and the breakdown threshold can decrease with pressure as observed in previous studies [21-24].

After the creation of a fractional ionization density by MPI the plasma will start to absorb energy directly from the laser beam via IB absorption and as the electrons are further heated they would have sufficient energy to collisionally ionize other atoms and ions. The IB absorption coefficient is given by

$$\alpha = \frac{7.8 \times 10^{-9}\ Z\, n_{ecm}^{2}\ \ln\Lambda}{\nu^{2}\ T_{eV}^{3/2}} \qquad [\mathrm{cm}^{-1}] \qquad (5.1)$$

where Z is the charge of the ions, n_{ecm} is the electron density in cm^{-3} , ν is the laser frequency in Hz, T_{eV} is the electron temperature in eV and $\ln\Lambda$ is the Coulomb logarithm. The rate of heating of a single electron is thus given by

$$\frac{dE}{dt} = \frac{\alpha I}{n_e} = \frac{3.3 \times 10^{-18}\ Z\, n_{ecm}\ \ln\Lambda\, I_{14}}{T_{eV}^{3/2}} \qquad (\frac{eV}{ps}) \qquad (5.2)$$

where I_{14} is the intensity in units of 10^{14} W/cm^2. Assuming constant values for intensity, electron density, and Coulomb logarithm and an initial temperature of T_0, equation (5.2) can be integrated to give the electron temperature as a function of time, t_{ps} in picoseconds, yielding

$$T_{eV}^{5/2} = 8.3 \times 10^{-18}\ Z\, n_{ecm}\ \ln\Lambda\, I_{14}\ t_{ps} + T_0^{5/2} \qquad eV^{5/2} \qquad (5.3)$$

For our conditions using linearly polarized light the electrons created by MPI will have a temperature of approximately 1/10 of the ionization potential [9] and thus, we can take an initial electron temperature of $T_0 = 2\text{eV}$. Therefore, for an initial electron density of 2.0 x 10^{17} cm^{-3}, assuming $\ln \Lambda = 3$ we would predict a final temperature at an intensity of 5x10^{13} Wcm^{-2} given by eqn. (3) of 3.4 eV. Thus, close to the threshold intensity conditions for our 6ps laser pulse little IB heating is expected. However, well above threshold at an intensity of 2x10^{14} Wcm^{-2} and a fully ionized density of 1.65x10^{19} cm^{-3} we would expect a final temperature of 30 eV and thus very substantial IB heating is expected.

Once IB heating becomes significant it is possible for the collisional ionization rate to exceed the MPI ionization rate. Using the collisional-radiative model, the collisional ionization coefficient is on the order of [27]

$$S = \frac{9 \times 10^{-6}\ \varsigma\ T_{eV}^{1/2}\ \exp(-\chi_{eV} / T_{eV})}{\left(4.88 + T_{eV} / \chi_{eV}\right) \chi_{eV}^{2}} \qquad \text{cm}^3\ \text{s}^{-1} \qquad (5.4)$$

where ς is the number of electrons in the outer shell and χ_{eV} is the ionization potential. The resultant time required to achieve the next ionization level is

$$\tau_{\text{ioniz}} = 1 / S\, n_{\text{ecm}} \qquad \text{s} \qquad (5.5)$$

For single ionization of argon for which χ_{eV} = 15.8 eV and ς = 8, we obtain S=1.0x10^{-9} cm^{3} s^{-1} at a temperature of 3.4eV. This leads to an ionization time of t = 5 ns at a density of 2 x 10^{17}. Thus, very slow ionization is expected at the breakdown threshold plasma conditions and the ionization should be dominated by MPI at threshold. If one considers an intensity well above threshold for argon of 2×10^{14} W/cm $^{-2}$ then full ionization of the plasma to the singly ionized state from MPI is expected [20] ($W = 3\text{x}10^{12}$ s^{-1} for single ionization of argon and $W = 2\text{x}10^{9}$ s^{-1} for double ionization of argon) . Using equation (3) to calculate the final plasma temperature gives $T_{eV} = 30$ eV. At a temperature of 30 eV (15 eV) the time required to collisionally ionize the singly ionized plasma to doubly ionized plasma from equation (5) is 2.0 ps (6.5 ps), from doubly ionized to triply ionized state is 3.7 ps (19 ps) and from triply to quadruply ionized is 12 ps (114 ps). Thus well above breakdown threshold it is expected that MPI will rapidly form a singly ionized plasma which subsequently will be heated by IB absorption and further ionized by collisional ionization. This process will be slowed down by the fact that the energy taken from the electrons for each ionization step is greater than the thermal energy per electron and thus the plasma will cool significantly and the ionization rate will drop in a self regulating fashion as ionization proceeds. Thus for a plasma of electron temperature around 20-30eV an ionization state between triply and quadruply ionized would be expected within the 6ps pulse duration.

The plasma temperature can be estimated by equating the measured fractional absorption to the IB absorption for a fully ionized plasma with a length of 800 μm as measured from the shadowgraphy. The peak measured absorption for argon was 13% which would require electron temperatures of 2 eV, 8 eV, 18 eV and 32 eV for singly, doubly, triply or quadruply ionized argon plasma. These temperatures are lower than those estimated from simple IB heating rates given earlier but would be consistent with the fact that the ionization process itself will absorb energy from the heating plasma.

The electron temperature can also be estimated from the absorbed energy density. Considering the case of the plasma created by a 3.3mJ laser pulse as shown in Fig.5-5 , the total ionized volume is 5 x 10 $^{-7}$ cm^{-3} which if quadruply ionized with an internal energy equal to 13% of the incident energy, given by the measured absorption, would result in a plasma temperature of 45 eV. If one takes into account radiation of energy from collisional excitation of Ar $^{+4}$ a lower temperature would be expected. For example, if half of the internal energy of ionization (144 eV per ion) is radiated away in 6ps then the temperature would be 27 eV.

Thus from the absorbed energy balance, IB absorption length and ionization time scales the argon plasma appears to ionized to close to Ar $^{4+}$ with a temperature of ~30eV. This is a higher ionization state than could be achieved from MPI directly for I=1x10 ^{15} Wcm^{-2}. It is interesting to note that a similar ionization state of ~3 and an absorption of less than 20% has been reported for 760 Torr argon plasmas heated by 10ns, 40mJ pulses at a wavelength of 0.694 μm . Thus the self-regulating nature of IB heating and cascade ionization appears to extend over a wide pulselength and wavelength regime.

5.4.2. Refraction

Once a plasma has been formed the incident laser light will be deflected by the refractive index gradients set up by the electron density. As shown in Fig. 5-8, there is an initial electron density with a maximum on axis giving rise to an electron density gradient towards the middle of the column. This will lead to a reduction of the index of refraction on axis which will act like a defocussing lens and deflect the incoming optical rays outwards from their original path. If the path of the ray is known then the integrated deflection angle, θ, can be calculated by the relation

$$\theta = \frac{d}{dy}\int n_r \, dz \qquad (5.6)$$

where n_r is the refractive index. The refractive index gradient can be estimated from the peak electron density, n_{e0}, and the radius of the initial plasma column, R, giving $dn/dy \approx n_{e0}/(2Rn_c)$, where $n_c = \omega^2 m_e / 4\pi e^2$, is the critical density.

In helium the plasma lengths observed from optical emission ranged from 400 to 600 μm for energies of 6 to 8mJ. A few early time shadowgrams in this energy range agree with these lengths indicating a plasma longer than the 330 μm field of view, as shown in Fig. 5-6. Thus, for helium, using L=400-600 μm, R=8 μm and n = 1.65x10 ^{19} cm $^{-3}$ a deflection angle of 23-34 mrad would be expected. The observed deflection angle of 7 mrad is smaller than the above value. However, this would be reasonable because most of the rays do not travel through the maximum density gradient region for the full length of the plasma.

In the case of argon, L = 850 μm and R = 16 μm as seen from Fig. 5-5. If the plasma is singly ionized then n_{e0} = 1.65×10^{19} cm^{-3} and a maximum deflection of 24 mrad would be expected. This is less than the measured maximum deflection of 32 mrad for argon. As observed for helium most of the rays would generally not pass through the maximum density gradient region for the full length of the plasma and the observed deflection angle should be considerably smaller than the value calculated above. This expectation is in good agreement with the higher ionization stage deduced from absorption as discussed above. Long pulse measurements of scattered light from an argon plasma have previously indicated self focussing of radiation in argon [28]. However, our pulse is so short that only the electronic process should contribute (as opposed to slower electrostrictive and thermal contributions) which for our conditions is estimated to give only a small self focussing effect. In addition, the scattering angle observed here is much smaller than reported in reference 28 and is entirely consistent with the expected electron density gradients for multiply ionized argon.

Because refraction would deflect the incoming light rays from their original path the peak intensity achieved at high input energies will be considerably less than the peak focal spot intensities in vacuum. Thus the peak ionization states which could be achieved directly by multiphoton ionization would also be limited by refraction to lower ionization states depending on the density of the target atoms. A more quantitative theoretical analysis of the breakdown and refraction problem would require numerical simulations of the interaction processes.

5.4.3. Blast Wave

After the ionization and heating of the plasma column the heated plasma region will expand radially. The initial energy deposition is virtually instantaneous on the much slower nanosecond time scale of the gas expansion. If the energy were deposited along the z-axis in a region of zero radial dimension then the situation would correspond to that of a cylindrical blast wave in a gas which has a self similar solution described in reference 29. This solution gives the expected profiles of density, pressure and temperature. A cylindrical density column is formed with high density walls and a low density high temperature region on axis. Such a description would be consistent with the shadowgrams observed in the time interval of 2-4ns for which the center of the plasma column is transparent, as can be seen in Fig. 4 (b-c). If uniformly ionized, this hollow density profile would form a refractive guiding channel for subpicosecond high intensity pulses injected on axis. The radial size of the cylindrical shock wave given by the self similar solution is [29]

$$R = A(E_L / \rho_0)^{1/4}\, t^{1/2} \qquad (5.7)$$

where A is a constant approximately equal to unity, E_L is the energy deposited per unit length, ρ_0 is the mass density, and t is the time since the release of the energy on axis.

In our present case the energy is released over a radial volume and thus it takes some time for the density and pressure profiles to evolve towards the ideal blast wave result. As can be seen from Fig. 5-9 at an input energy of 3.3mJ during the period of time from 2.0 to 3.9 ns after the laser pulse it appears that the plasma column expands approximately proportional to $t^{1/2}$ as expected for an ideal blast wave. Given the measured radius of $R = 41.5$ μm at 3.9 ns the energy deposited per unit length into the expanding shock wave wave is ~205 μJ /mm. At the same time the average absorbed energy is ~505 μJ /mm assuming an absorption length of 850 μm. However, integrating the blast wave energy over the full plasma profile from the 3.9 ns shadogram in Fig. 5 gives a total energy of 84 μJ compared to an absorbed energy of 430 μJ. Thus, only 20-40% of the absorbed energy has shown up in the hydrodynamic motion of the heated gas. This difference is not unreasonable given that a large fraction of the absorbed energy is lost as line radiation from the recombining ions and part of the energy will still be locked up in ionized and excited metastable states of the argon atom. Since the present plasma has low temperature, the supersonic heat wave model for hot plasma produced by the nanosecond CO_2 laser [30] does not apply here.

5.5 Conclusions

The present experiments have shown that by using axial focussing with f/10 optics it is possible to form plasma columns with a radius of ~25 μm and length of 900 μm in argon and a radius of ~10 μm and length of 400 μm in helium. The breakdown thresholds observed are in agreement with those expected for multiphoton ionization while the energy absorption indicates Inverse Bremsstrahlung and collisional ionization are important in subsequent heating and ionization of the plasma. Even so, the integrated absorption over a millimeter length plasma in argon or air is on the order of 10% indicating ionization and heating of several millimeters of plasma at the given pump intensities should be possible. The limiting factor in the present experiment appears to be refraction of the pump radiation in the electron density gradient formed by the breakdown process itself.

The radial expansion observed in the time period of 2 to 4 ns after breakdown is consistent with a cylindrical blast wave in the gas with approximately 30% of the absorbed energy in the hydrodynamic motion of the gas. The resulting hollow density profile when fully ionized would have a maximum refractive index on axis which may be suitable for use as a light guide for propagating high intensity subpicosecond pulses over long plasma lengths.

REFERENCES

1. K.G.H. Baldwin and B.W. Boreham, J. Appl. Phys. 52 (1981) 2627.
2. A. l'Huillier, L.A. Lompre, G. Mainfray and C. Manus, Phys.Rev. A 27 (1983) 2503.
3. M.D. Perry, O.L. Landen, A. Szoke and E.M. Campbell, Phys.Rev. A 37 (1988) 747.
4. S.L. Chin, C. Rolland, P.B. Corkum and P. Kelly, Phys. Rev. Lett. 61, (1988) 153.
5. G. Gibson, T.S. Luk, and C.K. Rhodes, Phys. Rev. A 41 (1990) 5049.
6. S. Augst, D.D. Meyerhofer, D. Strickland and S.L. Chin, J. Opt. Soc. Am. B 8(1991) 858.
7. J. Peyraud and N. Peyraud, J. Appl. Phys. 43 (1972) 2993.
8. W.W. Jones and A.W. Ali, Appl. Phys. Lett. 26 (1975) 450.
9. N.H. Burnett and P.B. Corkum, J. Opt. Soc. Am. B 6 (1989) 1195.
10. N.H. Burnett and G.D. Enright, IEEE J. Quant. Electron. 26 (1991) 1797.

11. A. Tunnermann, R. Henking and B. Wellegehausen, Appl. Phys. Lett. 58 (1991) 1004.
12. G.Z. Sun, E. Ott, Y.C. Lee, and P. Guzdar, Phys. Fluids 30 (1987) 526.
13. D.C. Barnes and T. Kurki-Suonio, and T. Tajima, IEEE Trans. Plasma. Phys. PS-15 (1987) 154.
14. R. Rankin, C.E. Capjack, N.H. Burnett and P.B. Corkum, Optics Lett. 16 (1991) 835.
15. J.C. Solem, T.S. Luk, K. Boyer, and C.K. Rhodes, IEEE J. Quant. Electron. 25 (1989) 2423.
16. C.G. Morgan, Rep. Prog. Phys. 38 (1975) 621.
17. G.M. Weyl, in "Laser-Induced Plasmas and Applications" (L.J. Radziemski and D.A. Cremers, eds.) Marcel Dekker, New York, 1989, pp.1-67.
18. J.N. Broughton and R. Fedosejevs (accepted, J. Appl. Phys.).
19. S.Szatmari and F.P. Schafer, J. Opt. Soc. Am.B. 6 (1989) 1877.
20. L.V. Keldysh, Zh. Eksp. Theor. Fiz. 47 (1964) 1945 Sov. Phys. JETP 20, (1965) 1307
21. R. Dewhurst, J. Phys.D. Appl. Phys. 10 (1977) 283.
22. R. Dewhurst, J. Phys.D. Appl. Phys. 11 (1978) 191.
23. M.C. Gower, Opt. Comm. 36 (1981) 43.
24. A.J. Alcock, K.Kato and M.C. Richardson, Opt. Comm. 6 (1972) 342.
25. J. Dawson and C. Oberman, Phys. Fluids 5 (1962) 517.
26. T.D. Johnston and J.M. Dawson, Phys. Fluids 16 (1973) 722.
27. C.D. Colombant and G.F. Tonon, J. Appl. Phys. 44 (1973) 3524.
28. A.J. Alcock, in "Laser Interactions and Related Plasma Phenomena" (H.J. Schwarz and H. Hora, eds.), Plenum, New York, 1972, pp.155-175.
29. S.C. Lin, J. Appl. Phys. 25 (1954) 54.
30. R. Popil, J. Meyer, and B. Ahlborn, Phys. Fluids. 27 (1984) 2767.

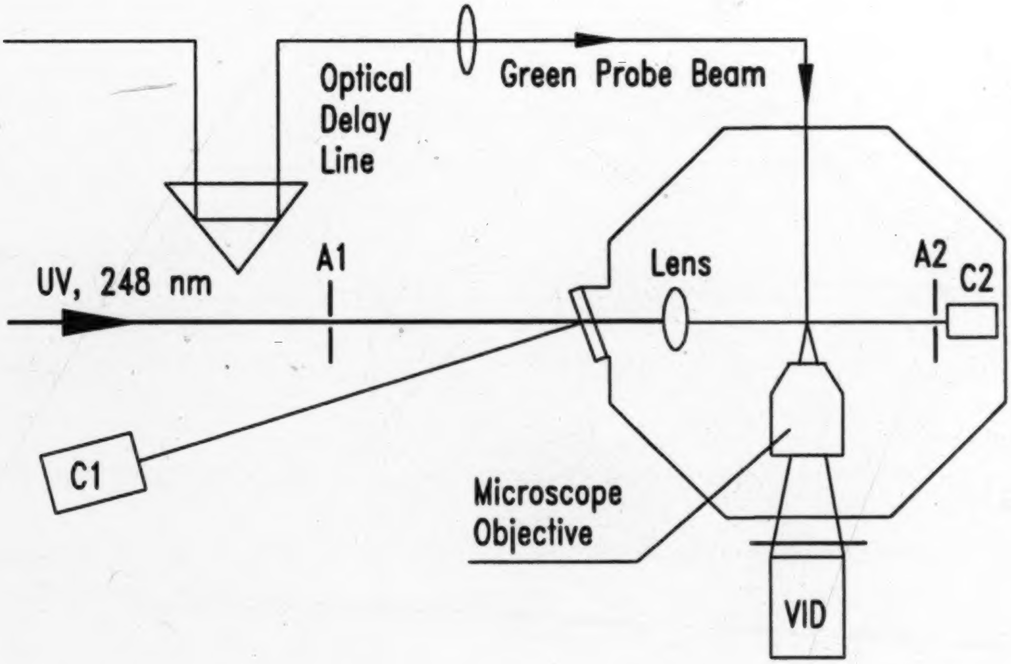
Optical
Delay
Line
Green Probe Beam
UV, 248 nm
A1
Lens
A2
C2
C1
Microscope
Objective
VID

Fig. 5-1 Schematic diagram of experimental layout

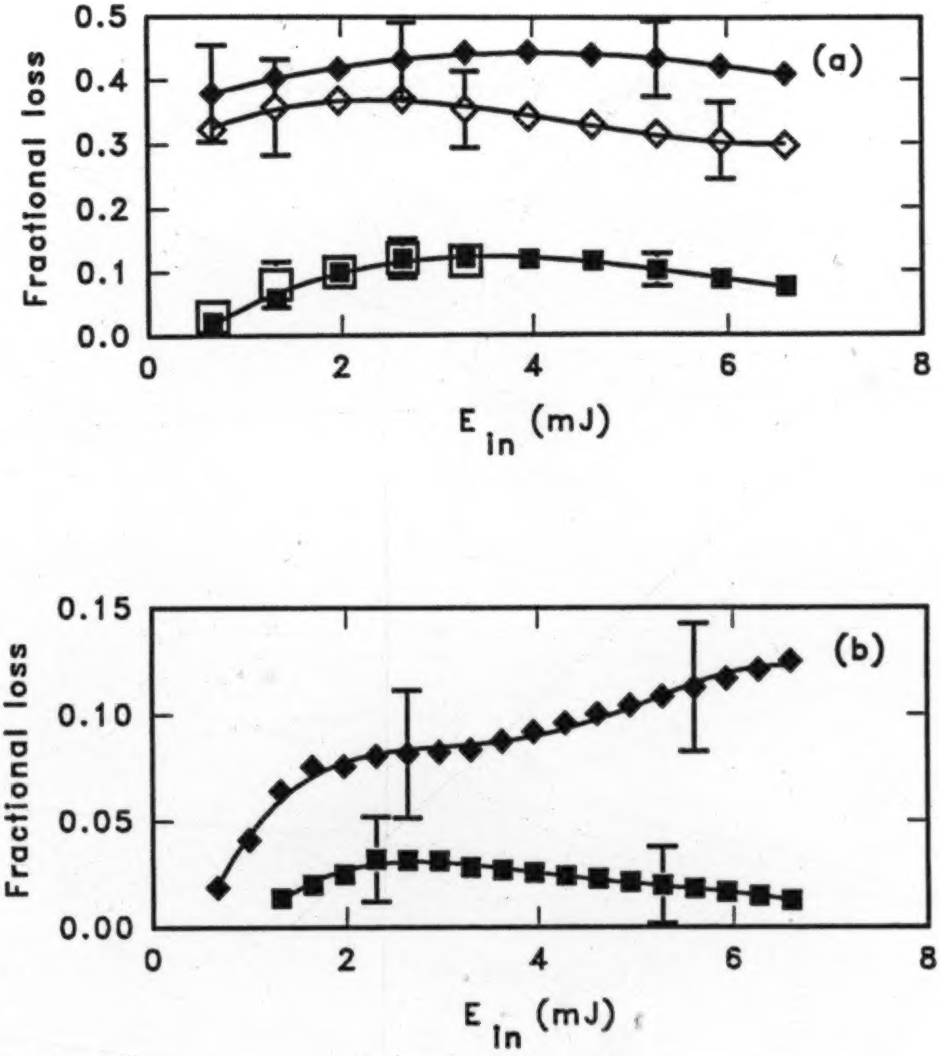

Fig. 5–2 Fractional energy loss of the laser beam in the plasma columns: (a) absorption in argon (□) and air (■) and combined absorption and scattering in argon (◇) and air (◆); (b) absorption in helium (■) and combined absorption and scattering in helium (◆).

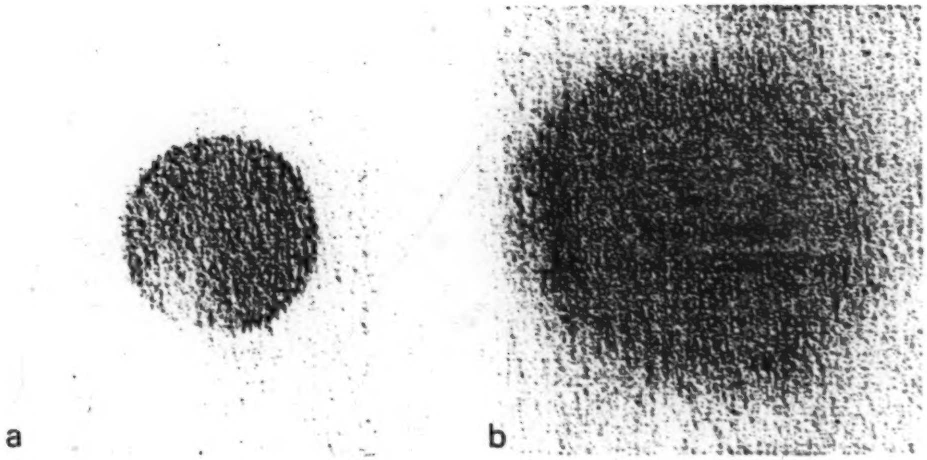

Fig. 5-3 Beam profile in vacuum (a) and scattered radiation in argon (b) recorded on UV sensitive paper at the position of calorimeter C2 for 5 shots at an average energy of E_{in}=5.0 mJ.

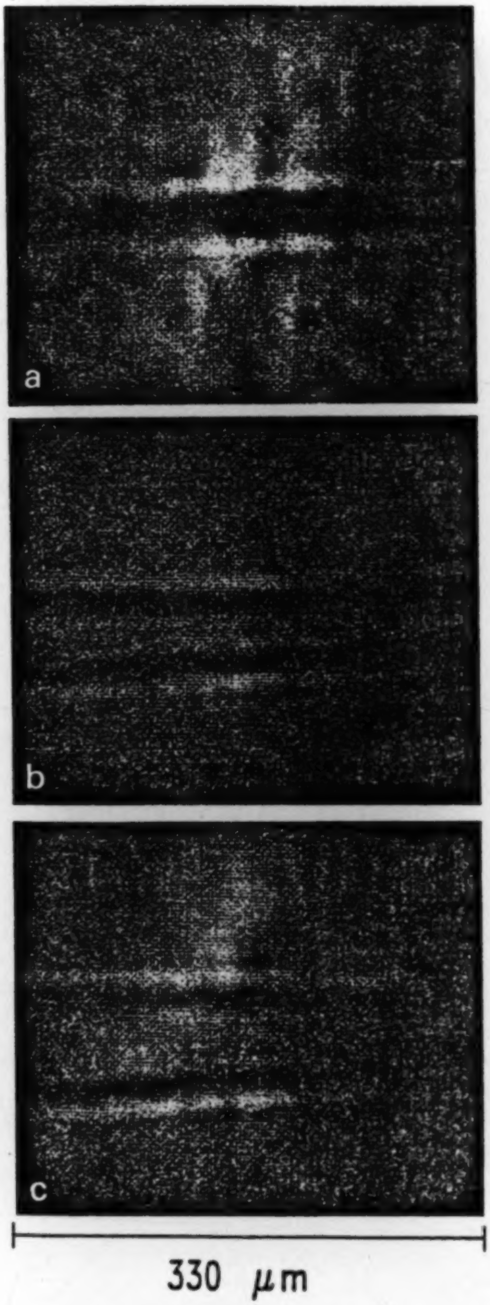

Fig. 5-4 Shadowgrams of the plasma columns: (a) energy E_{in}=1.2 mJ and probe time t_p=0.5 ns, (b) E_{in}=3.4 mJ and t_p=2 ns,and (c) E_{in}=4.5 mJ t_p=3.9 ns. The geometrical focal point is at the right hand edge of the image.

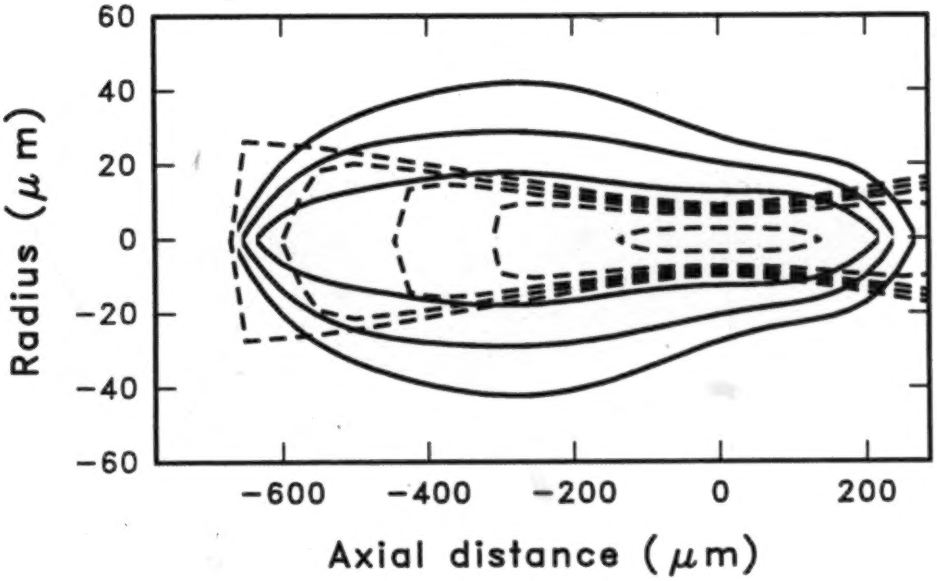

Fig. 5-5 Outlines of the argon plasma at times of 0.5 ns, 2 ns and 3.9 ns (solid lines from inside to outside respectively) for an input energy of 3.3 mJ. Also shown are isointensity contours at levels of 2%, 3%, 5%, 10%, and 50% of peak intensity (dashed lines from outside to inside).

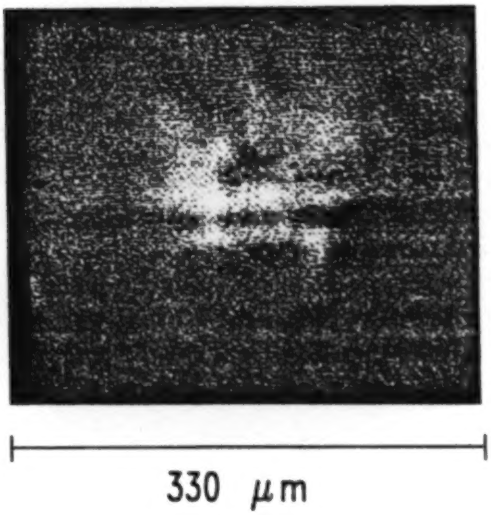

Fig. 5-6 Shadowgram of the breakdown plasma in helium for an input energy of 7.3 mJ at a probe time of 90 ps. The geometric focal point is 100 μm in from the right hand edge of the image.

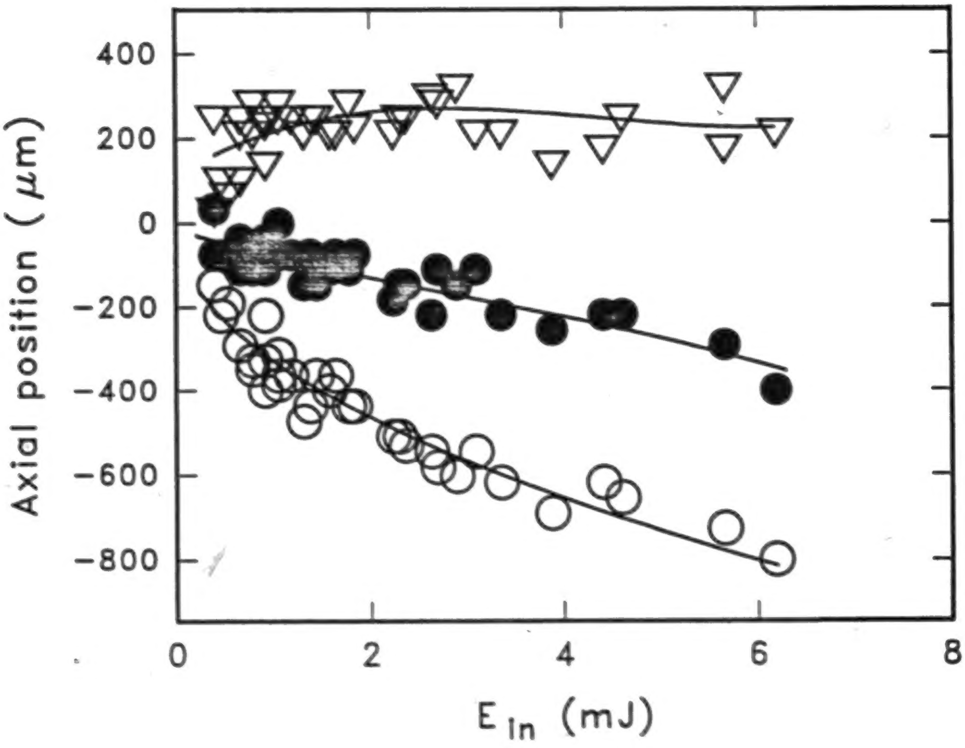

Fig. 5−7 Motion of the plasma column as a function of input energy determined from shadowgrams taken at 0.7 ns. Marked are the front edge (○)(closest to the focussing lens), middle point (●)(thickest part of the plasma), and back edge (▽). The solid line through the open circles is a least−squares fit to the data proportional to $E_{in}^{1/2}$ corresponding to a constant breakdown threshold intensity. The other solid lines are visual fits to the data.

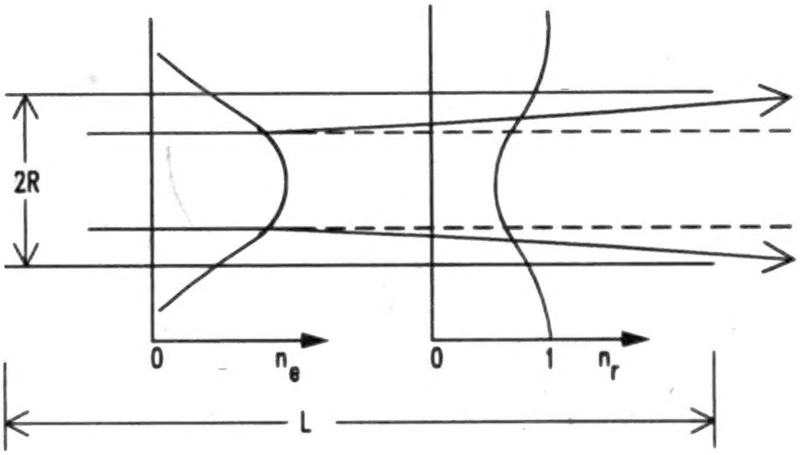

Fig. 5-8 Schematic diagram of refraction from a plasma column of length L. The electron denisty, n_e , and refractive index, n_r , profiles are also shown across the plasma column.

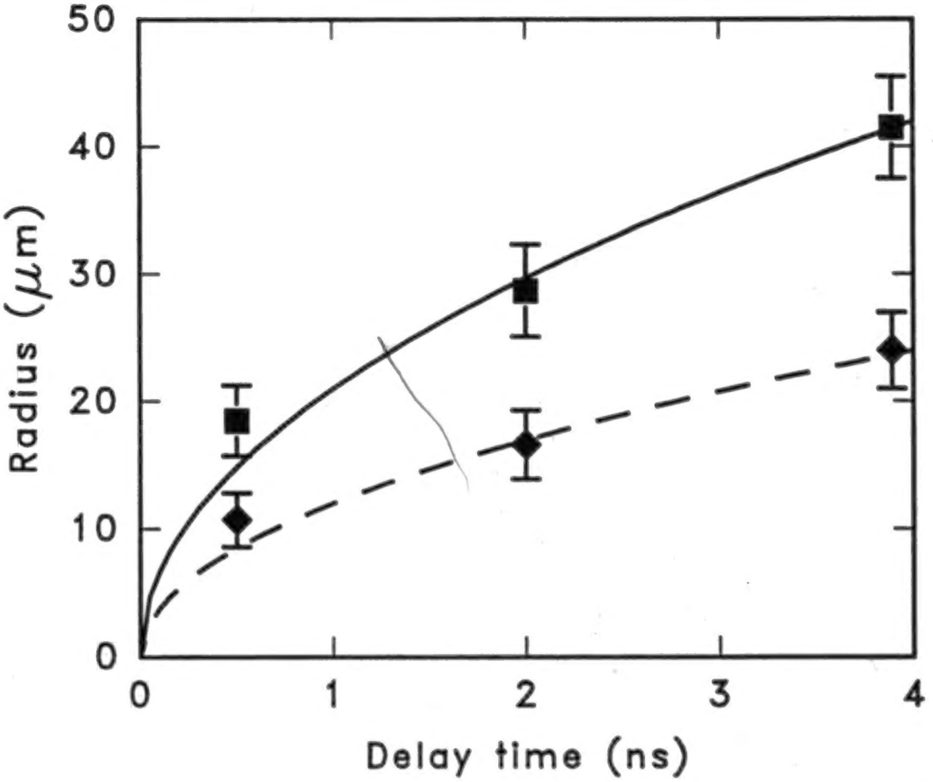

Fig. 5–9 Radius of the evolving argon plasma for an incident laser energy of 3.3 mJ at times of 0.5, 2.0, and 3.9 ns at two axial positions: at the geometric focal position (◆) and 300 μ m towards the laser from the geometric focal point (■).

Chapter 6

Density Measurements of a High Density Pulsed Gas Jet for Laser Plasma Interaction Studies [*]

The study of multiphoton ionization and X-ray lasers has generated new interest in using pulsed gas jet targets at high pressures, at and above one atmosphere, in laser plasma interaction experiments. The great advantage of a gas jet target, once ionized by the laser pulse, is to provide a uniform plasma medium at densities in the range of 10^{19}-10^{20} cm^{-3}. At the same time the limited spatial extent of the gas jet prevents breakdown of background gas at some distance on front of the high intensity focal region which could lead to beam refraction and self-focusing. These effects limit the ability to achieve very high intensities in a controlled manner in high pressure static gas cells.

Such targets would be ideal for multiphoton ionization pumped recombination XUV and X-ray lasers [1, 2] where ion densities on the order of 10^{19} to 10^{21} cm^{-3} are required. The gas jet target permits the excitation of a large volume of uniform gain medium which will be necessary in order to obtain operational coherent radiation sources. In order to provide adequate gain on the desired transitions, the gas density in the jet must be high enough to facilitate rapid recombination leading to large population inversions. Moreover, long interaction lengths are required in order to measure gain for proposed XUV lasers necessitating a high density gas target of the order of a millimeter or more in size. In these cases it also is important that the interaction region be above the gas nozzle with the incident laser beam passing transversely across the gas jet, such that the emission from the ends and sides of the interaction region can be viewed by diagnostics. Furthermore, the gas jet target provides good background conditions for the XUV and X-ray diagnostics which require a vacuum outside of the target region to prevent absorption of the emitted radiation prior to reaching the diagnostic instrumentation. Such absorption would occur if a static fill of gas was used for the target instead.

---

[*] Published as Y. M. Li and R. Fedosejevs, Meas. Sci. Technol. 5, 1197(1994).

Not only is it important to achieve a high starting density for XUV laser studies, it is also necessary to know the spatial density profile in the region of interaction. There is no simple analytic theory which can predict the detailed three dimensional free expansion flow from a high pressure nozzle into vacuum. Thus, it is important to have experimental measurements of the detailed density profile for such gas jets. In the future it may be possible to compare these measurements with numerical calculations of the gas flow in such systems.

Previous work on gas jet sources has focused primarily on supersonic jets for molecular beam and cluster research where the high pressure gas expands and cools with a tapered expansion nozzle to form a supersonic low density flow region extending from within the nozzle to far away from the nozzle tip [3-8]. For XUV laser experiments it is important that the high density flow region be outside the nozzle itself so that the laser beam can pass through freely and diagnostics can view the interaction from various directions. This requirement dictates that simple free expansion from a high pressure nozzle be employed for our gas targets. In the past [9], such a nozzle has been employed for inertial confinement fusion research to achieve long scale length plasmas where the laser was fired directly into the nozzle, which again is different than our required geometry. In their work only the axial density profile has been measured whereas in our geometry it is important to know the transverse density profile at various times throughout the duration of the gas pulse. Also, the jet used in these previous studies has a small opening less than 170 μm in diameter. As mentioned previously, we require an interaction length of the order of a millimeter. Thus, in this work a jet with a large nozzle opening of 1 mm in diameter has been developed and characterized.

A single shot interferometric method has been applied to determine the 3-dimensional density profile of the high density gas jet by taking interferograms of the gas jet and deconvolving the interferograms using Abel inversion [10] . The evolution of the density profile was measured by taking interferograms at various times through the gas flow. Data were obtained for N2 and He at different reservoir filling pressures. The experiment shows that such an interferometer can be used as a convenient and permanent on-line diagnostics for gas density characterization in laser plasma interaction studies. The jets developed in this work have been successfully used in laser plasma interaction experiments both at this laboratory and Rutherford Appleton Laboratory [11] .

In order to produce the required high density gas jets a fast high pressure solenoid valve [12] was employed. A brass nozzle tip was machined with an opening of 1 mm in diameter and a throat length of 1.8 mm, to fit the outlet port of the solenoid valve, as shown in Fig. 6-1. The combined valve and nozzle assembly was rigidly mounted inside a target chamber which could be evacuated to 10^{-2} Torr. One of the requirements for a pulsed gas jet is to achieve a fast rise time to a steady state density with the minimum release of gas into the target chamber. As described earlier, the buildup of background gas in the target chamber would disturb the experimental diagnostics. In order to achieve this goal, a pulse drive circuit was developed to deliver a 190 V pulse of ~ 5 ms duration to the solenoid coil of the valve. The actual duration of the gas pulse is somewhat longer due to the mechanical response time of the solenoid and the reservoir volume within the nozzle.

The density profile of the resultant gas jet was measured using a HeNe laser interferometer shown in Fig.6-2a. The collimated laser beam with a diameter of 1 cm is passed by the tip of gas jet nozzle. The tip is located at the edge of the laser beam displaced to one side so that only half of the beam is distorted when the jet is puffed. Then the beam is reflected at the front and back surfaces of a slightly wedged quartz plate. The thickness of the plate and angle of reflection are chosen to shift one reflection by half a beam width relative to the other reflection. Thus, the distorted portion of the reflected beam from the front surface only overlaps the undistorted part of the beam reflected from the back surface. The interference of the two beams gives rise to fringes outlining the gas jet which are imaged onto a vidicon and digitized by a computer. The wedge angle of the plate is chosen such that there are parallel background fringes covering the region of interest when there is no gas present. By adjusting the imaging lens a magnified image of the gas jet is formed on the vidicon giving the fringe shifts localized in the plane of the gas jet. In the experiment the wedged quartz plate and imaging lens were also placed inside the vacuum chamber while the laser and vidicon were located outside the chamber.

A typical interferogram is shown in Fig. 6-2b. The observed fringe shifts are due to the increased optical path length of the rays propagating through the gas jet. The phase shift is proportional to the difference in the refractive index of the gas from unity which in turn is proportional to the gas density and thus the fringe shift on the interferogram is directly related to the density profile of the gas jet. Assuming that the gas flow is cylindrically symmetric around the axis of the gas jet , the interferogram can be deconvolved by Abel inversion [10] to give the spatial variation of refractive index , thus yielding the gas density profiles. A grid of 40 radial points over a radius of 2 millimeters was used in the inversion process giving an effective resolution of 50 μm for the calculated electron density profile.

In order to achieve a short sub-millisecond duration probe pulse, which is required to freeze the motion of the gas flow, a simple high speed shutter was built. The shutter consisted of a fast linear solenoid [13] with an optical beam block attached to its arm. The beam block had a narrow, 0.5 mm, slit in it to act as a light gate. To achieve rapid and clean switching of the transmitted beam the solenoid shutter was located at the focal plane of the beam telescope used to expand the laser beam to 1 cm in diameter. The optical system was aligned so that the light passed through the slit of the solenoid shutter when the solenoid was in the mid range of its motion. By this means a probe pulse of 0.5 ms was obtained which was adequate for the present experiment. It should be noted that in initial experiments the shuttering was achieved by using a standard high speed camcorder with 1/2000 second option. This proved adequate for obtaining interferograms but the timing could not be measured or controlled relative to the firing of the solenoid.

The interferograms were taken with the gas jet puffing into vacuum in a chamber of ~ 226 l in volume. To precisely determine the positions of undisturbed maxima and minima of the background fringes, interferograms were taken every several shots throughout the experimental measurements without the gas jet puffing. These background fringes were digitized and used as the reference fringes in the analysis of the interferograms. In this manner, any distortion or curvature in the probe beam wavefront was automatically taken into account. In addition, the image of the nozzle tip was recorded every shot in the non-overlapped portion of the beam together with the interferogram so that the position of the shifted fringes could be accurately related to the nozzle tip. The exact dimension of the interferogram was calibrated using the image of a ruler scale which was placed just above the nozzle tip. The overall spatial resolution of the imaging system was 14 μm. At the higher pressures for nitrogen gas a dark region was observed in the vicinity of the nozzle tip as can be seen in Fig. 6-2b. In these cases the light passing within 100 to 200 μm of the nozzle was possibly refracted out of the collection angle of the imaging optics, f/7. This restricted measurement of the density profile within 200 μm of the nozzle at the highest pressures of nitrogen gas. At reservoir pressures of less than 800 psia fringes could be observed right up to the tip of the nozzle.

The risetime of the density of the gas jet was measured by varying the delay of the probe light pulse relative to the triggering of the solenoid valve. Fig. 6-3. shows the increase of fringe shifts observed close to the tip of the nozzle (at ~ 0.2 mm outside the nozzle) from the beginning of opening the solenoid valve to about 25 ms later. In this case, nitrogen gas at a reservoir pressure of 814 psia was used with the solenoid pulse being adjusted to a width of 5 ms which was the same value used in the rest of the measurements reported below. Since the fringe shift corresponds directly to the increase of gas density, the plot gives the rise in the gas density as a function of time after triggering the gas jet. Because of the mechanical time required for the solenoid valve to open and close and the time it takes for the gas to empty out of the solenoid housing the rise and fall times of the gas flow are significantly slower. It takes about 15 ms to reach the maximum density and then the flow reaches a steady state density for approximately 10 ms. After 25 ms the density drops back to zero with a time scale of the order of 15 ms.

A typical spatial density profile taken at a time of 10 ms is shown in Fig. 6-4a. for a reservoir pressure of 1514 psia of nitrogen. The Z-axis is the axial direction of the gas jet. The jet has molecular densities of 5.5×10^{20} cm^{-3}, 4.7×10^{20} cm^{-3}, and 2.8×10^{20} at Z=300 μm , 400 μm and 700 μm , respectively. This is typically the density range of interest for laser plasma interaction experiments. Down the jet at Z = 1 mm, the molecular density decreases to 1.7×10^{20} cm^{-3}. Further down the jet, the density decreases dramatically as the jet spreads out. Fig. 6-4b. shows the corresponding contour plot of Fig. 6-4a. It can be seen that the jet is mainly confined within a 1 mm diameter cylindrical column immediately above the nozzle tip. Also shown in Fig. 6-4b as dashed lines are the full width at half peak density of the radial gas density profile as a function of distance above the nozzle. It can be seen that at distances greater than 1 mm the jet spreads out significantly.

The axial pressure profiles of the gas jet as a function of the distance from the nozzle tip for reservoir pressures of 214, 414, 814, and 1514 psia of nitrogen are shown in Fig. 5. Also, an axial profile for helium is shown in the same figure at the highest reservoir pressure of 1514 psia, which is overlapped on the curve of nitrogen at 1514 psia. The error bars were calculated from the inversion procedure [10] for an estimated measurement accuracy of one tenth of a fringe shift. It is interesting to note that these profiles can be fit over the upper 80 % of their pressure ranges to an exponential function of the form

$$P = P_0 e^{-bZ} \tag{1}$$

where P is the pressure of the gas jet, P_0 is the pressure at the nozzle tip (Z=0) which depends on the reservoir pressure, and b is the density profile coefficient characterizing the gas jet. Such an exponential fall off of pressure with axial distance was also noted for a lower pressure gas nozzle [8]. Taking the average of coefficients b for all individual fits gives a value of b which is equal to $0.0014 \pm 0.0002\ \mu m^{-1}$. Using this average value of b, P_0 is adjusted in each case to give a best fit to the data. From these values the average ratio of P_0 to the reservoir pressure, P_{res}, has been determined giving a value for $\alpha = P_0 / P_{res}$ of $\alpha = 0.27 \pm 0.01$ for both nitrogen and helium. The exponential curves are shown as the solid curves on Fig. 5. The values of P_0 used for plotting the best fit curves in Fig. 5. are P_0 = 60, 114, 228 and 434 psia for reservoir pressures of 214, 414, 814 and

1514 psia of nitrogen respectively. For helium at a pressure P_{res} = 1514 psia, the best fit is obtained with a value of P_0 = 434 psia. Although the data for nitrogen was obscured at the position of Z = 100 μm for a reservoir pressure of 1514 psia the similar flows for helium and nitrogen would indicate that similar pressures would be achieved at this position as for the helium case. It can be seen that over the present range of parameters the jet pressure is linearly proportional to the reservoir pressure and that the pressure falls off approximately as an exponential in the vicinity of the nozzle tip.

Fig.6-6. shows the dependence of gas jet pressure on the reservoir pressure at seven different positions from the tip of nozzle ranging from 120 μm to 2020 μm away from the nozzle tip. At a given position, the jet pressure increases approximately linearly with the reservoir pressure. Linear fits using the average coefficients α and b from above are also shown in Fig. 6-6. It should be pointed out that the ratio of the reservoir pressure to the output pressure at 100 μm away from the nozzle tip is 5 which is comparable to the ratio of 6 obtained with a lower pressure solenoid operated gas jet [8]. This is much smaller than the value of 30 or more obtained with low pressure supersonic jets operated by piezoelectric valves [7]. Thus, higher pressures can be obtained with the present free expansion nozzle and fast solenoid valve, as required for a range of laser plasma interaction experiments.

While the jet is being fired residual gas pressure builds up in the target chamber. With a volume of 226 liters in the target chamber, the background chamber gas pressure will rise up to 1-2 Torr by the end of the shot. Typically experiments can be carried out at a time of 10 ms after the leading edge of the solenoid pulse. This is about 1/4 of the duration of the full gas pulse and thus the background pressure would be below 0.5 Torr. If lower background pressures were required, then a scheme employing high speed differential pumping would be required. In initial laser plasma interaction experiments using the jet in the chamber we have observed no problems from the residual gas pressure on the propagation of the laser pulse.

In conclusion, a pulsed gas jet designed to produce output densities well above one atmosphere has been built and tested. Its spatial refractive index profile has been characterized using interferometry and Abel inversion of the resultant fringe shifts has been employed to obtain gas densities. The full transverse and axial density profiles have thus been obtained. The jet produces high pressures with densities up to 6×10^{20} cm^{-3} for nitrogen and helium gases at 200 μm from the nozzle tip. The jet pressure is linearly proportional to the reservoir pressure and the axial pressure falls off approximately as an exponential function away from the nozzle tip. The dense region is mainly confined to a column of 1 mm in diameter near the nozzle. This gas jet target will be useful in ultrashort pulse laser plasma interaction experiments where it will significantly reduce the defocusing of incident laser beam prior to reaching the high density interaction region and should provide high enough density for recombination XUV and X-ray laser experiments. An additional advantage of using the interferometric method for measuring gas density is that it can be easily incorporated on-line as part of the diagnostics for a given laser plasma interaction experiment.

References

1. Burnett N H and Corkum P B 1989 Cold plasma production for recombination extreme ultraviolet lasers by optical field induced ionization *J. Opt. Soc. Am. B* **6**,1195

2. Burnett N H and Enright G D 1990 Population inversion in the recombination of optically-ionized plasma *IEEE J. Quant. Electron.* **26** 1797

3. Auerbach A and McDiarmid R 1980 Modified pulsed valve for supersonic jet applications *Rev. Sci. Instrum.* **51** 1273

4. Otis C E and Johnson P M 1980 A simple pulsed valve for use in supersonic nozzle experiments *Rev. Sci. Instrum.* **51** 1228

5. Hagena O F 1981 Nucleation and growth of clusters in expanding nozzle flows *Surf. Sci.* **106** 101

6. Cross J B and Valentini J 1982 High repetition rate pulsed nozzle beam source *Rev. Sci. Instrum.* **53** 38

7. Andresen P, Faubel M, Haeusler D, Kraft G, Luelf H W, and Skofronick J G 1985 Characteristics of a piezoelectric pulsed nozzle beam *Rev. Sci. Instrum.* **56** 2038

8. Lompre L A, Ferray M, LHuillier A, Li X F, and Mainfray G 1988 Optical determination of the characteristics of a pulsed-gas jet *J. Appl. Phys.* **63** 1791

9. Musinski D L, Pattinson T T, and Steinman D A 1982 Gas jet targets for laser plasma interaction studies *Plasma Physics* **24**, 731

10. Bockasten K 1961 Transformation of observed radiances into radial distribution of the emission of a plasma *J. Opt. Soc. Am.* **51** 943

11. Offenberger A A, Blyth W, Key M H, Wark J, Najmudin Z, and Damgor A E 1993 Thomson scattering measurements in optically ionized gases produced by high intensity KrF laser radiation *Short-Pulse High-Intensity Lasers and Applications II, H. A. Baldis, Editor, Proc. SPIE.* **1860** *90*

12. Skinner Valve Division, Honeywell, Inc., 95 Edgewood, Connecticut 06051. Model no.: X52HLB23002.

13. Guardian Electric Manufacturing Co., Woodstock, Illinois 60098, Model no.: TP6X12.

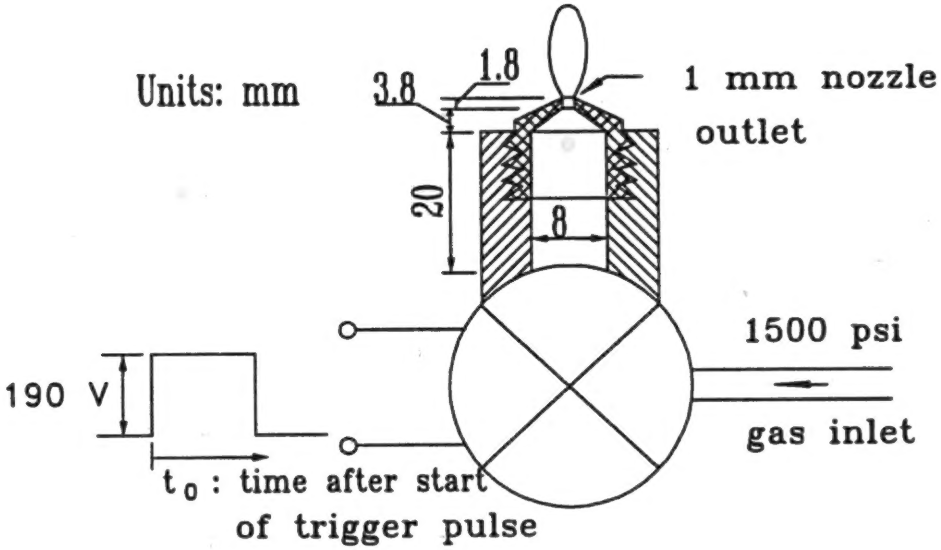
Units: mm
3.8
1.8
1 mm nozzle outlet
20
8
1500 psi
gas inlet
190 V
t_0 : time after start of trigger pulse

Fig. 6-1 Schematic diagram of gas jet solenoid and nozzle tip.

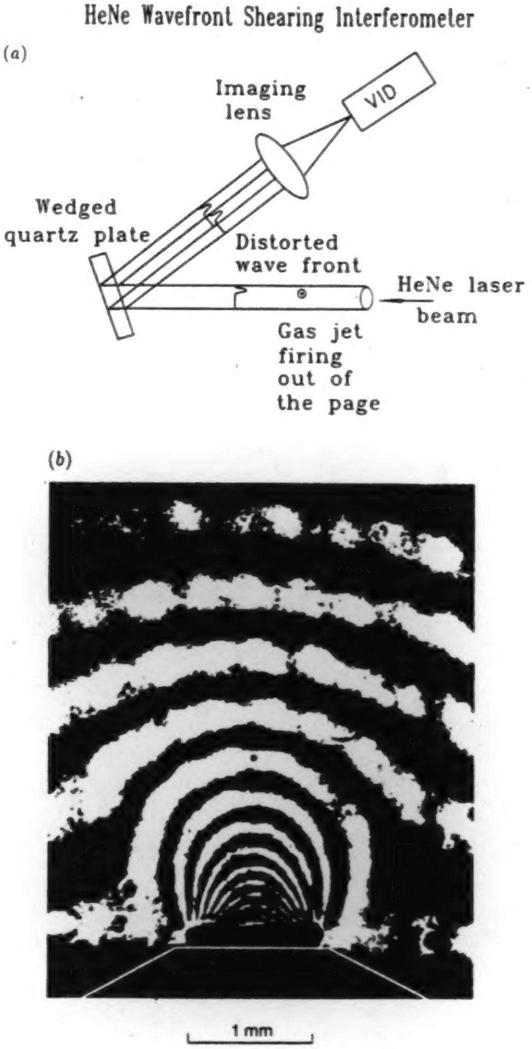
HeNe Wavefront Shearing Interferometer
(a)
Imaging lens
VID
Wedged quartz plate
Distorted wave front
HeNe laser beam
Gas jet firing out of the page
(b)
1 mm

Fig. 6-2 (a) Schematic diagram of the wavefront-shearing interferometer using a wedge quartz plate. The image is viewed by a vidicon camera, VID (b) Typical interferogram obtained at time t_0=10 ms after the start of the solenoid pulse for nitrogen gas at a reservoir pressure of 104 bar.

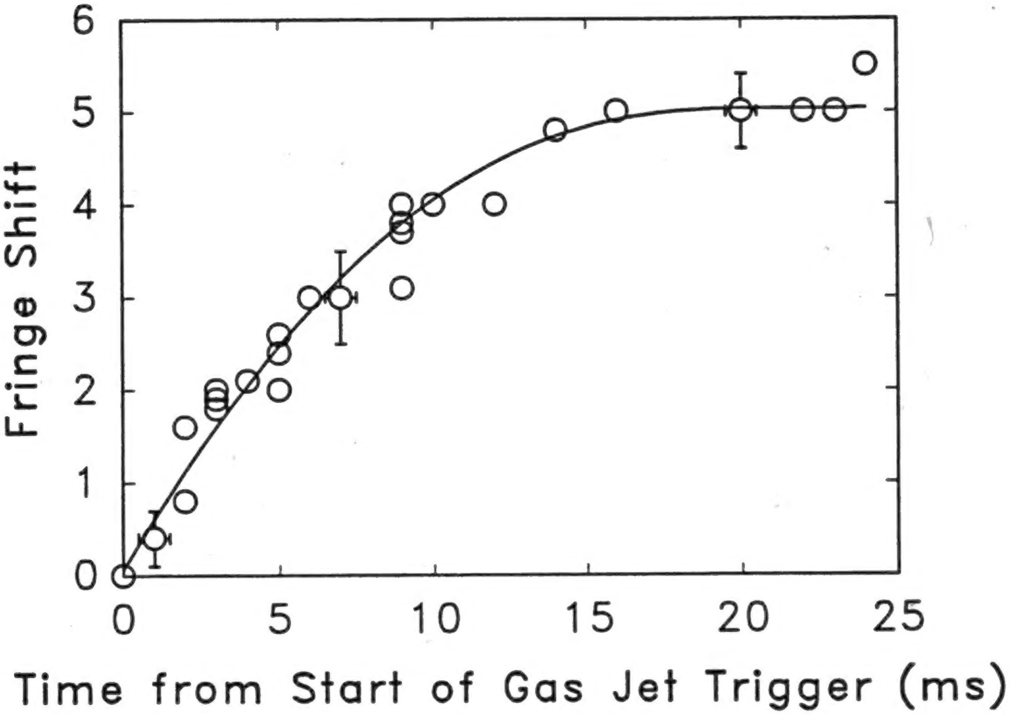

Fig. 6–3 Time–dependence of the fringe shifts observed at a distance of 0.2 mm from the tip of the nozzle for times of 0–25 ms after the start of the solenoid pulse for nitrogen gas at a reservoir pressure of 56 bar.

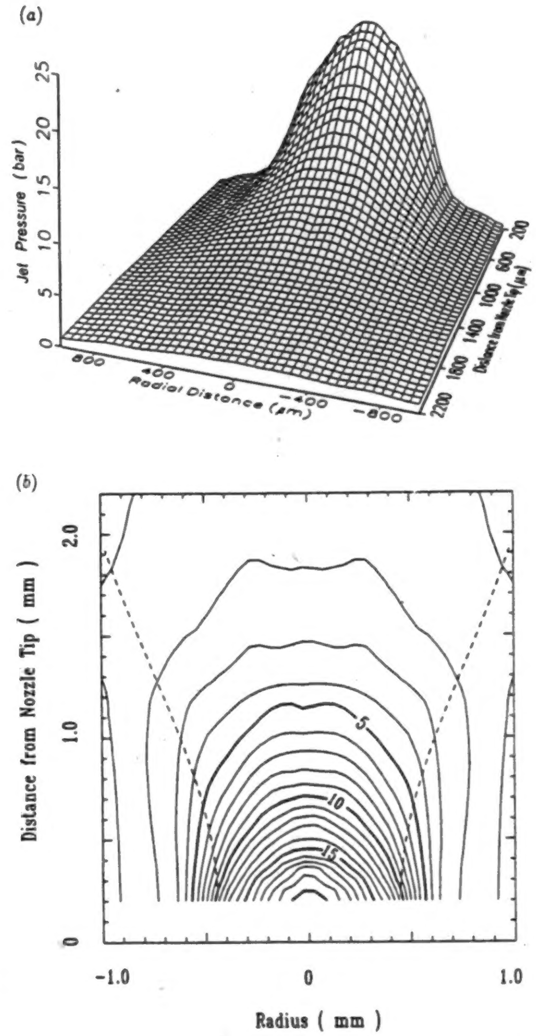

Fig. 6-4 (a) Spatial profiles of gas jet density for nitrogen at reservoir pressure of 104 bar. (b) Corresponding contour plot of density. The contour pressures are given in bars. The broken line outlines the region in which the density falls off to half the peak on-axis value.

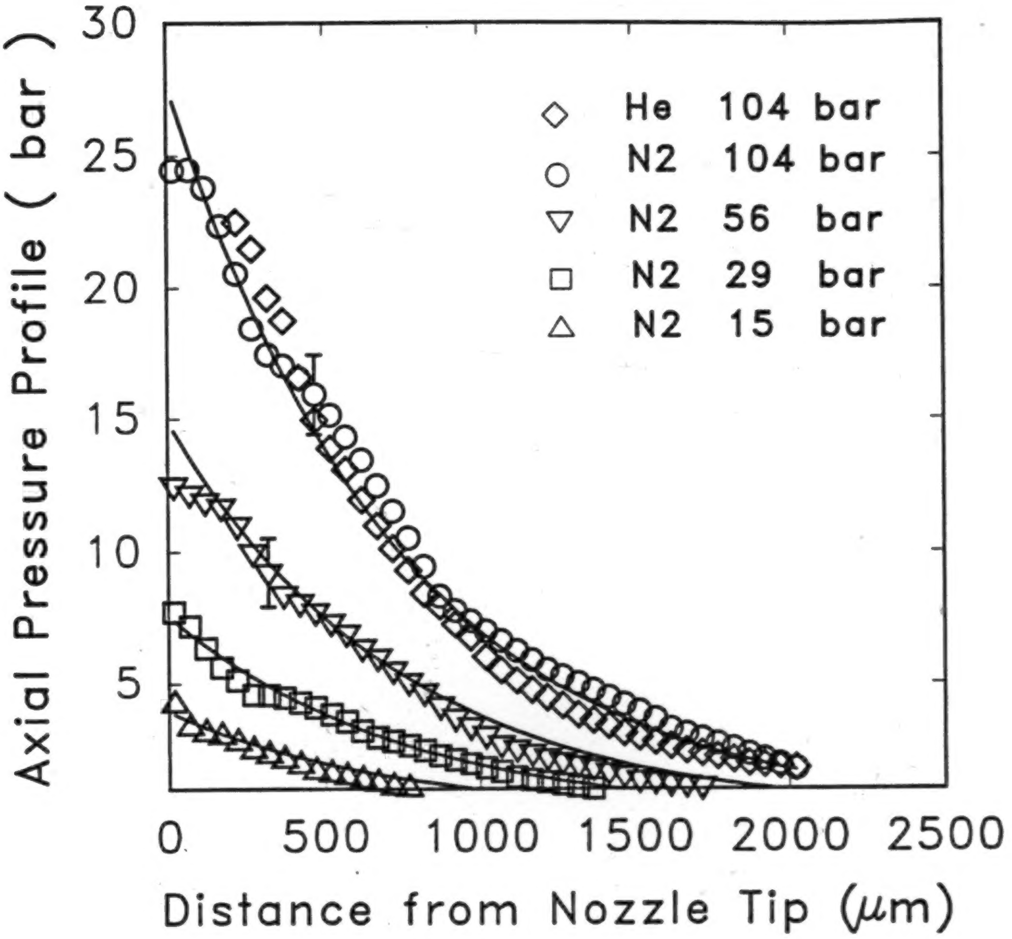

Fig. 6-5 Axial pressures of the nitrogen gas jet as a function of distance from the nozzle tip for reservoir pressures of 15, 29, 56 and 104 bar of nitrogen respectively and for helium gas jet at a reservoir pressure of 104 bar. The full curves are exponential profiles, which have been fitted to the data as discussed in the text.

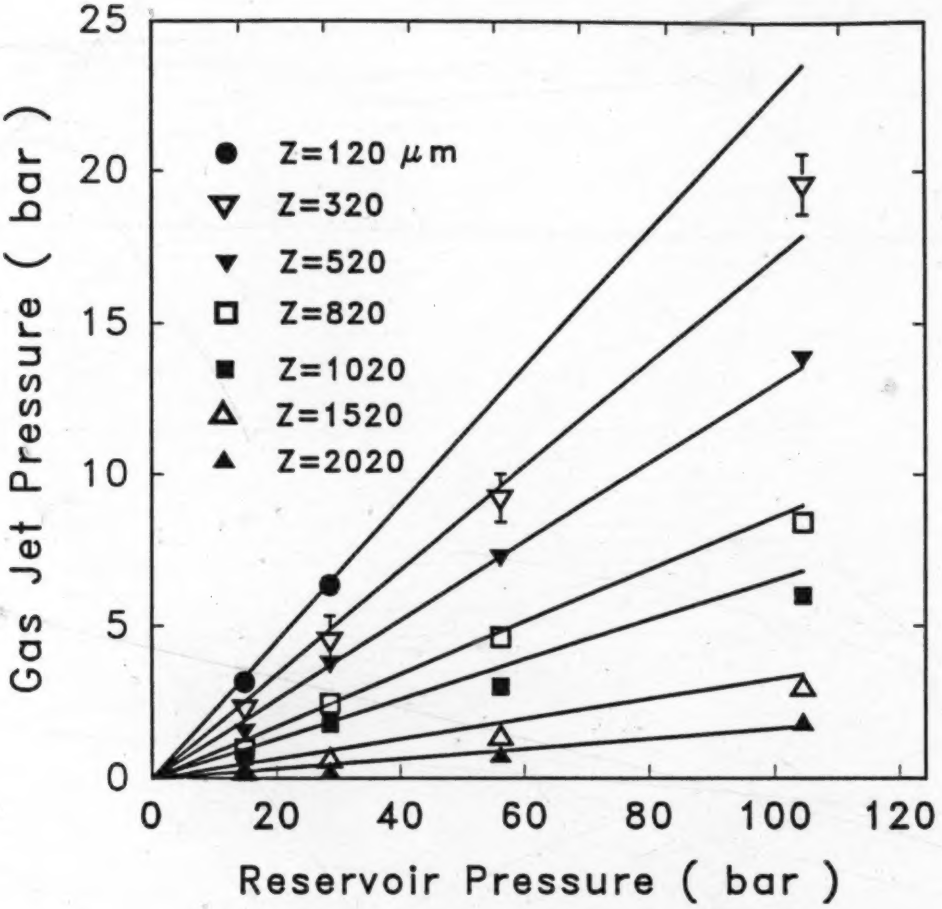

Fig. 6–6 Dependence of gas jet pressure on reservoir pressure at seven different positions from the tip of nozzle. These are 120, 320, 520, 820, 1020, 1520 and 2020 μ m away from the nozzle tip.

Chapter 7

Propagation of Ultrashort Intense Pulse through High Density Gas Jet

7.1 Introduction

In this project, a high density gas jet was developed to minimize the refraction prior to the focus. As such, the laser intensities experienced by the plasma are expected to be much higher than that achieved in the previous experiment using a static gas fill. The propagation of ultrashort intense laser pulses in the plasma was experimentally investigated using several diagnostics. Firstly, the transmitted laser beam was imaged onto a CCD camera. By imaging various axial planes in the jet, the change in size and shape of the transmitted spot reveals the refraction of the beam. Secondly, the beam propagation was also monitored by visible emission and UV scattering in the direction perpendicular to the laser beam. The He II line at 468.5 nm was used to image the fully ionized helium regions while the UV side scattering gives information on the dynamics of beam propagation. With these diagnostics, the effect of the various intensities, pulse widths and gas densities on the beam propagation and plasma channel formation was systematically studied. Thirdly, the beam propagation was also characterized by the spectral shape of He II lines emitted from various sites of the plasma.

7.2 Experimental Details

The gas jet target and various diagnostics are shown in Fig. 7-1. The KrF laser pulse was sent into the target chamber through a tilted CaF_2 window which also acts as a beam splitter, BS1. The reflected beam off of BS1 was further split for monitoring the input pulse energy by a calibrated calorimeter PY7, the level of amplified spontaneous emission (ASE) by a fast photodiode (Hamamatsu R1193U-02). The main laser beam was focused into the gas jet by the focusing lens L1, an aspheric doublet which has a focal length of 20 cm for the wavelength of 248 nm. The laser produced plasma was measured by several diagnostics.

For angular orientation the convention has been chosen that the direction of laser propagation is taken as 0 degrees and the other directions were counted counterclockwise relative to the 0 degrees direction, looking down from above. Due to the complexity of the experiment, several configurations of the various diagnostics have been implemented as described below.

a). In the absence of M6, M7 and L9 :

135 degree visible spectrum on to OMA

90 degree scatted UV light and visible emission

0 degree refraction of the KrF laser beam

b). With M6 in place, and M7 and L9 removed:

90 degree visible spectrum on to OMA

0 degree refraction of the KrF laser beam

c). with L9 and M7 in place and M6 removed:

0 degree visible spectrum on to OMA

90 degree, scattered UV and visible emission

7.3 Laser Beam Profile

The transmitted KrF laser beam was measured by re-imaging it onto a charge coupled device (CCD) camera with the L9 and M7 removed. The magnification used was approximately 14 times. To focus the input beam to the center of the gas jet and obtain a good image of the focal spot, the following calibration procedure was employed. A thin metal wire of 50 μm in diameter was first placed in the axial center of the jet. This was done by using 20 times magnified images from two orthogonal directions. By defocusing, the front end laser beam was used as a light source illuminating the wire. A clear image of the wire could be formed onto the CCD camera by adjusting the lens L3. Then the thin wire was removed and the input beam was refocused until the smallest circular spot was found on the CCD camera. After this adjustment, the focal point was located in the center of the gas jet and at the same time the focal spot was properly imaged onto the CCD camera. The image of the wire was also used as a spatial calibration for the imaging system. As will be discussed later, it was also necessary to image the beam spot at the exit of the gas jet for various measurements and the imaging system was focused accordingly.

With this setup, the vacuum laser beam profile through focus was measured at full laser power by moving the main focusing lens L1 axially by calibrated steps. The lens L1 was mounted on a motorized micrometer driven translation stage which has a position accuracy of ±7μm . The beam diameters at the half intensity points were measured horizontally and vertically. The plot of the averaged beam diameters vs. the focal position is shown in Fig. 7-2. By using a least squares fit to this curve, an average beam diameter of 18 μm can be obtained at the best focus condition. Using this beam diameter data, the peak vacuum intensity can be calculated as a function of axial position and is computed for a pulse with an energy of 250 mJ and duration of 1 ps, as shown in Fig. 7-3. This profile combined with the temporal profile gives the laser intensity at any given position and time.

The experiments discussed here were primarily conducted at a height of $300 \pm 25\mu m$ above the nozzle tip. For a reservoir pressure of 1500 psig the radial gas density profile is shown in Fig. 7-4. As the reservoir pressure is varied in the following experiments the peak density at the center of the gas jet will be stated. The transverse profile remains the same as given here.

7.4 Refraction

The refraction of the transmitted beam was measured by reimaging it onto a CCD camera with the L9 and M7 removed. The magnification was approximately 14 times. To have a complete image of the beam propagation and refraction through the gas jet, various combinations of focusing and imaging positions were employed. Various configurations used are shown in Fig. 7-5. In a), the laser is focused at the center of the gasjet and the center is imaged onto CCD. The images from this measurement show how much the laser beam was refracted prior to reaching focus. In this case the resultant image will be somewhat distorted due to additional refraction of the laser beam through the second half of the gas jet. The other three configurations, b), c), and d), all have the exit plane being imaged onto the CCD while the laser beam is focused at the center, exit, and entrance respectively. In these cases the CCD camera gives an undistorted image of the laser beam profile since no more refraction occurs after exiting the gas jet. These configurations give an indication of the propagation of the laser pulse through the gas jet.

With the laser beam focused into the center of the gas jet, two imaging configurations, a) and b), were used to record the beam refraction in a helium jet for a laser pulse energy of $180 \pm 15\ \mathrm{mJ}$. In Fig. 7-6, a set of images show the refracted beam spots at various densities when imaging the center of the gas jet onto CCD as defined in configuration a). The image in vacuum is essentially an overexposed image of the beam waist of the input laser beam formed by the focusing lens. As the gas density increases the transmitted energy decreases to 50 % of its initial value at the highest gas pressure, as will be discussed later in this chapter. It can be seen that at the highest density 4.9 x 10^{20} cm^{-3} most of the laser beam was scattered into a large circular area. The bright spot in the center which is much weaker than the vacuum focus is the unrefracted portion of the beam. As the pressure decreases, the size of the scattered beam area becomes monotonically smaller. Finally, with the gas absent, the main beam shrinks to a single spot where the intensity is very high. In the vacuum case shown in Fig. 7-6 the image was saturated and a weak rectangular image of ASE radiation from the e-beam amplifier is also visible. The contribution of ASE to the scattered light was estimated to be smaller than 7% based on an average ASE prepulse energy of 5% and postpulse energy of 5% of the main pulse. Thus once a significant portion of the main beam is refracted the ASE component becomes only a small part of this scattered light image. In comparing the image at low density (3.2×10^{19} cm^{-3}) with that in vacuum, not only is the size of the outer weak refracted image larger than the weak ASE image in vacuum, but the intensity of the scattered light is 50% higher than that in vacuum. Thus at this density the laser beam is still refracted and approximately 20% of the energy in the short pulse appears in the refraction spot. If the density were decreased further, the refracted beam spot from the short pulse would have been expected to be very weak and submerged in the background of ASE, which would be difficult to distinguish in the experiments.

When imaging the exit of the gas jet while the laser is focussed in the center as in configuration b), a set of images are obtained as shown in Fig. 7-7. Since this is not at the beam waist, the beam spots both of the refracted and unrefracted beams are larger than those when imaging the center as discussed above. As the pressure decreases, the refraction of the beam decreases similarly to that when imaging the center of the gas jet. To get a more quantitative treatment of the refraction, the size of each outer refracted spot is measured and shown in Fig. 7-8 with the horizontal axis being the density of the jet. It appears that the diameter of the refracted beam spot increases linearly with the jet density for both imaging configurations and pressures in the range of 1-5x10^{20} cm^{-3}. Furthermore, it is also instructive to determine an asymptotic angle as a measure of refraction. The asymptotic angle is defined as in the geometry shown in Fig. 7-9. The origin of the reference is assumed to be at the point O where the laser beam enters the gas jet. With this reference point, the asymptotic half angle is the arctangent of the ratio of the radius of the beam spot to the distance to image plane. This angle can be defined for both images: (i) taken at the midplane of the gas jet and (ii) at the exit of the gas jet. After setting up these conventions, the asymptotic refracted angles are calculated and plotted in Fig. 7-10 as a function of density. It can be seen that there is a difference in these angles at lower densities but at higher densities, the two set of angles approach each other. This is what one would expect in the case of refraction occurring at the entrance of the gas jet at high densities. These asymptotic angles provide a quantitative measure of refraction which can be used for comparison with simulations.

The third set of pictures, shown in Fig. 7-11, were taken for helium with both focusing and imaging at the exit of the jet as in configuration c). At lower densities, the beam was refracted slightly. As the density increases, the beam is refracted more. However, as before, a bright central spot is observed in all cases. The interesting point here is that a ring pattern is developed at a density of 4.9 x 10^{20} cm^{-3}. Combining with the above data from configuration b), we have Fig. 7-12 which shows the diameters of the outer beam refraction spot diameter vs. the density.

For nitrogen, similar experiments were carried out but with the exception that the refracted beams were imaged always at the exit of the jet and the laser beam was focused at the front (d), center (b), and exit (c) respectively, as illustrated in Fig. 7-5. Figs.7-13-Fig.7-15 show the corresponding refracted beam spots at the above mentioned focusing positions. Taking the same reference system as for helium above, the refracted beam diameters and asymptotic angles are plotted in Fig.7-16 and Fig.7-17 respectively. The overall features are similar to those for helium jet. There is also an interesting feature of ring-shaped structures for nitrogen when both focusing and imaging at the exit of the jet when the density is larger than 1×10^{20} cm^{-3}. This behavior is similar to that for helium in Fig. 7-11 except the latter occurs at a higher density of 4.9×10^{20} cm^{-3}. At densities below 1×10^{20} cm^{-3} , the asymptotic angles are quite different for the different geometries. However, as the density increases, the asymptotic angles approach each other. Since nitrogen has two atoms per molecule and more electrons than helium, it has a higher electron density and refracts more than helium for the same neutral gas density.

7.5 Visible emission and UV side scattering

To investigate the propagation of the ultrashort pulse through the high density jet, both the visible emission of helium and the UV side scattering were imaged spatially. The radiation from the plasma in the transverse direction was collected by a triplet lens L2 which collimated and sent the light to a beam splitter M3. This beam splitter was actually a multi-layer dielectric high reflector for KrF laser radiation with a wavelength of 248 nm at 45 degrees of angle of incidence which reflected all the UV laser radiation and passed over

90 % of the visible radiation. The UV radiation was directed to a UV streak camera by a mirror M2 and lens L5. To avoid the background laser radiation scattering from the nozzle tip itself, a knife edge was placed at the image plane of L5. By properly adjusting the position of the knife edge, the scattered UV light from the nozzle could be blocked. The streak camera was operated at a streak speed of 15 mm/ns so that for the one picosecond scattering event the streak camera acted as a still frame camera but still discriminated against stray scattered from inside the chamber which arrived at different delay times. Thus the image on the streak camera took a snapshot of the self scattering of the laser light from the plasma.

The visible radiation which passed through M3 was focused onto a vidicon by lens L7. In front of the vidicon a narrow band filter was used which passed the radiation of the He II transition n=4-3 at 468.5 nm with a narrow spectral band of 1.5 nm. This filter gave good discrimination against the closest neighboring line at 471.3 nm from He I. In a cold plasma the majority of emission from the n=4-3 transition of He II occurs upon recombination from fully ionized helium to highly excited levels of single ionized helium. Thus carrying out such monochromatic imaging of the helium plasma, the region of the fully stripped helium ion potentially could be identified. The size and shape of the plasma channel image revealed the propagation of the ultrashort pulse in the plasma. It also gave an indication of the subsequent hydrodynamics of the expanding blast wave since this was a time integrated result.

The plasma channel formation in helium was very much associated with the amount of ASE accompanying the incident laser light. For a clean short pulse, the beam seems always to be refracted. To study the effect of ASE on plasma formation, laser shots with various levels of ASE were carried out to explore the propagation dynamics. In the following data, the incoming laser is focused at the center of the jet.

As the timing and amplifier gains in the laser system were adjusted so that the amount of ASE was reduced, a clean short pulse was formed, with post and prepulse energies of 5% relative to the main picosecond pulse. Fig. 7-18 shows a typical visible emission profile of helium plasma and the corresponding UV side scattering image for a laser shot with a clean pulse of 1 ps at a peak vacuum intensity of 1×10^{17} W/cm^2. It can be seen that the visible profile starts with a wider column and gets narrower as the laser propagates into the jet. This profile only reflects the final He II emission boundary in the expanding blast wave and implies more energy deposition in the first half of the gas jet in agreement with modeling code calculations presented in Chapter 9. The real dynamics of the laser pulse in the plasma can be seen in UV side scattering. UV scattering is observed throughout the high pressure region of the gas jet. However, brighter emission regions are observed at the ends of the high density region. The first scattering spot to appear is located 316 μm into the jet from the front edge of the jet. When the laser pulse passes the center and reaches the second half of the jet, there is another spot occurring which is generally larger in size. The center of the second spot is 727 μm from the front edge of the jet. Compared with the visible emission profile, this corresponds to the region of the visible profile where the plasma channel becomes narrower. A primary mechanism for the UV sidescattered image is Thomson scattering from the plasma which is proportional to electron density. The two scattering spots observed, instead of one spot corresponding to a peak electron density point in the plasma, could indicate some enhancement of normal Thomson scattering from the entrance and exit regions of the plasma. Because of the limited amount of UV image data taken and the lack of spectral information on the scattered signal a more detailed analysis of the data was not carried out.

When the timing and amplifier gains are adjusted so that there is a sizable ASE prepulse, the main short laser pulse will interact with a preformed plasma whose property depends on the intensity of the prepulse. For an ASE prepulse of 18% of the total energy, the shape of the visible emission changes as shown in Fig. 7-19. Instead of decreasing in width, the plasma channel width becomes larger as the laser propagates through the gas jet. At the end of channel, the channel has its maximum width. In viewing the UV side scattering as shown in Fig. 7-19, there is a scattering spot corresponding to the second half of the plasma channel. When the energy of the prepulse is increased to 35 % of the total energy, the plasma channel becomes uniform across the whole length as shown in Fig. 7-20. The total length of the channel is limited by the length of the jet to 1 mm. It is interesting to note from Fig. 7-20 that the UV scattering is significantly reduced so that it is not visible using the same gain as for the previous images. In this case it appears that the plasma channel formed by the large ASE prepulse confines the picosecond laser pulse leading to uniform propagation through the gas jet with little defocusing and refraction.

Given several nanoseconds to expand the electron densities would be somewhat reduced from the starting density leading to reduced UV scattering levels.

7.6 Spectral diagnostics of beam propagation

The plasma created by a laser pulse will generally recombine into highly excited states of the next lower ionization levels which in turn will decay through emission of radiation. The radiation is thus a signature of the plasma state. This is true for cold, well underdense plasmas where collisional excitation of emission lines is weak. However, some collisionally excited emission can also occur over long periods of time as the plasma expands and slowly cools, particularly in the high density walls of the expanding blast wave. At the entrance and exit of the gas jet the plasma expands axially into vacuum and cools rapidly. In these cases the line emission is expected to result pre-dominantly from recombination processes. In the present experiment, the visible emission due to recombination of the fully stripped helium ions, He II, at 468.5 nm was used as a spectral diagnostic to outline the region of fully ionized plasma and thus the propagation of the laser pulse through the gas jet. The idea is that where there is He II, there is a laser intensity over 5 x 10 ^{15} W/cm^2 which is the multiphoton ionization threshold for He II. If the laser beam is not refracted, similar He II emission would be observed at both the entrance and exit of the gas jet. If refraction occurs, the spectra of He II at different locations should give an indication of the beam propagation effects.

The He II line was monitored in three directions of 0, 90 and 135 degrees imaged at the exit, middle and entrance of the gas jet respectively. For 0 degrees, lens L9 and mirror

M7 were in place as shown in Fig. 7-1. Through L3, L9, M7 and M5 the visible emission from the exit of the gas jet was imaged onto the 30 μm entrance slit of the monochromator MC1 coupled with an OMA. This leads to an imaging system of f/8 giving a focal depth of 240 μm at the entrance slit of the monochromator which corresponds to a ~ 80 μm thickness at the exit of the plasma. Thus, the emission from the region prior to the exit of the jet forms a large blurred image at the slit of the monochromator which is estimated to be contributing < 10% to the spectrum of interest. The monochromator had a grating of 1180 line/mm giving a resolution of 0.3 nm when an entrance slit of 30 μm was used. Removing L9, M7 and M6 the light from the entrance of the gas jet viewed at 135 degrees, followed the path of L4, M1, M4, L8, M5, was imaged onto MC1 and then to the OMA. If M6 was put back in place, then the light from the middle of the gas jet viewed at 90 degrees was routed to MC1 through L2, M6, M4, L8 and M5 and from there onto the OMA/monochromator system.

In Fig. 7-21 , a group of He II spectra is shown corresponding to the entrance, middle and exit of the gas jet viewed in the directions of 135, 90, and 0 degrees respectively at a gas density of 4.9×10^{20} cm^{-3} and vacuum laser intensity of 1×10^{17} W/cm^2. At 135 degrees, there is a strong He II line at 468.5 nm. This came from the entrance region of the gas jet. At 90 degrees, the spectrum becomes broadened. The broadening arises from the high density in the center of the jet. Because of the broadening there could be some partial contribution from a HeI line at 471.3 nm. Another feature is that the spectra obtained from the center of the gas jet are asymmetric, with the longer wavelength wing falling off more rapidly than the blue side wing. Since the He II line at

468.5 nm is from the n=3-4 transition, the asymmetry may mean that the n=4 level is more mixed with the high lying levels above it than the n=3 level with its neighboring levels. At the exit of the gas jet viewed at 0 degrees, there is a smaller signal at 468.5 nm and an almost equally strong He I line at 471.3 nm. This implies that there is not enough laser intensity to fully ionize all atoms at the exit. In other words, the plasma at the exit is only partially ionized. This means that the laser beam is refracted significantly since the energy loss due to absorption and scattering is not a large fraction of the initial energy as will be shown later. Note that for peak plasma temperatures of a few hundred eV, as expected here, the Doppler broadening and shifts will be a fraction of a nanometer consistent with the narrow line spectra observed at the entrance and exit of the gas jet.

To confirm the beam refraction, two more pieces of evidence will be presented. First, the spectra from the exit of the gas jet viewed at 0 degrees were correlated with the visible plasma channel imaging as discussed above. In Fig. 7-22 , two spectra are shown. The one with enhanced He II line emission corresponds to the elongated plasma channel in Fig. 7-23 while the weak He II spectra corresponds to the short plasma channel. The elongated plasma channel implies that the laser beam undergoes less refraction and keeps its high intensity at the exit producing more doubly ionized helium so that the enhanced He II line is observed. On the other hand, the short plasma channel means the beam is refracted before it reaches the exit thus reducing its intensity. The less intense laser beam will produce only partially ionized plasma which gives weak He II emission together with He I lines.

The second evidence for beam refraction came from reducing the jet pressure since at lower pressure the beam is not expected to be refracted as much and has a higher laser intensity at the exit which will produce the He II line emission. In Fig. 7-24 , the spectra of He II taken at the exit of the gas jet viewed at 0 degrees are shown for densities of 4.9 x 10^{20} cm $^{-3}$, 3.7 x 10^{20} cm $^{-3}$, and 2.2 x 10^{20} cm $^{-3}$. At the highest density of 4.9 x 10^{20} cm $^{-3}$, both the He I line at 471.3 nm and the He II line appear and have approximately same intensity. As the density is reduced to 3.7 x 10^{20} cm $^{-3}$ the He II line increases dramatically. This means that the laser intensity at the exit is larger due to less refraction. With further decreases in density, the over all signal is reduced and relative intensities of the signals of HeII to He I are roughly the same.

In summary, the spectral emission is a good diagnostic of the beam propagation. As the laser beam enters the jet, it will fully ionize the atoms. This is where the strong He II line at 468.5 nm is observed. After the beam gets into the center of the jet, the plasma is surrounded by high density gas and the emission is broadened as observed from the 90 degree spectra. At the exit the He II emission is reduced. Thus the He II emission acts as threshold intensity diagnostic which in turn is a diagnostic of the beam propagation.

7.7 Energy Transmission

The transmission of the input KrF beam through the gas jet was measured by using a pair of calorimeters PY7 at the input and PY2 for transmitted energy. The ratio of the reading of PY7 to the reading of PY2 with gas relative to that in vacuum gives the absolute transmission. The transmission was studied as a function of gas density. Fig.7-25 shows the reduction of energy transmitted through the gas jet into an f/2.5 cone angle for helium, neon, nitrogen and argon respectively. It can be seen that there is more than 90% transmission for helium for densities below 1.5×10^{20} cm $^{-3}$ and over 55% for densities larger than 4.5×10^{20} cm $^{-3}$. For high Z species, on the other hand, transmission is dramatically reduced. Neon transmission is less than for helium but greater than for nitrogen and argon. The transmission for nitrogen and argon is reduced to $\approx$ 30% for densities $> 5 \times 10^{19}$ cm $^{-3}$ and then levels off at about 20%.

7.8 Discussion

The refraction of laser radiation propagating in the forward direction can occur from a number of mechanisms including ionization induced refraction, ponderomotive and thermal filamentation and forward Raman scattering. A search for forward Raman scattered light using a spectrograph to analyze the transmitted radiation indicated that Raman scattered radiation was below the detection limit of $\sim 10^{-5}$ of the incident light. Thus, Raman scattering is not an important mechanism for the present experimental intensities.

The ponderomotive potential ranges from U_{pm}=57.7 eV to 577 eV for KrF laser intensities of 10^{16} to 10^{17} W/cm^2. Electrons with an energy of 577 eV have a velocity of 1.5×10^9 cm/s and thus could travel a distance of 15 μm in one picosecond. Thus some of the electrons can be expelled to the shoulders of the 18 μm diameter beam at peak intensity. However only a small number of electrons will be expelled before an ambipolar potential equal to the ponderomotive potential is established. Particle in cell simulations by Penetrante and Bardsley [1] have indicated an electron density shoulder of ~10^{18} cm^{-3} for 50 fs XeCl laser pulses at a higher intensity of 10^{18} W/cm^2. For our high electron densities of 10^{20}-5×10^{21} cm^{-3} in the present experiments such a small perturbation in the electron density profile will have a negligible effect on beam propagation. The ponderomotive heating of such a small fraction of the electron population will also have little effect on the heating of the high density plasma.

Once an ambipolar potential equal to the ponderomotive potential is established then the ions will be accelerated outwards from the plasma column. The expulsion of ions, together with electrons, from the plasma column can lead to much larger perturbations in electron density and result in ponderomotive filamentation and self focusing. However a growth time of the order of picoseconds must be allowed for the ions to move and refracting structures to be formed. The scattering angle corresponding to the fastest growing mode for filamentation is given by [2,3]

$$\theta_r \approx \frac{1}{2}\left(\frac{\upsilon_{osc}}{\upsilon_{th}}\right)\left(\frac{\omega_{pe}}{\omega_0}\right) \qquad (7.1)$$

Estimating approximate parameters for our gas jet and allowing for some defocusing due to ionization induced refraction, we can take a temperature of 20 eV, an intensity of 10^{16} W/cm^2, corresponding to $\upsilon_{osc}/\upsilon_{th} = 3.4$, and a fully ionized helium plasma with atomic density of 2×10^{20} cm^{-3} which results in a value of $\theta = 0.25$ radians or 14 ^{0}. This is comparable to measured values of 15^0 for this density as shown in Fig. 7-10 where the predicted scattering angle is plotted as a function of density for a value of $\upsilon_{osc}/\upsilon_{th} = 3.4$. This formula for filamentation angle has been used to explain simulation and experiments involving the interaction of a 100 ps, $2\text{x}10^{15}$ W/cm^2 1.06 μm laser pulse with a preformed plasma with an electron density of 0.2 n_c [2]. The growth rate, γ, for ponderomotive filamentation is given by Eqn. 8.21 from Kruer [4] in the appropriate limit for the present condition that $\gamma >> kCs$,

$$\gamma = \frac{\upsilon_{osc}}{2c}\omega_{pi} \qquad (7.2)$$

where k is the wavenumber of the transverse ion perturbation, $C_s = \sqrt{ZT_e / m_i}$ is the ion acoustic velocity and $\omega_{pi} = \sqrt{m / Zm_i}\,\omega_{pe}$ is the ion plasma frequency. Evaluating for the peak intensity and density expected in the present experiment, $I=10^{16}$ W/cm^2 and n_e=0.1 n_c gives a growth rate of $4.1 \text{ x}10^{11}$ s^{-1}. Since a few of e-foldings of growth are required to produce significant filamentation it appears that our 1 ps pulse will not allow sufficient growth time for ponderomotive filamentation. It is expected that for our conditions where $\upsilon_{osc}/\upsilon_{th} > 1$ that ponderomotive filamentation will dominate thermal filamentation but thermal filamentation in this regime has not been investigated in detail yet.

The dominant mechanism for refraction of the incident laser radiation is the ionization induced refractive index profile. At the highest helium density (and lower densities of other gases) the electron density in the central region of the gas jet will be of the order of $n_e = 1 \times 10^{21}\,\text{cm}^{-3}$. Assuming an average beam radius of ~ 30 μm through this region (allowing already for significant refraction) the refractive index gradient can be estimated from the electron density divided by the radius. The deflection angle due to refraction can then be estimated to be $\theta = (1/2n_c)(dn_e/dy)L$ where L = 426 μm is the half path length between the half density points of the gas jet. This leads to an estimate of deflection angle of $\theta \cong 0.46$ radians or 24^0. This is larger than but comparable to the scattering angles measured from the CCD camera images at the exit of the gas jet as shown in Figs. 7-10 and 7-17. A more detailed calculation of the refraction due to ionization will be given in Chapter 9 where some modeling calculations will be presented.

The intense spots in the center of the refracted radiation observed at the exit of the gas jet, particularly when focused at the exit of the gas jet as shown in Figs. 7-11 and 7-15 , are difficult to explain. Together with the ring patterns observed around these spots the patterns are suggestive of self focusing in the gas jet. In this case, when focusing right through the gas, the long interaction length approximates a static background gas condition. Self focusing in static background gases has been well known for two decades but has generally been observed for longer pulselengths.

At the highest electron densities obtained in nitrogen gas ionized to Z=+5 the electron density at the center of the gas jet is $n_e \cong 5 \times 10^{21} \text{cm}^{-3}$. The critical power for relativistic self focusing in this case is P_c=0.06 TW. Thus, the peak power of 0.2 TW would exceed this critical power. Allowing for absorption in the entrance region of the gas jet the laser power at the center of the gas jet would be approximately at the threshold for relativistic self focusing and thus some enhancement of the radiation on axis may be expected. Self focusing effects attributed to relativistic self focusing using subpicosecond KrF laser pulses have been reported by Borisov et al [5] in static gas fill targets of nitrogen.

Recently more evidence of relativistic self focusing has been reported for peak powers of five times the critical power using gas jet targets irradiated with 400 ps, 1.06 μm laser pulses [6]. The intense central spot observed in the present experiment for nitrogen gas targets may be due to a combination of regular self focusing in the breakdown region of the gas target together with initial focusing effects at the threshold for relativistic self focusing. For the bright central spot observed using the helium gas jet targets relativistic self focusing cannot play a role since the peak densities are five times lower than the nitrogen target and thus the critical power is above that available in the present experiment.

A discussion of the absorption measurements together with an analysis of expected plasma temperatures will be presented in Chapter 9.

References

1. B. M. Penetrante and J. N. Bardsley, Phys. Rev. A 43, 3100 (1991).
2. S. Wilks, P. E. Young, J. Hammer, M. Tabak, and W. L. Kruer, Phys. Rev. Lett. 73, 2994 (1994).
3. W. L. Kruer, Comments Plasma Phys. Controlled Fusion. 9, 63 (1985).
4. W. L. Kruer, The Physics of Laser Plasma Interactions, , Addison-Wesley , Redwood City, 1988.
5. A. B. Borisov, A. V. Borovskiy, V. V. Korobkin, A. M. Prokhorov, O. B. Shiryaev, X. M. Shi, T. S. Luk, A. M. McPherson, J. C. Solem, K. Boyer, and C. K. Rhodes, Phys. Rev. Lett. 68, 2309 (1992).
6. P. Monot, T. Auguste, P. Gibbon, F. Jakober, and G. Mainfray, A. Dulieu, M. Louis-Jacquet, G. Malka, and J. L. Miquel, Phys. Rev. Lett. 74, 2953 (1995).

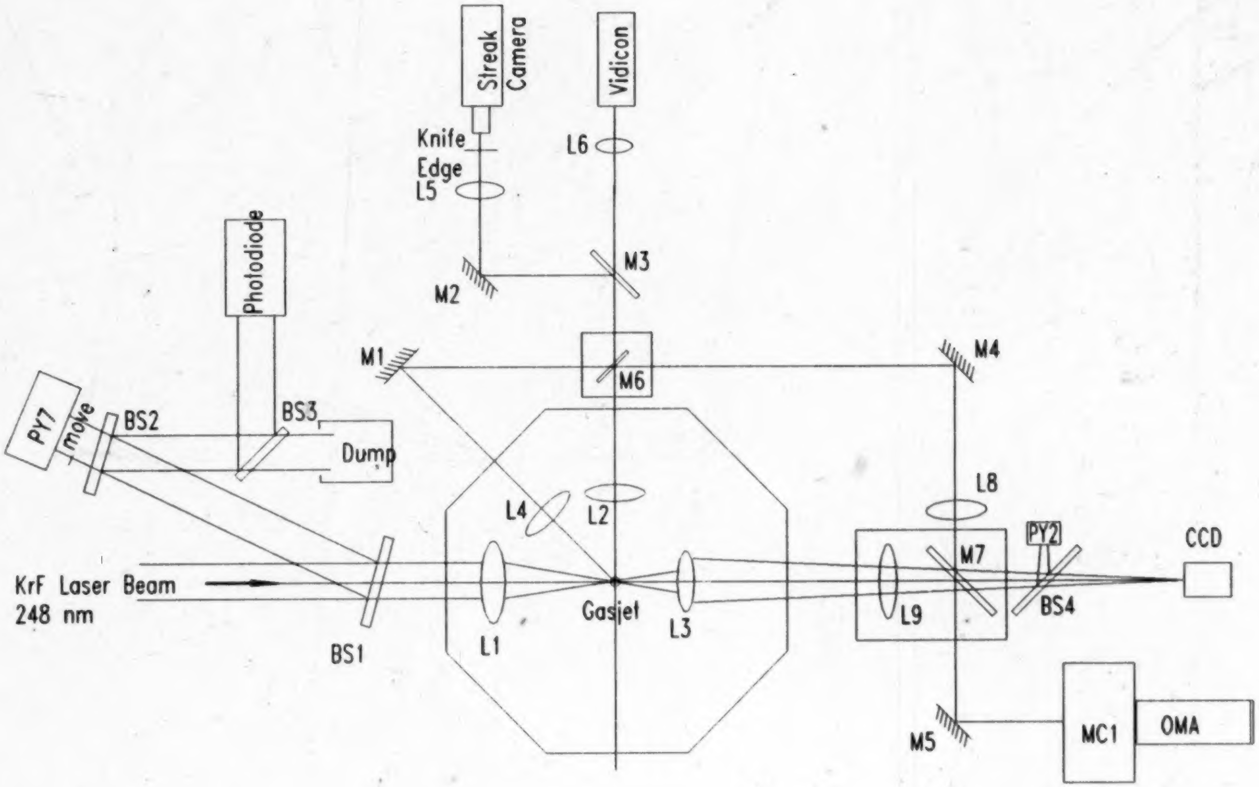
Streak Camera
Vidicon
Knife Edge
L5
L6
Photodiode
M2
M3
M1
M6
M4
PY7
move
BS2
BS3
Dump
L4
L2
L8
PY2
CCD
KrF Laser Beam
248 nm
BS1
L1
Gasjet
L3
M7
L9
BS4
M5
MC1
OMA

Fig. 7-1 Experimental setup for beam propagation study

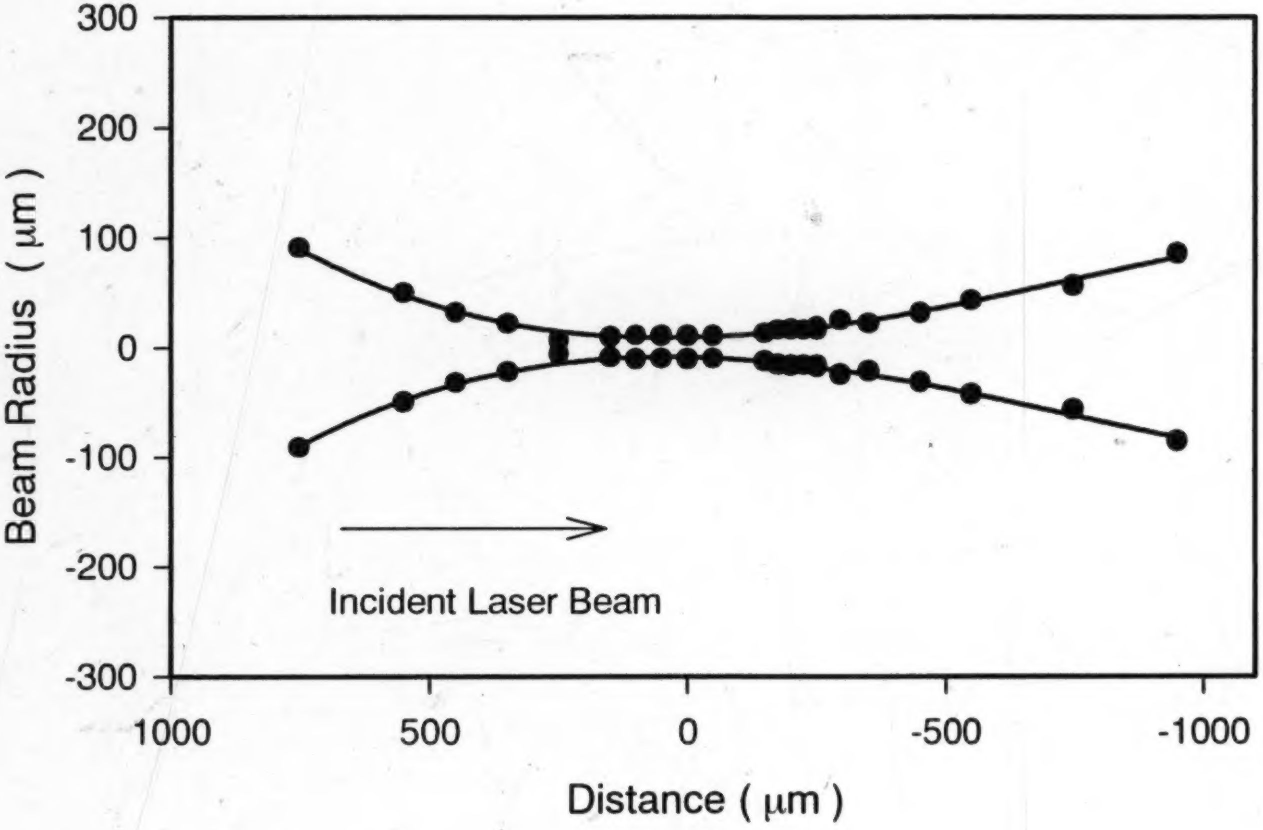

Fig. 7-2 Laser beam profile passing focus in vacuum

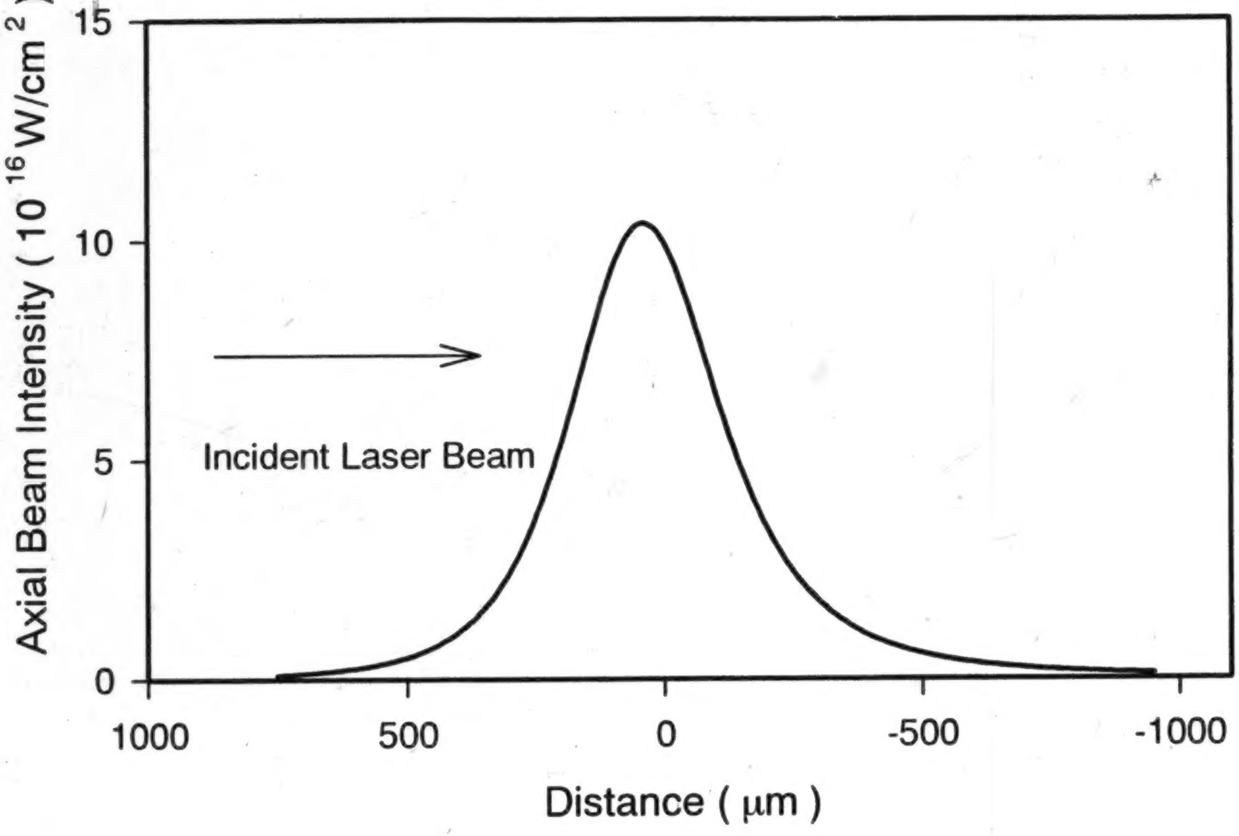

Fig. 7-3 Plot of peak vacuum intensity vs. position through gas jet region

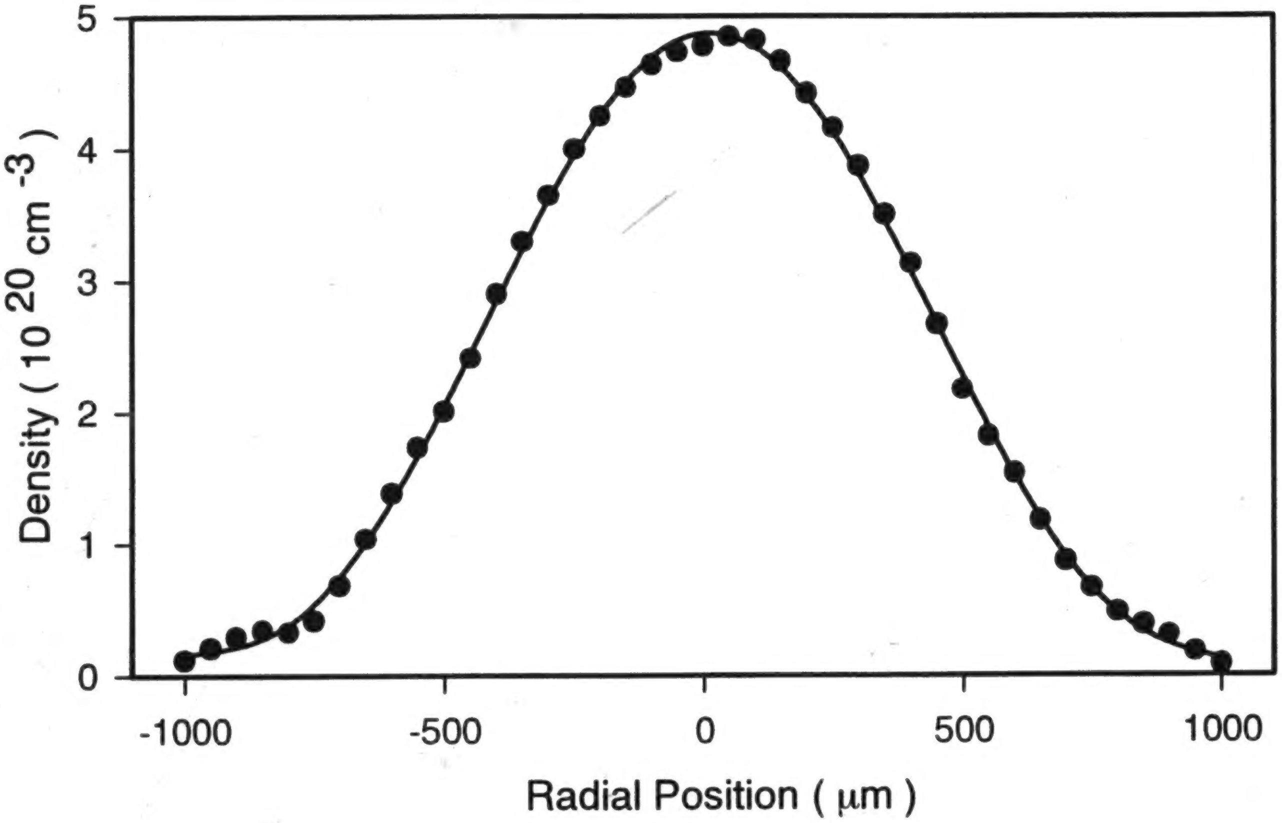

Fig. 7-4 Radial density profile at a distance of Z=300 μm above nozzle tip

a) Focusing at the center, imaging at the center

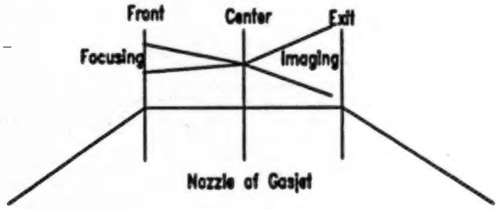
Front
Center
Exit
Focusing
Imaging
Nozzle of Gasjet

b) Focusing at the center, imaging at the exit

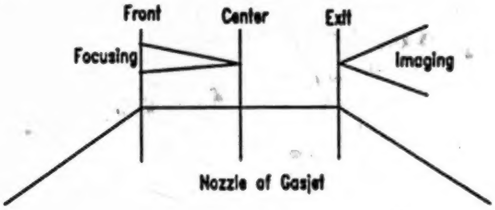
Front
Center
Exit
Focusing
Imaging
Nozzle of Gasjet

c) Focusing at the exit, imaging at the exit

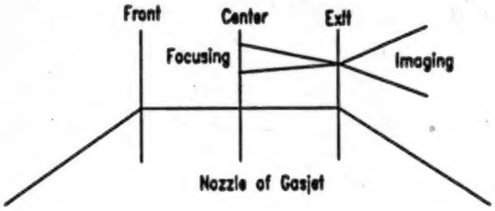
Front
Center
Exit
Focusing
Imaging
Nozzle of Gasjet

d) Focusing at the front, imaging at the exit

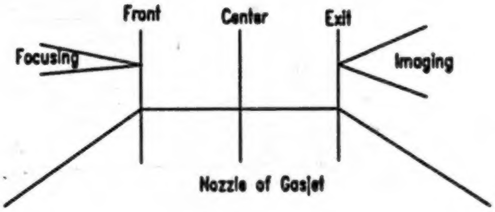
Front
Center
Exit
Focusing
Imaging
Nozzle of Gasjet

Fig. 7–5 Focusing and imaging geometries

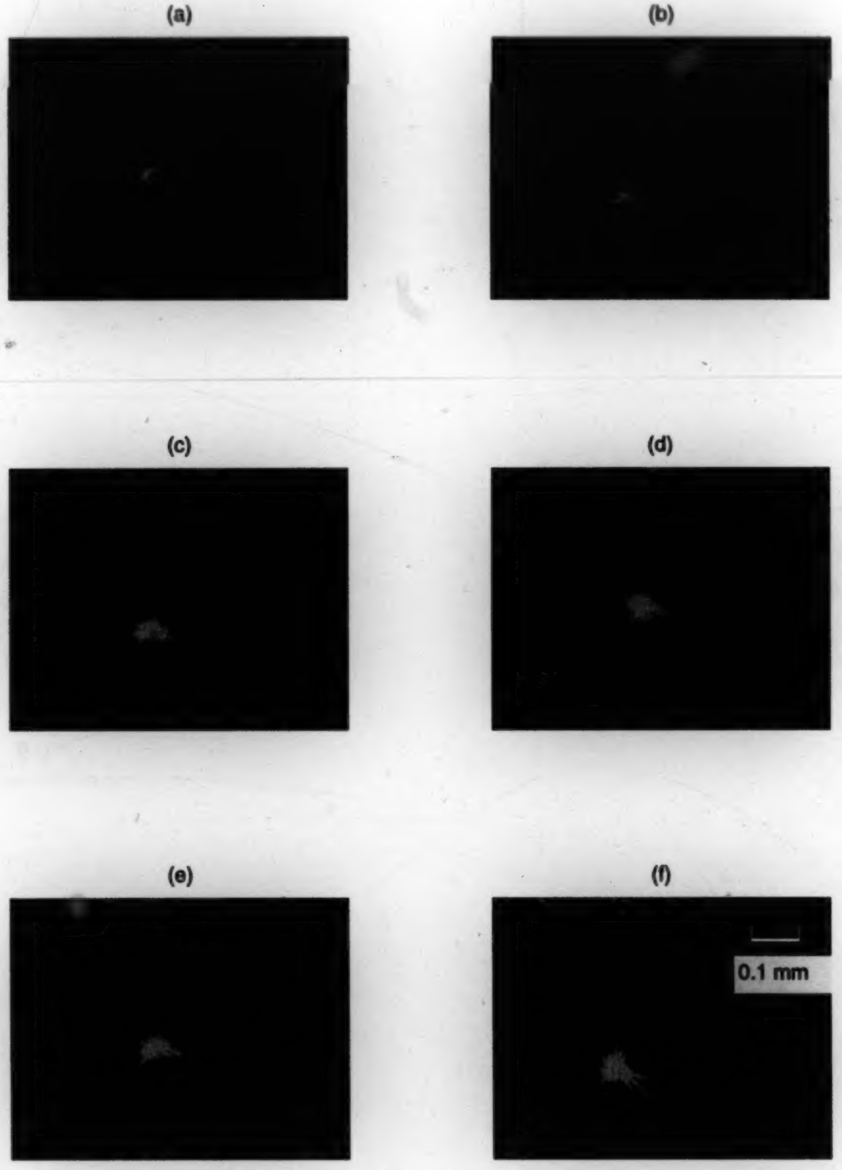

Fig. 7-6 Beam spots at the center of the gas jet for helium as a function of neutral gas density when the laser beam was focused at the center of the gas jet. (a) 49, (b) 32, (c) 16, (d) 6.5, (e) 3.2 times 10^{19} cm $^{-3}$, and (f) vacuum.

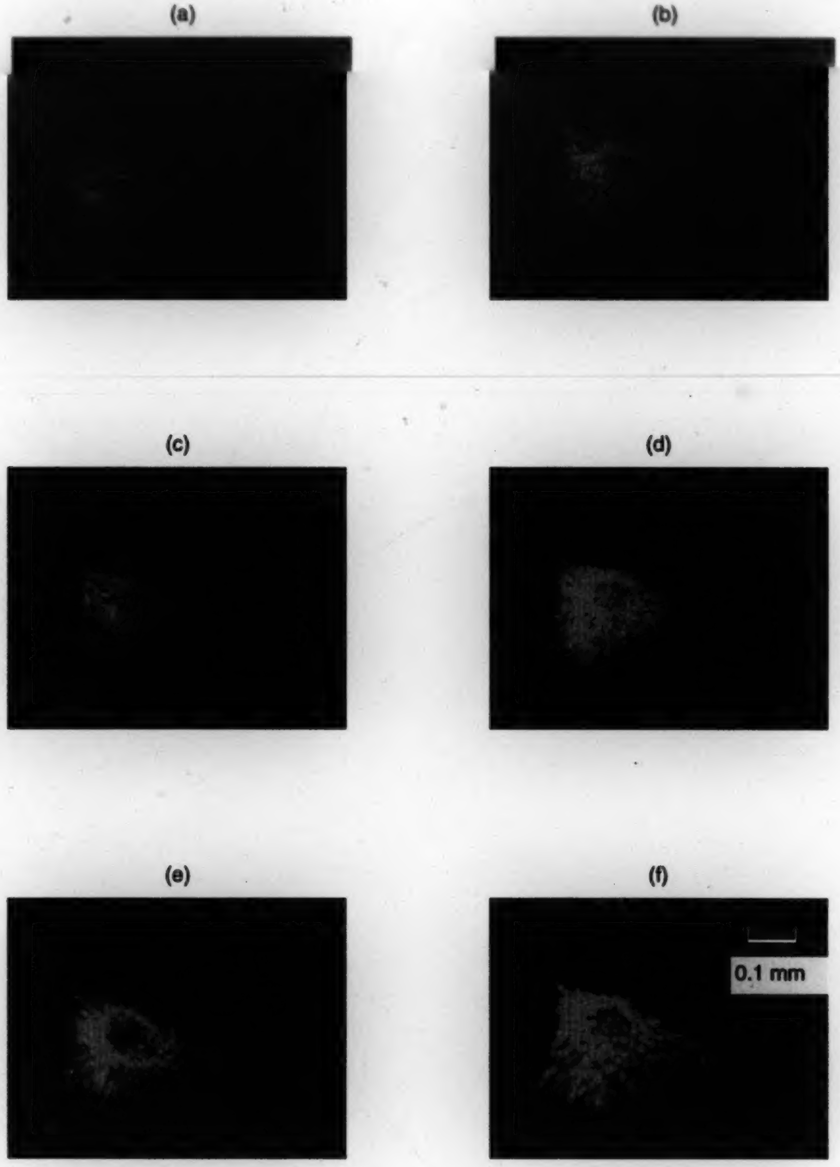

Fig. 7-7 Beam spots at the exit of the gas jet for helium as a function of neutral gas density when the laser beam was focused at the center of the gas jet. (a) 49, (b) 32, (c) 16, (d) 6.5, (e) 2.3 times 10^{19} cm $^{-3}$, and (f) vacuum.

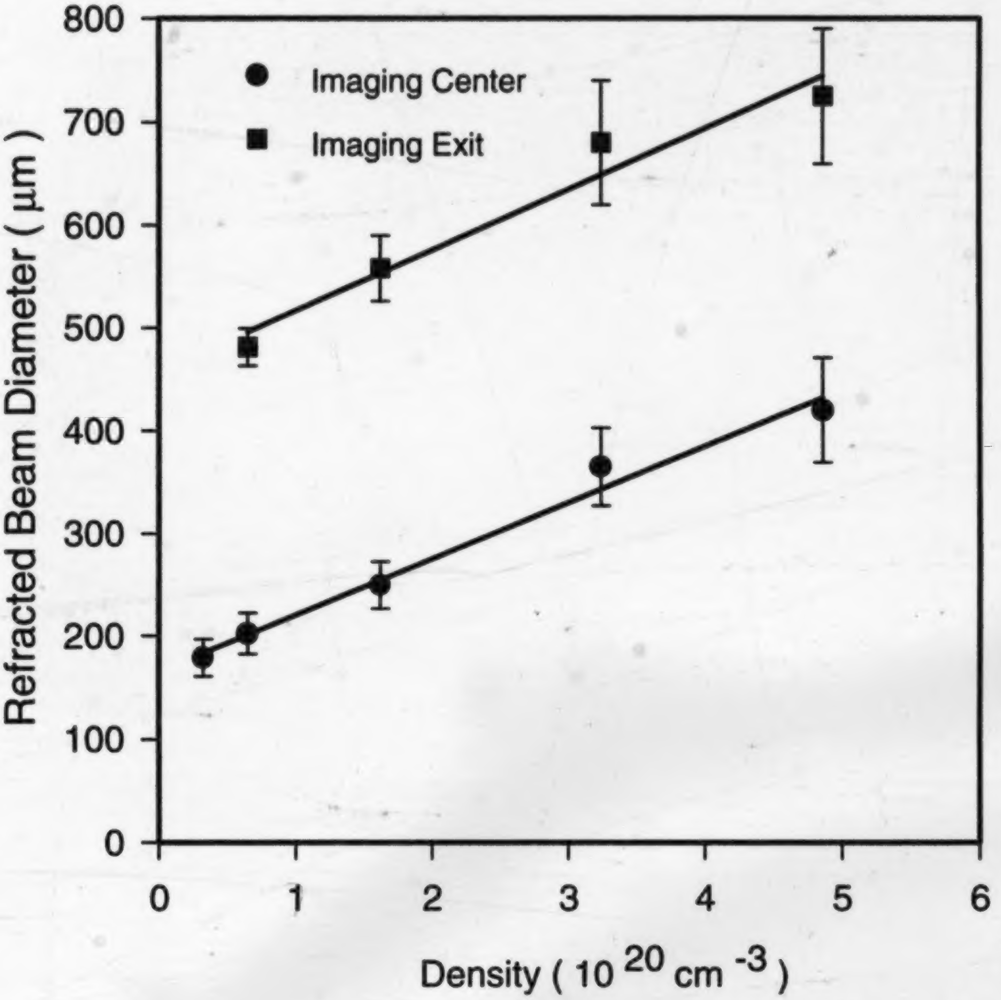

Fig. 7-8 Refractive beam diameters as a function of density for helium when a laser beam is focused at the center of the jet. ● imaging center ■ imaging exit.

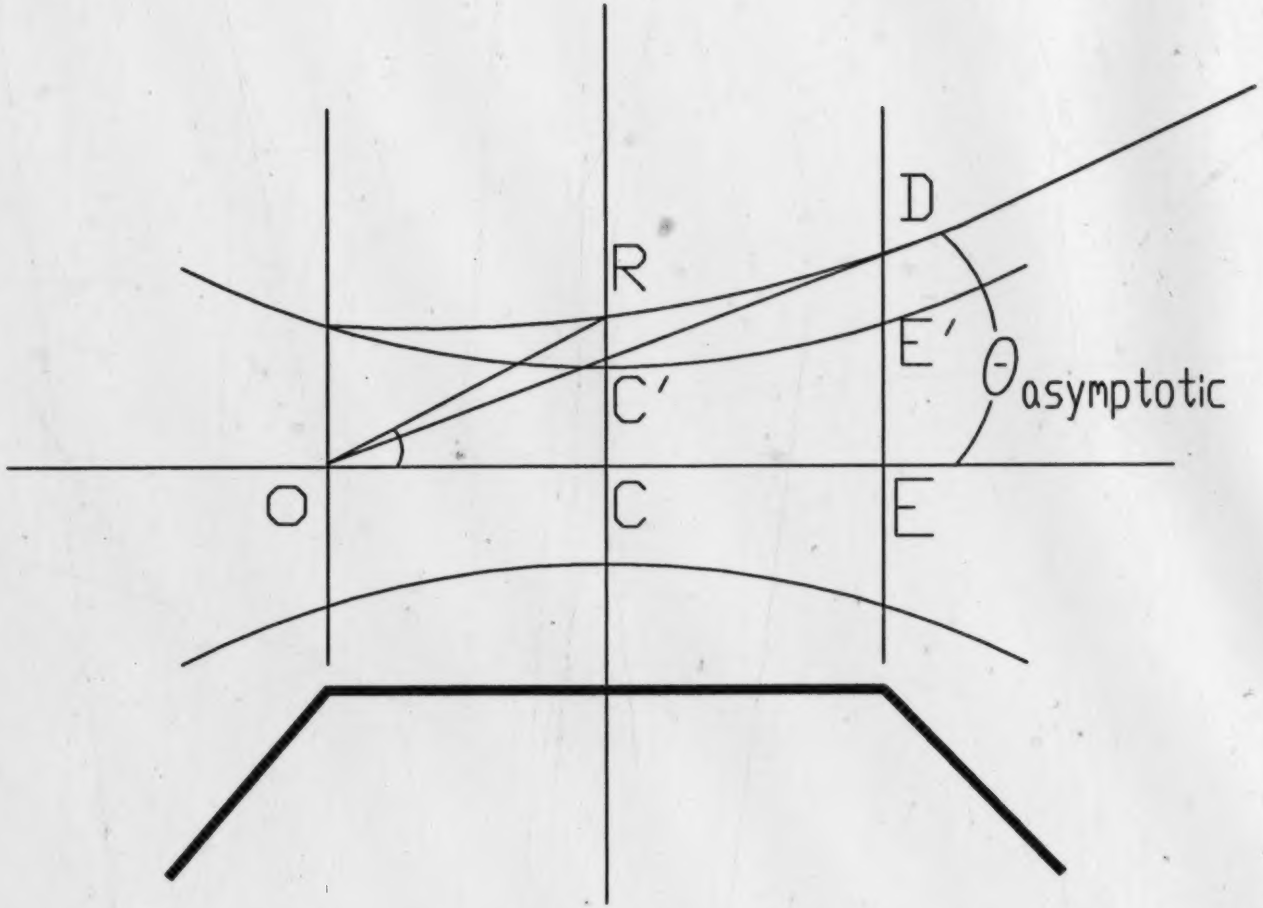
D
R
E′
$\theta_{asymptotic}$
C′
O
C
E

Fig. 7-9 Geometry of asymptotic refracted angle

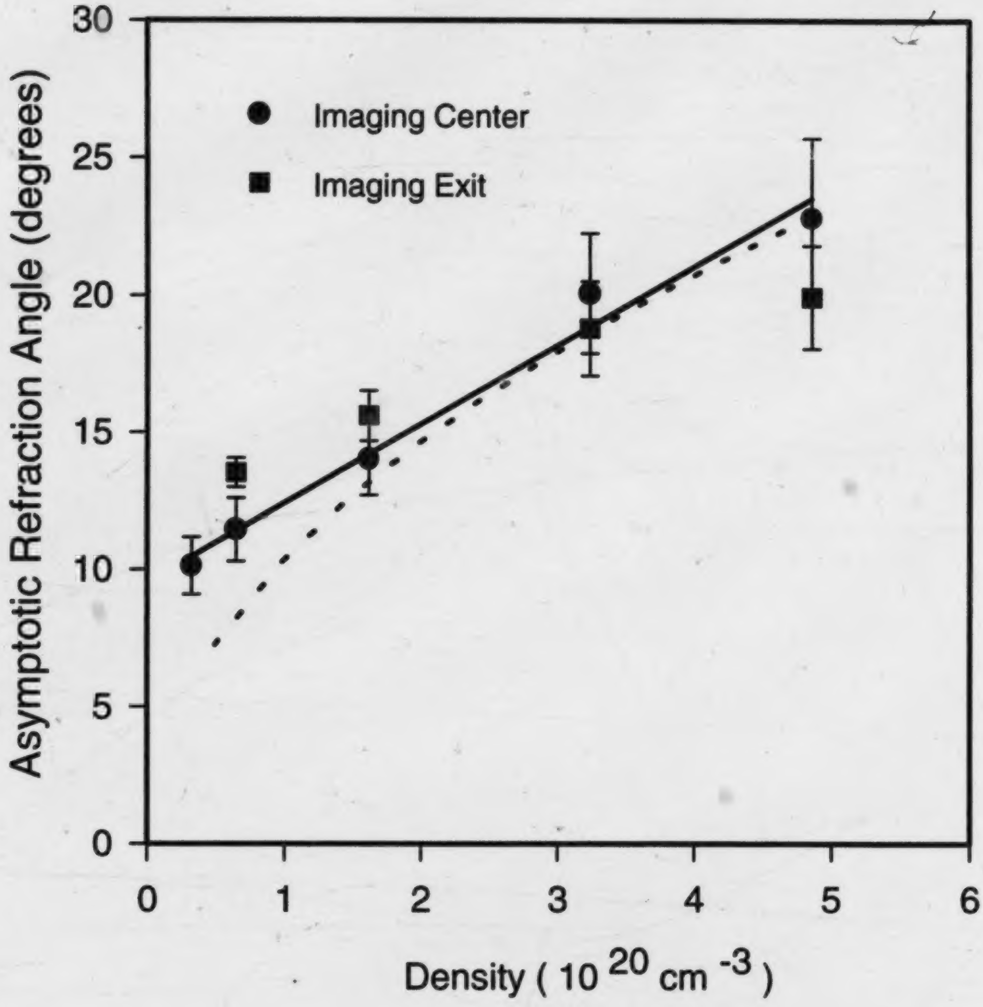

Fig. 7-10 Asymptotic refractive angle as a function of atomic density for helium when a laser beam is focused at the center of the jet. ● imaging center ■ imaging exit. The dashed line is the theoretical prediction using Eqn.7.1.

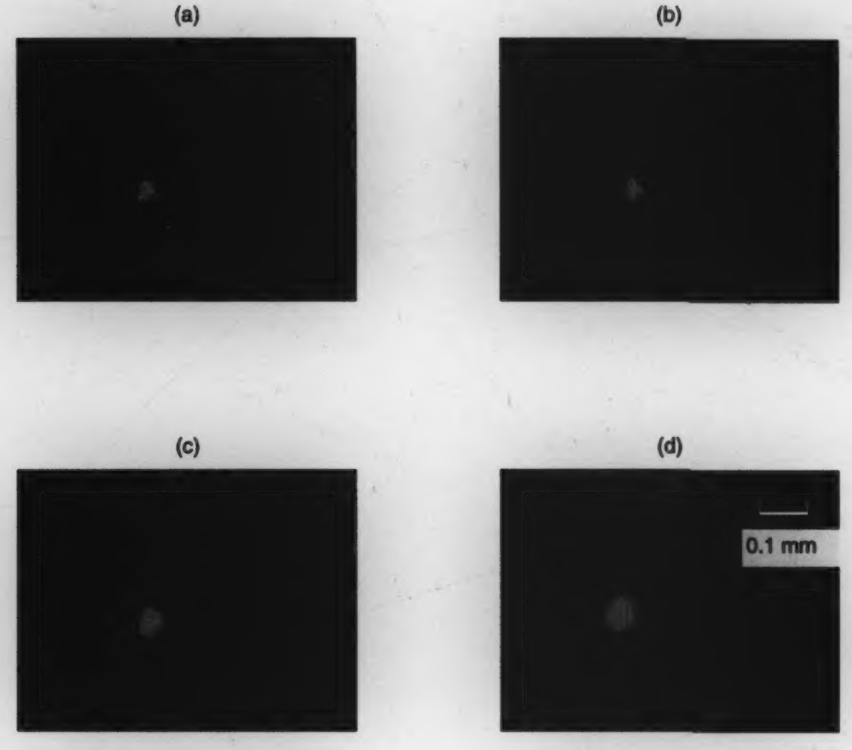

Fig. 7-11 Beam spots at the exit of the gas jet for helium as a function of neutral gas density when the laser beam was focused at the exit of the gas jet. A ring-shaped structure develops at a density of 4.9×10^{20} cm^{-3}. (a) 49, (b) 32, (c) 16, and (d) 8.1 times 10^{19} cm^{-3}.

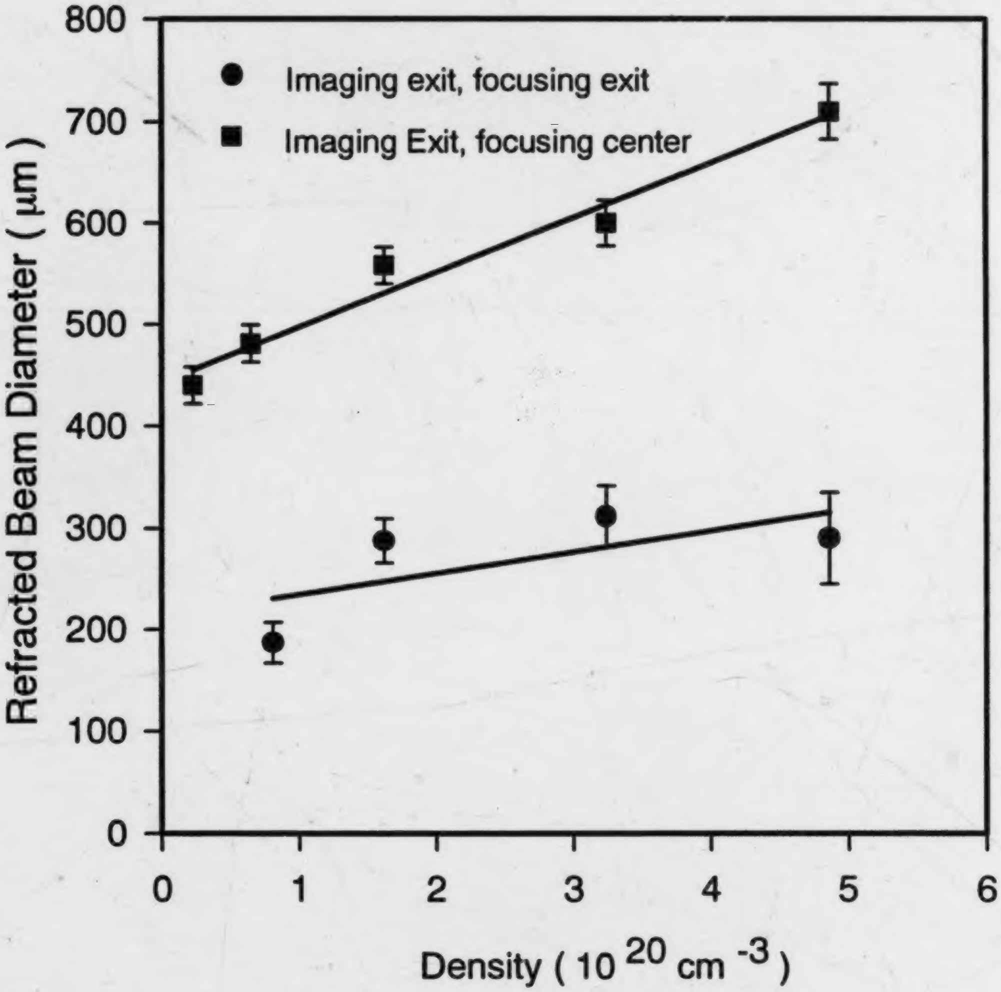

Fig. 7-12 Refractive beam diameters as a function of density for helium when imaging at exit. A laser beam is focused at exit ● and center ■ .

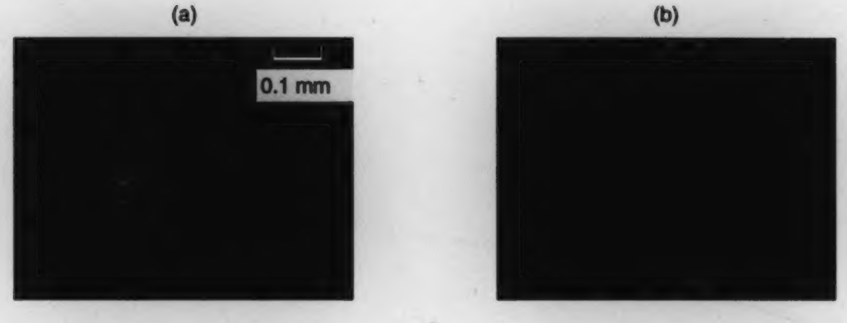

Fig. 7-13 Beam spots at the exit of the gas jet for nitrogen as a function of molecular gas density when the laser beam was focused at the entrance of the gas jet. (a) 4.5 and (b) 16 times 10 ^{19} cm $^{-3}$.

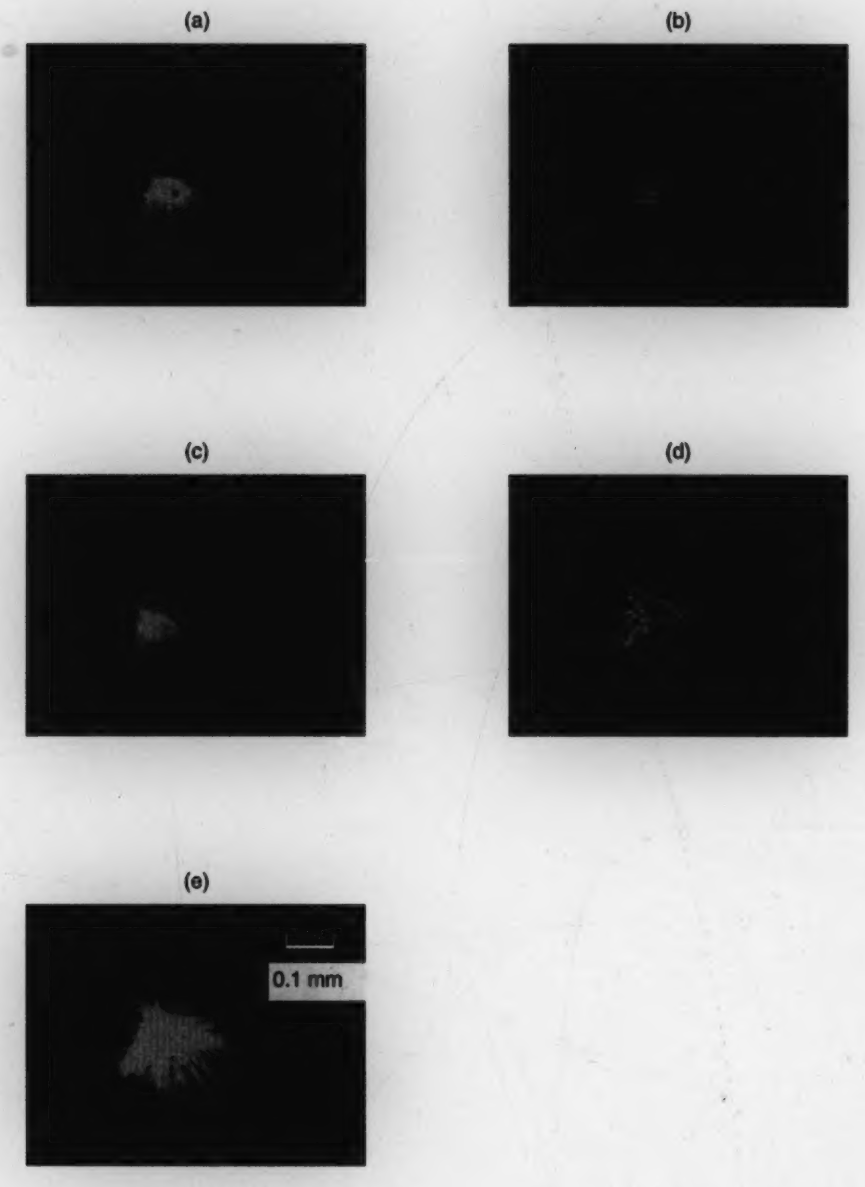

Fig. 7-14 Beam spots at the exit of the gas jet for nitrogen as a function of neutral gas density when the laser beam was focused at the center of the gas jet. (a) 49, (b) 32, and (c) 6.5 times 10^{19} cm^{-3}, and (d) 2x attenuated in vacuum, and (e) vacuum.

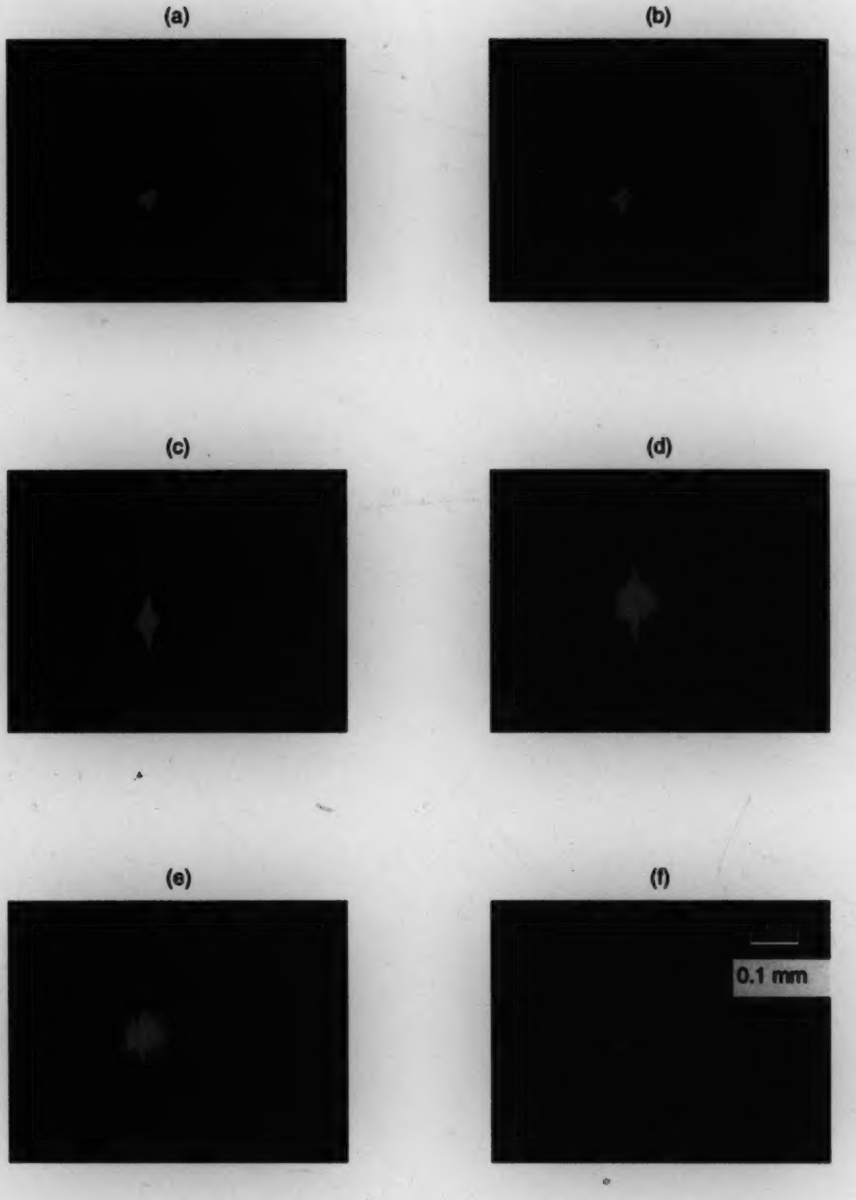

Fig. 7-15 Beam spots at the exit of the gas jet for nitrogen as a function of molecular gas density when the laser beam was focused at the exit of the gas jet. (a) 49, (b) 32, (c) 9.7, (d)8.1, (e) 3.1 times 10^{19} cm^{-3}, and (f) 10x attenuated in vacuum.

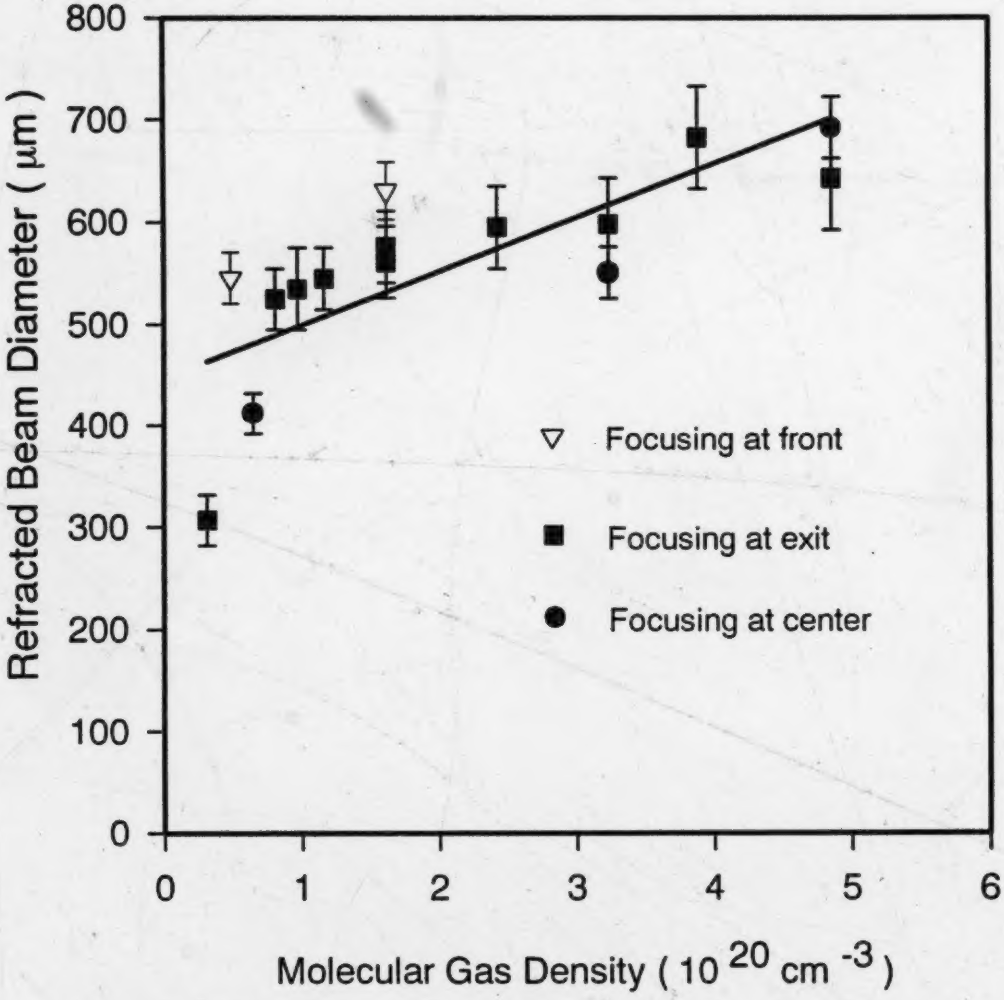

Fig. 7-16 Refractive beam diameter as a function of molecular density for nitrogen when imaging at exit. ▽ focusing at front, ■ focusing at exit, and, ● focusing at center.

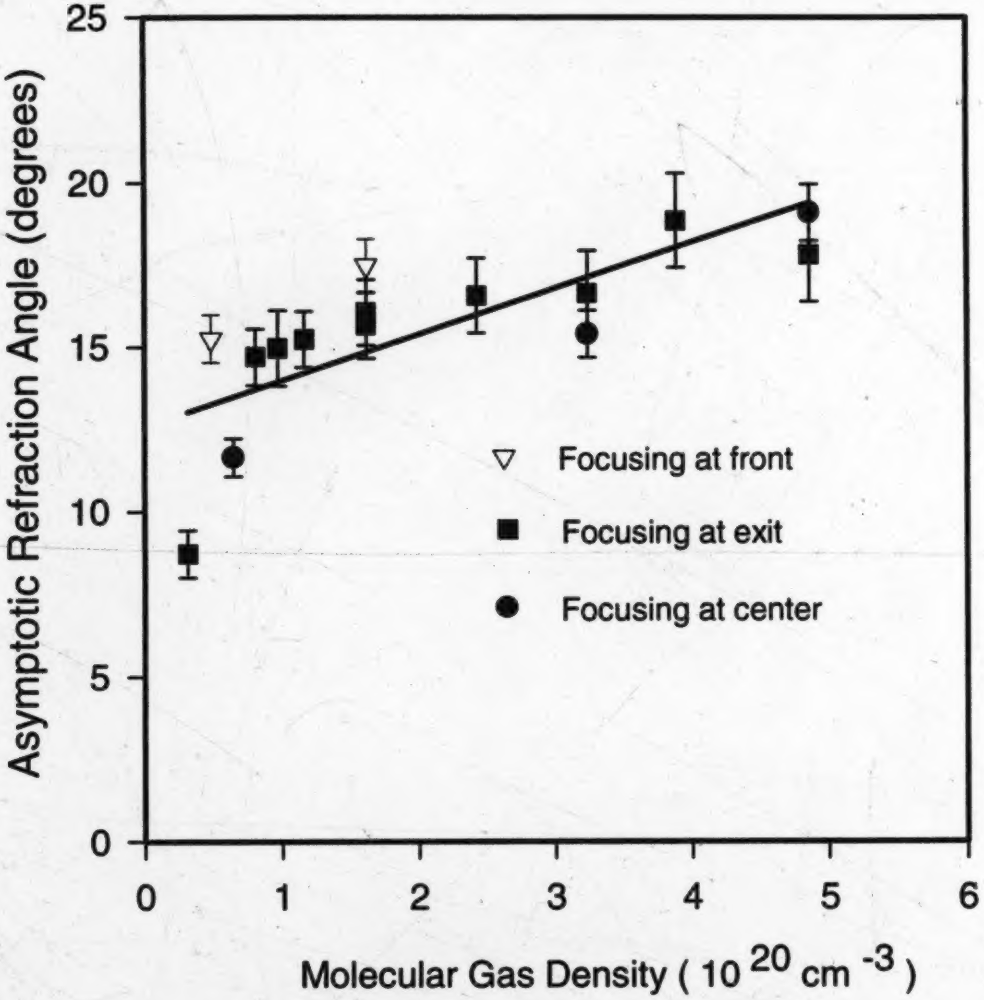

Fig. 7-17 Asymptotic refraction angle as a function of density for nitrogen when imaged at exit. ▽ focusing at front, ■ focusing at exit, and ● focusing at center.

Fig. 7-18 Plasma channel in helium of density of 4.9 x 10 ^{20} cm $^{-3}$ imaged by He II line emission at 468.5 nm (bottom image) and the corresponding UV laser light side scattering (top image) for a laser pulse of peak intensity of 1x 10 ^{17} W/cm^2 with a clean pulse. The two images have the same dimensions. For each image the horizontal and vertical dimensions are identical.

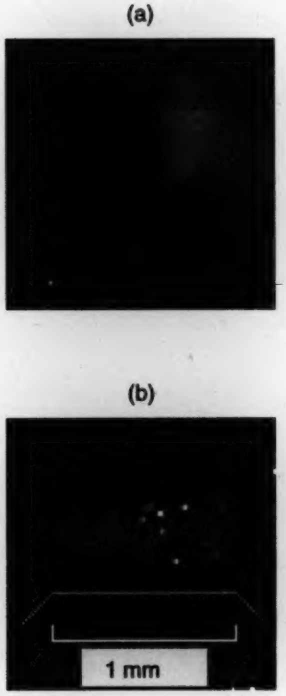

Fig. 7-19 Plasma channel in helium of atomic density of 4.9×10^{20} cm^{-3} imaged by He II line emission at 468.5 nm (bottom image) and the corresponding UV laser light side scattering (top image) for a laser pulse of peak intensity of 1×10^{17} W/cm^2 with a prepulse of 18% of energy of the main pulse. The two images have the same dimensions. For each image the horizontal and vertical dimensions are identical.

Fig. 7-20. Plasma channel in helium of density of 4.9×10^{20} cm^{-3} imaged by He II line at 468.5 nm (bottom image) and the corresponding UV laser light side scattering (top image) for a laser pulse of peak intensity of 1×10^{17} W/cm^2 with an ASE prepulse of 35% of energy of the main pulse. The two images have the same dimensions. For each image the horizontal and vertical dimensions are identical.

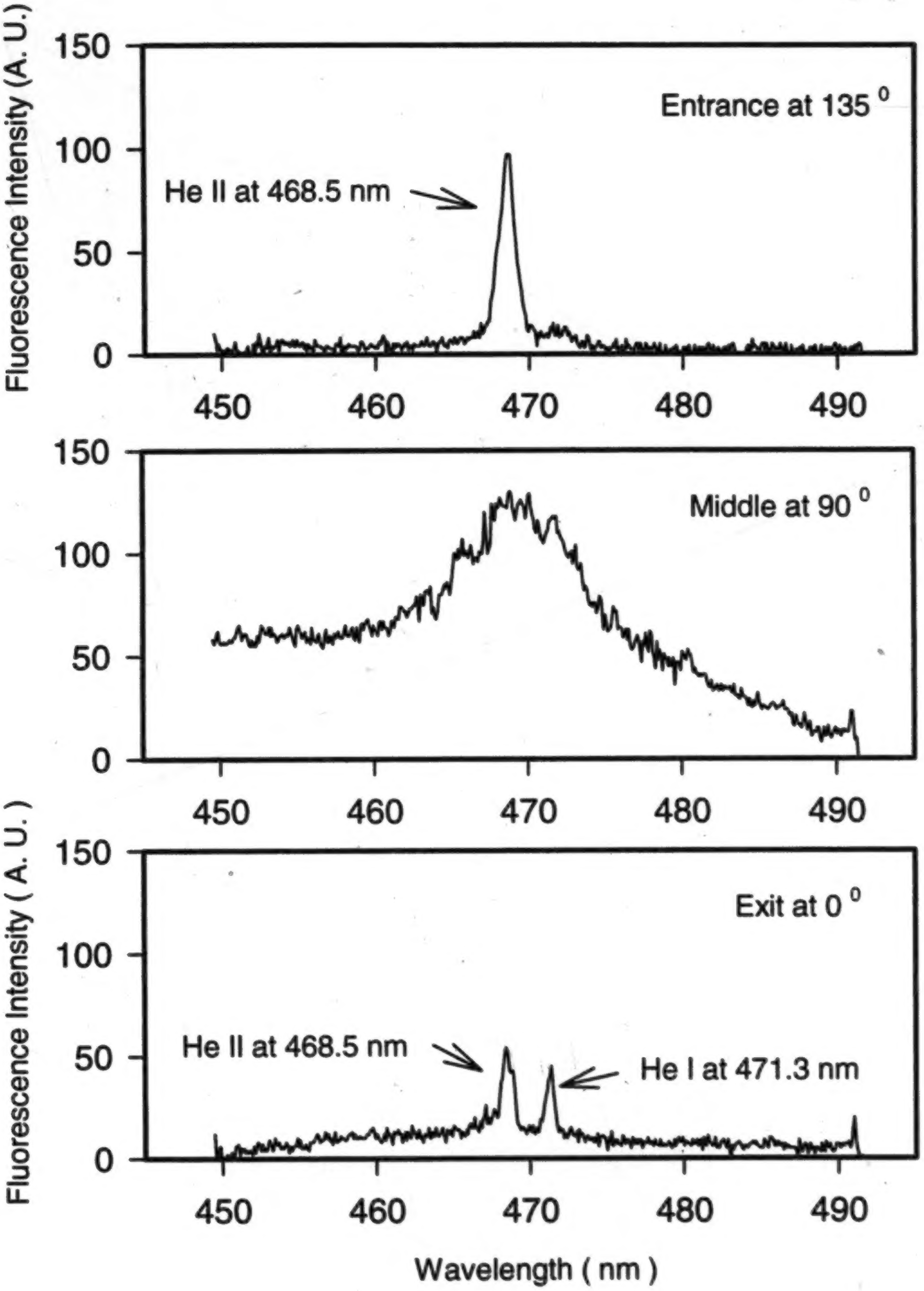

Fig. 7-21 He II emission spectra at 135, 90, and 0 degrees with a density of 4.9×10^{20} cm^{-3} for an intensity of 1×10^{17} W/cm^2 imaged at the entrance, center, and exit of the gas jet respectively.

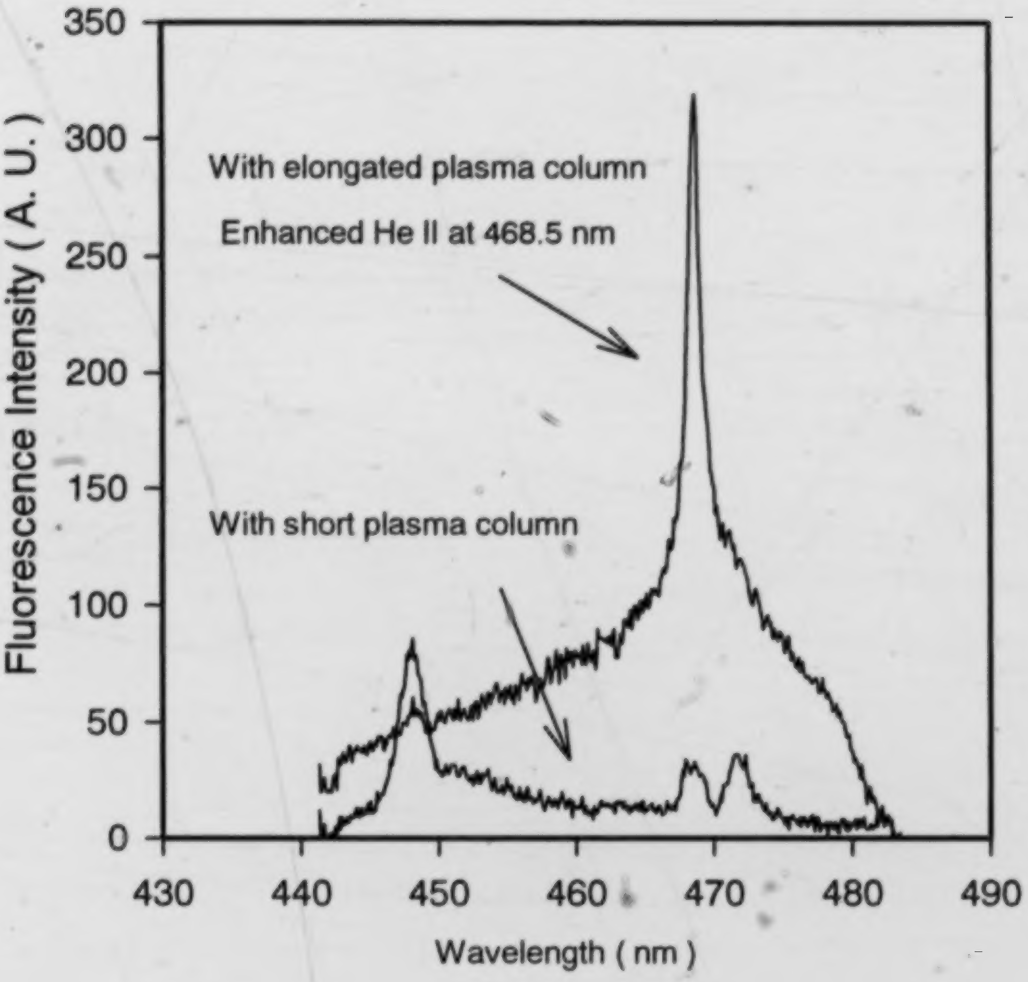

Fig. 7-22 He II spectra at the exit of the gas jet viewed at 0 degree. Enhanced He II at 468.5 nm with elongated plasma column vs. weak He II emission and He I emission (at 471.3 nm) with short plasma column at density of 4.9×10^{20} cm^{-3} and intensity of 1×10^{17} W/cm^2.

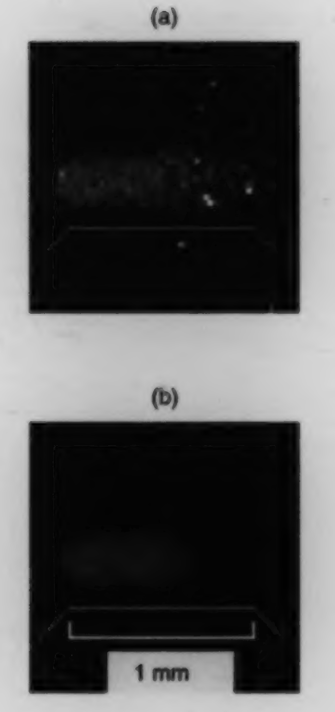

Fig. 7-23. Plasma channels in helium at density of 4.9×10^{20} cm $^{-3}$ corresponding to the two spectra in Fig. 7-22. The top (a) and bottom (b) images have ASE prepulses of 35% and 20% of energy of the main pulse.

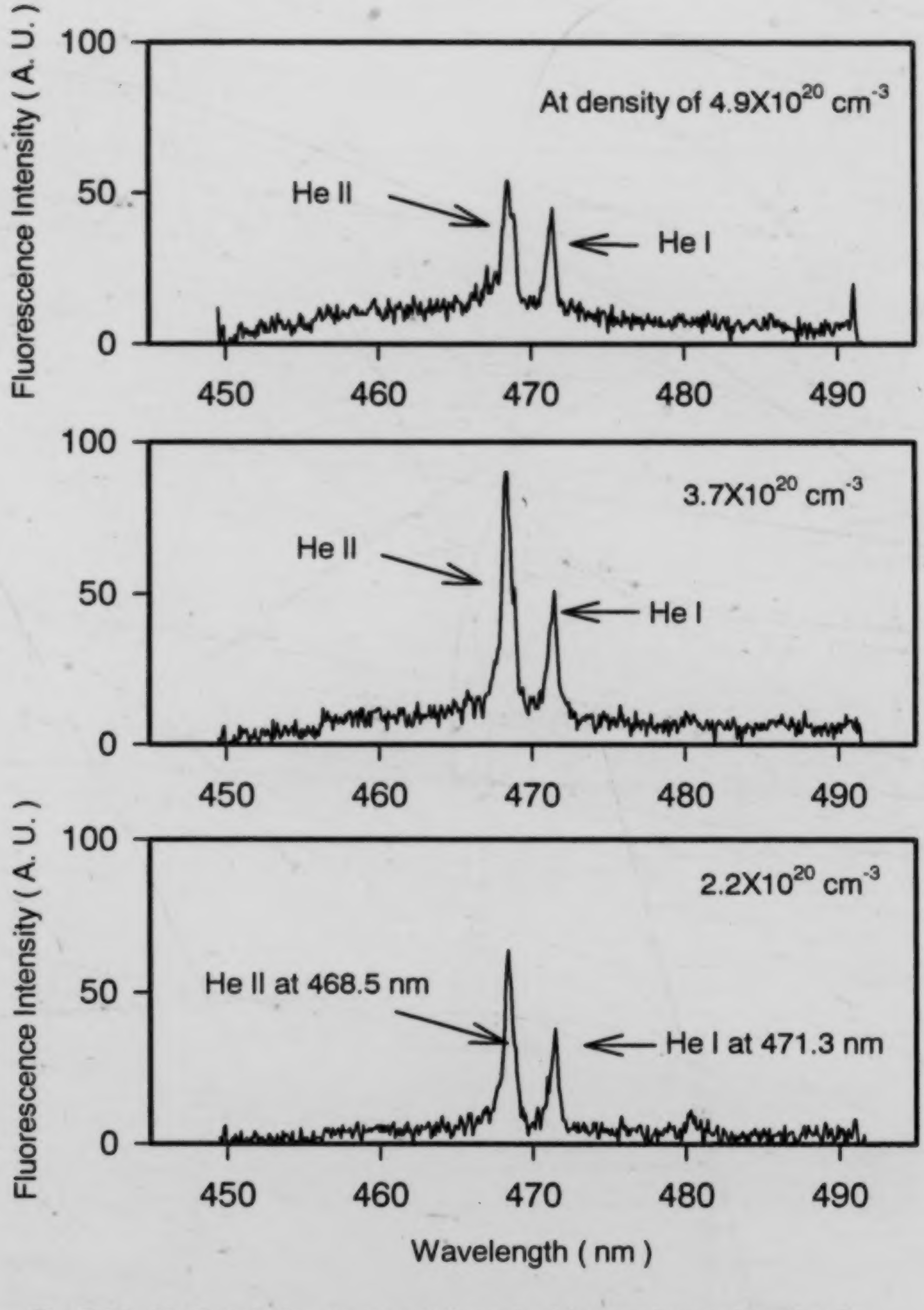

Fig. 7-24 He II emission spectra at the exit of the gas jet as viewed at 0 degrees at densities of 4.9 x 10 ^{20} cm^{-3}, 3.7 x 10 ^{20} cm^{-3}, and 2.2 x 10^{20} cm^{-3} for an intensity of 1 x 10 ^{17} W/cm^{2}.

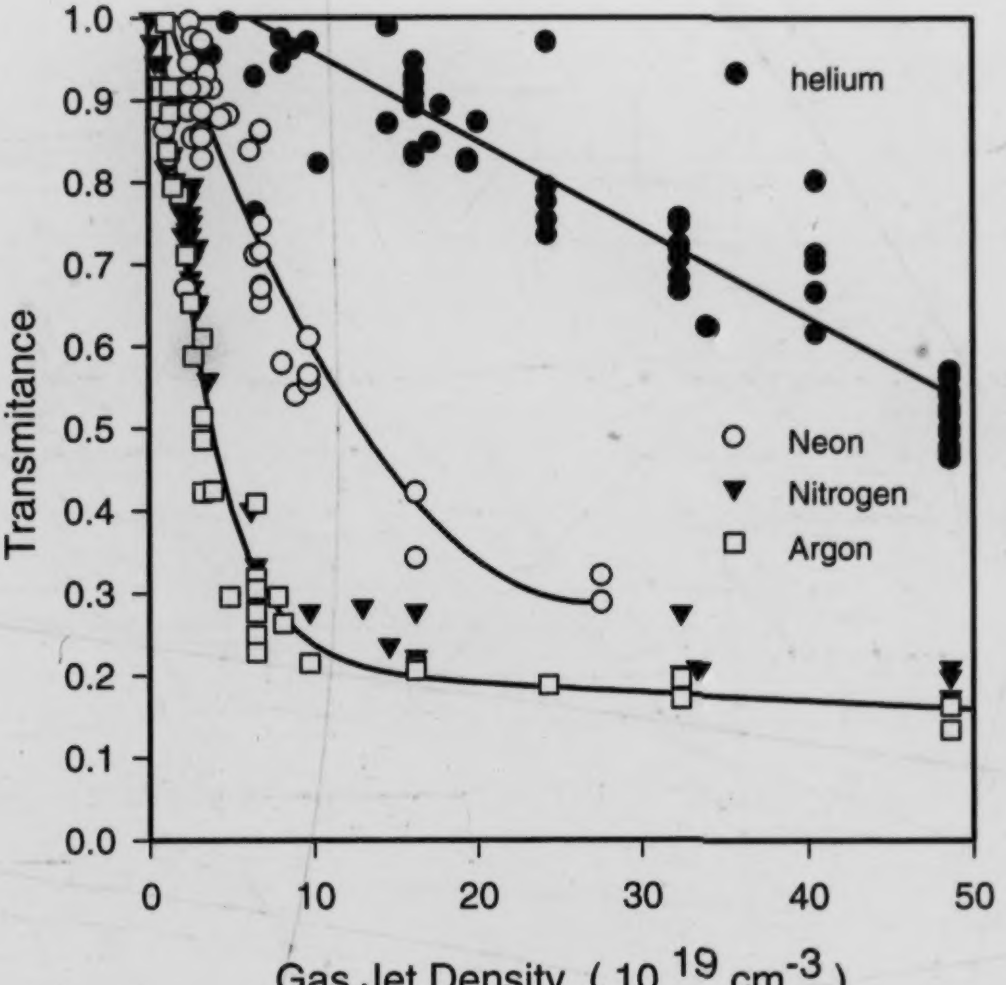

Fig. 7-25 Energy transmission of KrF laser pulses through He, Ne, N_2, and Ar into an f/2.5 cone angle as a function of density. Note that it is molecular density for N_2.

Chapter 8

Ionization Induced Blue-shift of KrF Laser Pulse in Underdense Plasma

8.1 Introduction

Spectral blueshifting from rapidly ionizing plasma was initially studied [1] using a nanosecond CO_2 laser incident on static gas cell in the early 1970s, where the dominant ionization process was collisional ionization. Picosecond and femtosecond pulses have been used more recently [2-5] to carry out measurement of spectral blueshifting in rare gas targets in a totally new regime where the ionization mechanism is rapid optical field induced ionization resulting from high field intensity. Due to the extremely high ionization rate, optical field induced ionization can produce a rapidly changing plasma front, where the rapid creation of free electrons causes a sudden decrease of the refractive index. Since the recombination time of the electrons in the plasma is much longer than the pulse width of the laser, the electron density increases monotonically throughout the laser pulse. This leads to blue-shifted components in the transmitted spectra. Theoretical modeling and computer simulations can be used to interpret the plasma dynamics [6] based on the resultant spectrum. Detailed blue-shifted spectra reported in the past have revealed multi-peak structures, which were attributed to interference effects between components of the spectrum which were created at different times during the laser pulse [4].

The previous studies were all carried out in static gas cells for pressures up to 30 atm. The defocusing of the laser beam from the breakdown plasma created led to some difficulty in achieving extremely high intensities although vacuum intensities of 10^{13} -10^{16} W/cm^2 were used. In order to match the theoretically calculated spectra with experimentally observed spectra, peak intensities of 5 to 10 times lower than the vacuum focus intensities were required [6].

In this chapter, the blue-shifted spectra of three rare gases (helium, neon, and argon) and nitrogen irradiated by one picosecond duration KrF laser pulses at 248.5 nm with vacuum focal intensities of ~ 10^{17} W/cm ^{2} are presented. One unique feature of the present study as compared to previous studies is that the laser pulse is focused onto a gas jet target rather than into a static gas cell, so that refraction can be reduced and higher intensity can be achieved. The dependence of the spectral shifts and lineshapes on the gas density was studied and comparisons were drawn among various gases. The spatial dependence of the spectra was also studied. The blue-shifted spectra are directly related to the ionization dynamics, which can be used to test theoretical models of optical field induced ionization. The spatial distribution of the transmitted beam and its blue-shifted component attests to the refraction and scattering of the input laser beam which occur at higher gas pressures.

8.2 Experimental Setup

The experimental setup for measurement of the transmitted KrF spectra is shown in Fig.8-1. With an aspheric doublet lens of 20 cm in focal length, a focal spot of 18 μm in diameter was measured. This leads to a laser intensity of 8 x 10 ^{16} W/cm ^{2} at an energy of 200 mJ for a pulse duration of 1 ps. The KrF laser radiation was normally focused at the center of the gas jet. The transmitted and forward scattered KrF light into a cone of solid angle of 0.142 steradians was collected by a UV triplet lens with a focal length of 12.5 cm. The light entered and exited the chamber via CaF_2 windows to minimize any additional absorption and self-phase modulation. The transmitted beam was further attenuated using beam splitter BS4. The part of the beam reflected off BS4 impinged on a diffuser to average the radiation over the beam profile. The optical fiber lying behind the diffuser directs the radiation to the entrance of an Ebert monochromator which has a grating of 2880 lines/mm and focusing mirror of 586 mm focal length. The resolved spectra was recorded using an optical multichannel analyzer (OMA). The overall system had a resolution of 0.08 nm.

To accurately compare the transmitted light with the input, a sample of the input beam from a beam splitter was also fed into the same monochromator by an optical fiber. This reference beam and the transmitted beam were separated spatially along the vertical entrance slit. The monochromator formed an image of two corresponding source points giving two bands of spectra on the OMA detector vertically separated in the same manner as input. The two spectra were recorded simultaneously for each shot. Thus the spectral shift can be unambiguously registered. When no gas jet was employed, i.e. shots in vacuum, there was no measurable change in the output pulse spectrum caused by self-phase modulation or other effects along the path of the transmitted beam.

8.3 Experimental Results

The dependence of the ionization induced buleshift in the transmitted spectrum in helium on gas density at a vacuum laser intensity of 8×10^{16} W/cm^2 is shown in Fig. 8-2. The intensity scale is in arbitrary units but the relative number of counts is meaningful between the various spectra. It can be seen that at a low atomic density of 3.2×10^{19} cm^{-3} a slight shoulder emerges on the blue side of the pulse. As the density increases, a distinct peak is formed at densities of the order of 6.5×10^{19} cm^{-3}, which is blueshifted by 0.54 nm from the center of the input beam. At the same time, the transmitted main pulse is slightly blueshifted by ~ 0.06 nm and the height of the main pulse is reduced as expected since the energy is channeled into the blueshifted spectral band. As the gas density is increased even further, the peak starts breaking up into a long modulated shoulder shifting towards shorter wavelength. In addition, the main peak at λ_0 becomes smaller and smaller.

The transmitted spectra for neon, nitrogen, and argon are shown in Figs. 8-3, 4 and 5 respectively. The overall dependence of the blueshifted spectra is similar to that for helium. However, there are some differences. First, for higher Z species which are ionized to higher levels, it needs less gas density to produce the same density of electrons and give a comparable blueshift. Thus, lower and lower densities are needed in terms of neon, nitrogen (two atoms for each N_2 molecule) and argon. Second, the blue shifted part is always spectrally connected with the main pulse rather than a separated peak as for helium. Third, there is a significant amount of fine structure appearing, which has not been seen in the previously reported investigations. This is attributed to the use of a gas jet enabling higher intensity at the entrance to the plasma which is significantly different from the previous experiments [2,4,5].

It is worth noting that none of the spectra in Fig. 8-2 to Fig. 8-5 shows a significant degree of red shifting, as opposed to most experiments on supercontinuum generation in solids, liquids, and gases which show both red and blue shifted components but with the red shifted component being more pronounced [7]. In this respect, the present experimental results deal mainly with the effects of ionization dynamics during the plasma formation rather than the nonlinear response of the neutral medium.

To investigate the spatial distribution of the blue shifted spectra, a stop with the same size as the laser beam was placed in the beam path before BS4 such that the original beam path was totally blocked. The light which passed around the stop was that which had been refracted and forward scattered by the plasma. With this block in place, the measured blue shifted spectra of helium are shown in Fig. 8-6 for different gas densities. The bottom curve is a vacuum shot without the stop in place but with 10 times attenuation. The next curve up is the scattered light signal with the block in place and no gas present. With gas density up to 8.7×10^{19} cm^{-3}, there is predominantly light at the original wavelength but no significant blue shifted spectra. In comparison with the blue shifted spectra obtained without the block in Fig. 8-2, the blue shifted component of the spectrum for density $< 8.7 \times 10^{19}$ cm^{-3} is mainly confined to the original beam path and thus blocked by the stop. The primary component of the spectra measured is the refracted part of the non-frequency-shifted beam. With increasing density, strong blue shifted spectral bands appear as shown in the top three curves in Fig. 8-6. Upon reaching the highest atomic density of 5.22×10^{20} cm^{-3}, the intensity of the central peak is reduced to a comparable level as the adjacent blue shifted spectral band resulting in a broad spectrum with shifted centroid. In Fig. 8-7, similar spectra were observed for nitrogen but with onset of the phenomena at lower densities, as expected. However, with densities higher than 3.8×10^{19} cm^{-3} the blue shifted spectra keeps spreading to shorter wavelength leading to weaker and weaker spectral intensity in the range of 246 to 248 nm and the blueshifted spectra has almost disappeared as one approaches the highest density of 5.2×10^{20} cm^{-3}.

8.4 Discussion

A homogeneous model can be used to make a simple estimate of the blue shifts .

For a homogeneous plasma produced by monochromatic laser light of wavelength λ_0, under the assumption that $N_e << N_{cr}$, the spectral shift is given by [6]

$$\Delta\lambda = -1.25 \times 10^{-13} \frac{e^2 N_i \lambda_0^3 L}{8\pi^2 \; m_e \, c^3} \frac{dZ}{dt} \qquad (1)$$

where N_i is the ion density, Z is the degree of ionization, L is the interaction length. λ_0 is in units of nm and the rest of the constants have their usual meaning in cgs units. It is clear that the shift is very much dependent on the ionization rate. In the present experimental conditions for helium (Fig. 8-2), with $N_i = 6.5 \times 10^{19}$ cm^{-3}, L=0.4 mm, we have $\Delta\lambda = 0.59 - 5.9$ nm assuming that $dZ/dt = 10^{12}$-$10^{13} s^{-1}$. The measured shift of the second peak is 0.54 nm to the blue, consistent with an average ionization rate of $10^{12} s^{-1}$.

The ionization induced blue shift has been numerically simulated in terms of a one dimensional electromagnetic propagation model [6]. Since the blue shifting is associated with the instantaneous action of ionization in the wavefront, the spatial intensity profiles of the laser beam, either initial or in the course of ionization, will affect the resultant spectra.

For a beam with a transverse intensity beam profile, the nonuniformity can cause two kinds of effects. First, it will induce different shifts across the beam front since the multiphoton ionization rate is nonlinearly dependent on the laser intensity. Secondly, it causes refraction of the laser beam itself as evidenced in this experiment (Fig. 8-6) and the recent numerical studies by Rankin et al. [8], Leemans et al.[9], and Rae [10]. This refraction will in turn alter the beam profile. Previous studies have all been done in gas cells with pressures up to 30 atm [4]. In Ref. 2, a significant amount of defocusing was found and the actual intensity may have been reduced 10 times [6]. Other experiments [2-5] using large f number optics (> f/8) and lower intensities of 10^{14-15} W/cm^2 have revealed multi-peaks on the shoulder of the blue shifted spectra. These are attributed to the interference effects in the spectrum when the frequency shift occurs several times during the laser pulse [4]. Simulations have compared well to these experimental results. However, in the present experiment, much higher laser intensities prevail in the gas jet target because of the significant reduction in defocusing. A second peak for helium at a density of 6.5×10^{19} cm^{-3} was revealed which was not seen before. Even with the present gas jet system, the transmitted laser beam has undergone some degree of refraction as shown in Fig. 8-6. In this case, the refracted beam is still intense enough to ionize the gas along its diverging path and causes a blue shift. Thus refraction is important in modeling the ionization dynamics. A calculation of the expected ionization induced blue shift including the refraction effect will be presented in the next chapter.

In summary, the blue shifted spectra for helium, neon, argon, and nitrogen have been measured at various pressures for KrF laser irradiation at a vacuum intensity of 8×10^{16} W/cm^2. A gas jet target was used in this experiment to minimize refraction of the laser beam and thus realize higher laser intensities. For helium, a distinct second peak was revealed which was not seen before and is attributed to the high intensities achieved in the present gas jet target. At lower densities, the blue shifted spectra were confined mainly to the original beam path. As the pressure increases, the laser beam was refracted and the refracted beam also exhibited a blue shifting along its diverging beam path. The refraction of the laser beam is important in the correct interpretation of the observed blue shifted spectra.

References

1. E. Yablonovitch, Phys. Rev. Lett. 31, 877 (1973).
2. W. M. Wood, C. W. Siders, and M. C. Downer, Opt. Lett. 13, 984 (1988).
3. W. M. Wood, C. W. Siders, and M. C. Downer, Phys. Rev. Lett. 67, 3523(1991).
4. S. P. Le Blanc and R. Sauerbrey, S. C. Rae and K. Burnett, J. Opt. Soc. Am. B 10, 1801, (1993).
5. M. Ciarrocca, J. P. Marangos, D. D. Burgess, M. H. R. Hutchinson, R. A. Smith, S. C. Rae, Opt. Comm. 110, 425 (1994).
6. S. C. Rae and K. Burnett, Phys. Rev. A 46, 1084 (1992).
7. P. B. Corkum and C. Rolland, IEEE J. Quantum. Electron. 25, 2634 (1989).
8. R. Rankin, C. E. Capjack, N. H. Burnett, and P. B. Corkum, Opt. Lett. 16, 835 (1991).
9. W. P. Leemans, C. E. Clayton, W. B. Mori, K. A. Marsh, P. K. Kaw, A. Dyson, and C. Joshi, Phys. Rev. A 46, 1091 (1992).
10 S. C. Rae, Opt. Comm. 104, 330 (1994).
11. N. Bloembergen, Opt. Comm. 8, 285(1973).

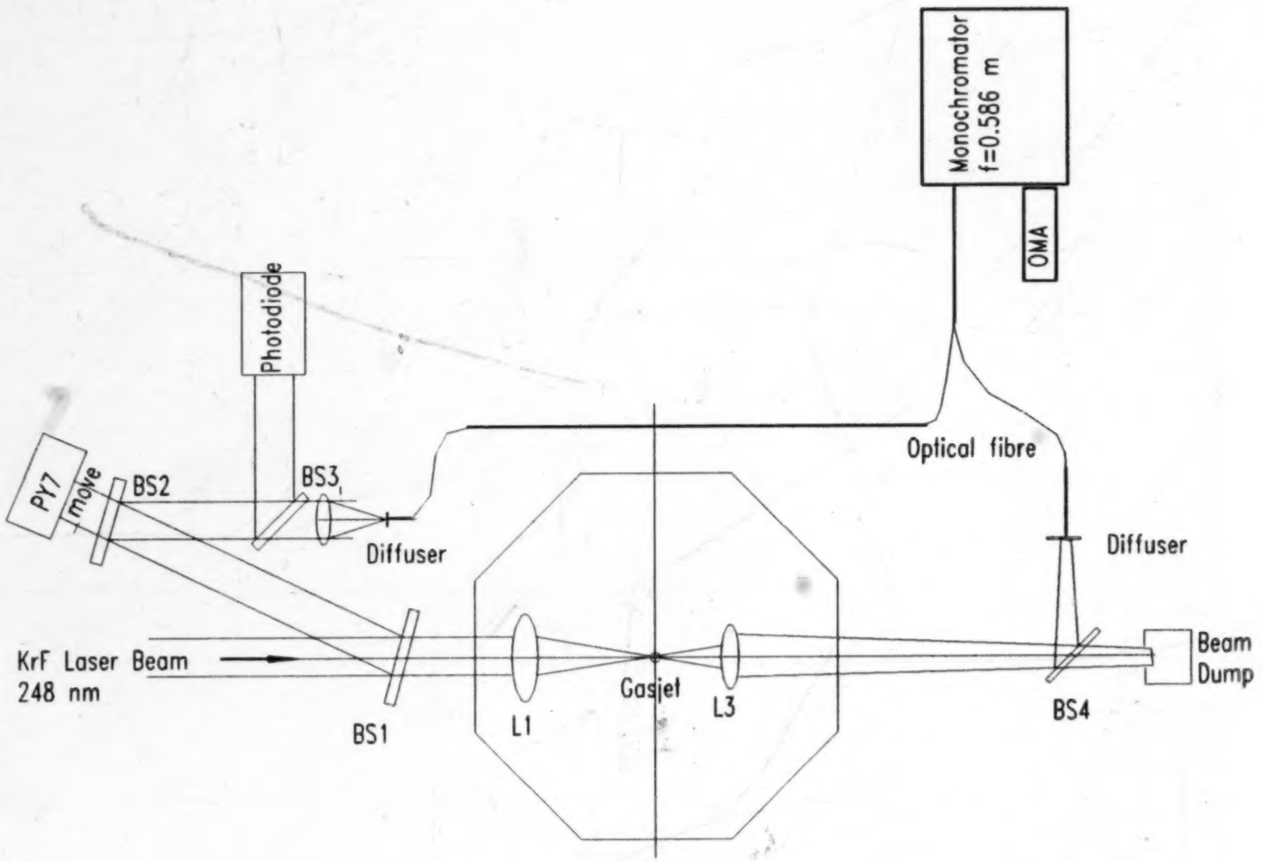
Monochromator
f=0.586 m
OMA
Photodiode
PY7
move
BS2
BS3
Optical fibre
Diffuser
Diffuser
KrF Laser Beam
248 nm
BS1
L1
Gasjet
L3
BS4
Beam
Dump

Fig. 8-1 Experimental setup for blueshift measurement

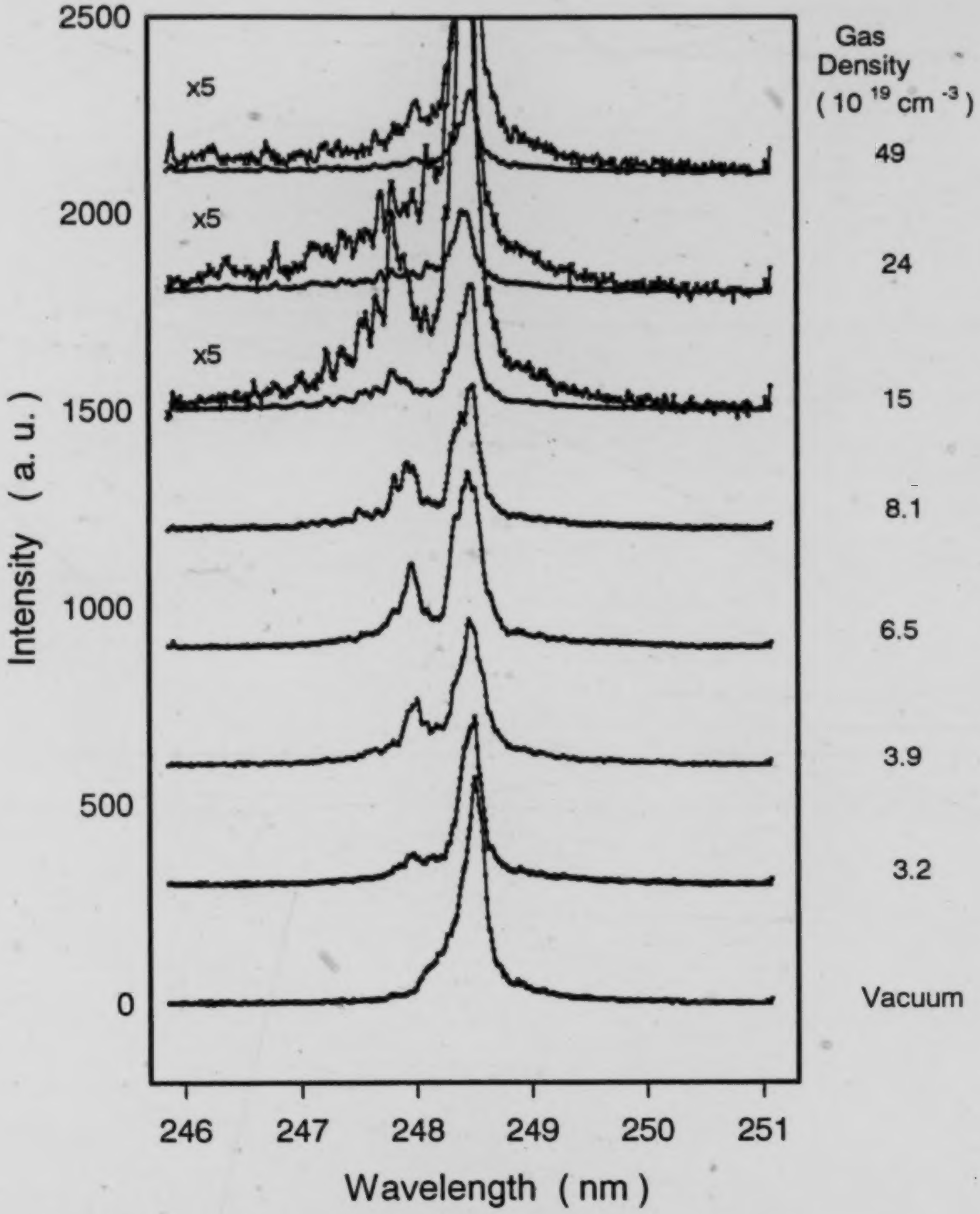

Fig. 8-2 Blue shifted spectra in He as a function of gas density at a vacuum intensity of 8×10^{16} W/cm^2. The top three plots also show 5 times magnified curves of each.

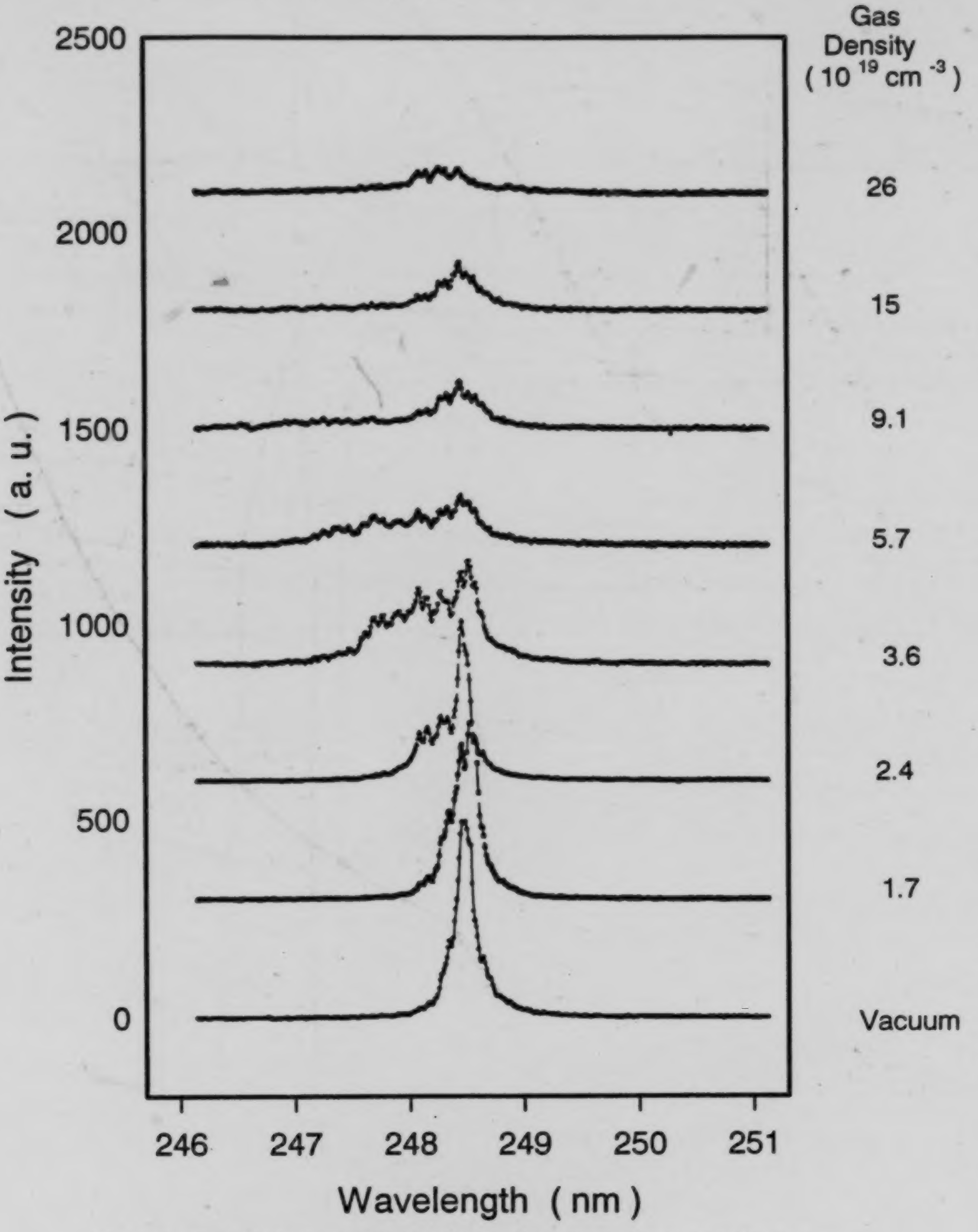

Fig. 8-3 Blue shifted spectra for Ne as a function of gas density at a vacuum intensity of $8x10^{16}$ W/cm^2 .

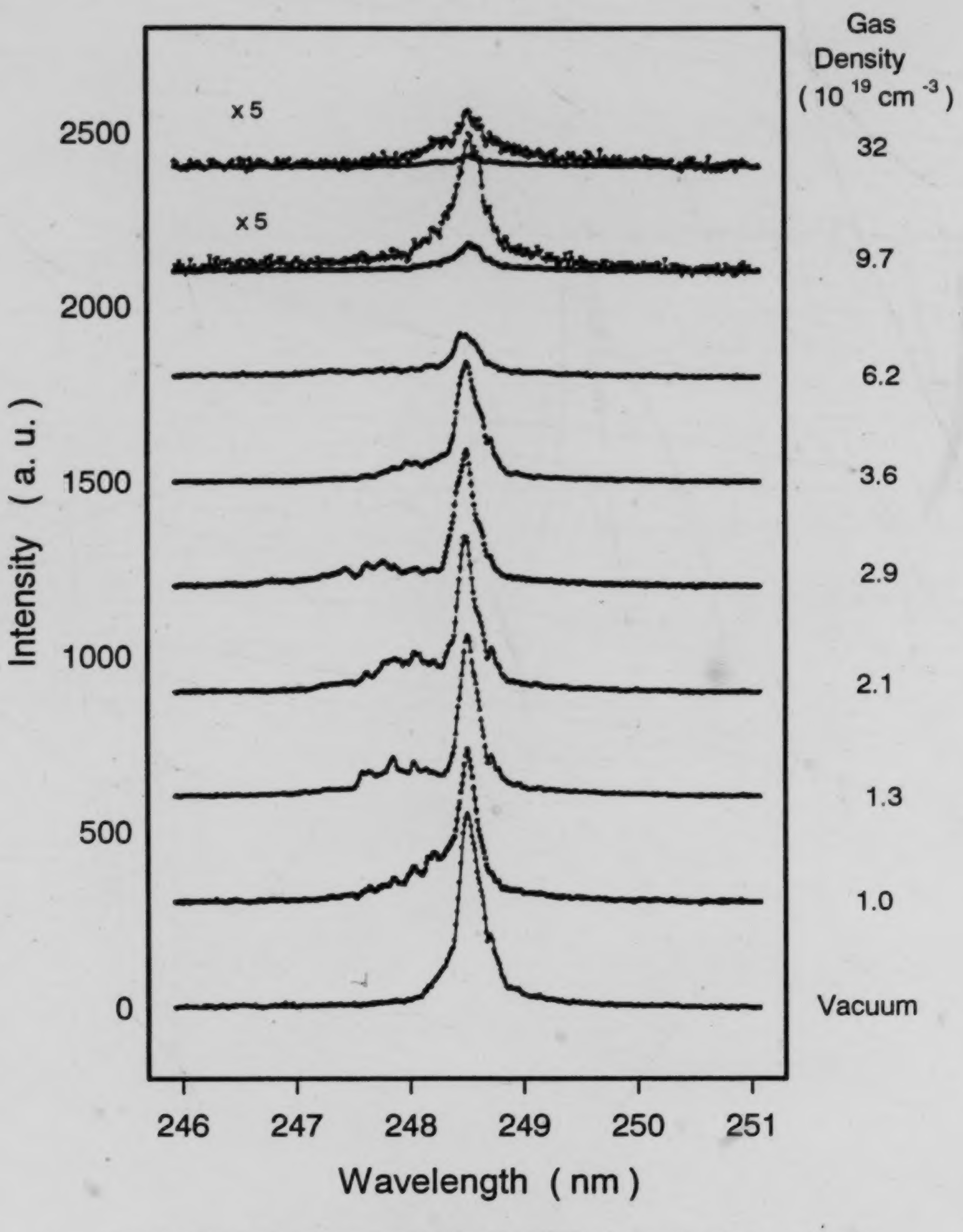

Fig. 8-4 Blue shifted spectra for N_2 as a function of molecular gas density at a vacuum intensity of 8×10^{16} W/cm^2. The top two plots also show 5 times magnified curves of each.

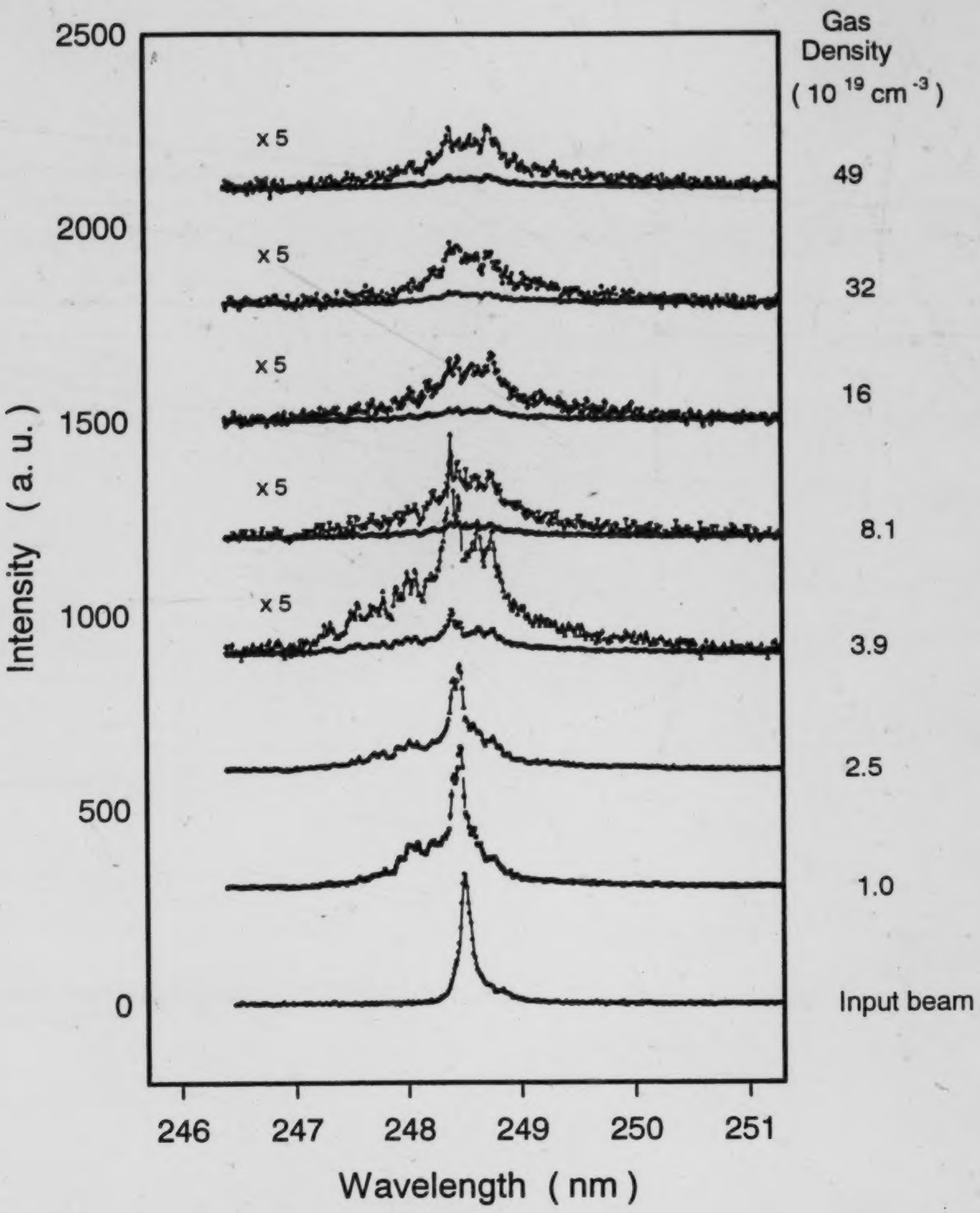

Fig. 8-5 Blue shifted spectra for Ar as a function of density at a vacuum intensity of 8×10^{16} W/cm^2. The top five curves also show their 5 times magnified curves of each.

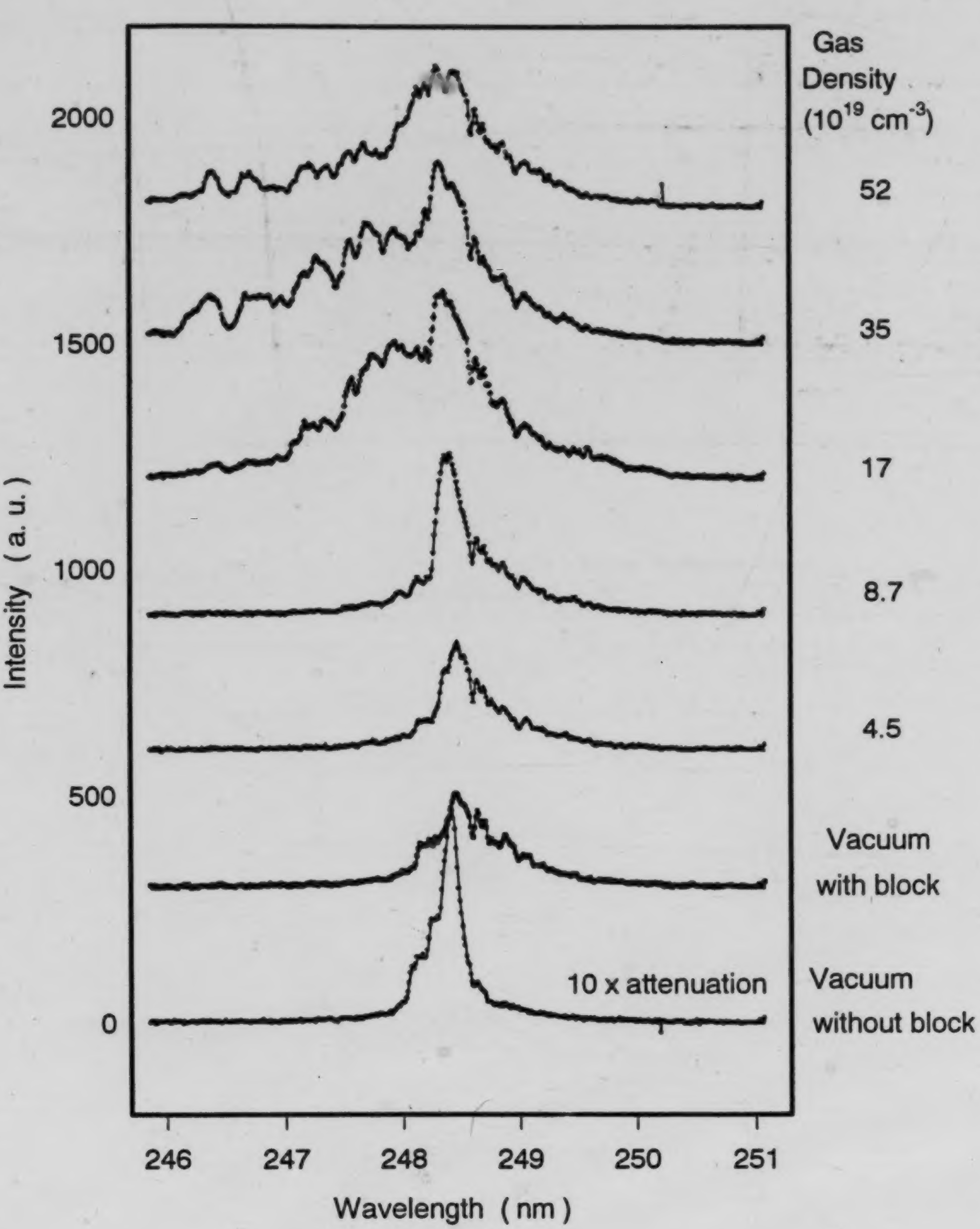

Fig. 8-6 Blue shifted spectra with a beam stop for He as a function of density at a vacuum intensity of $8x10^{16}$ W/cm^2. The bottom curve is 10 times attenuated.

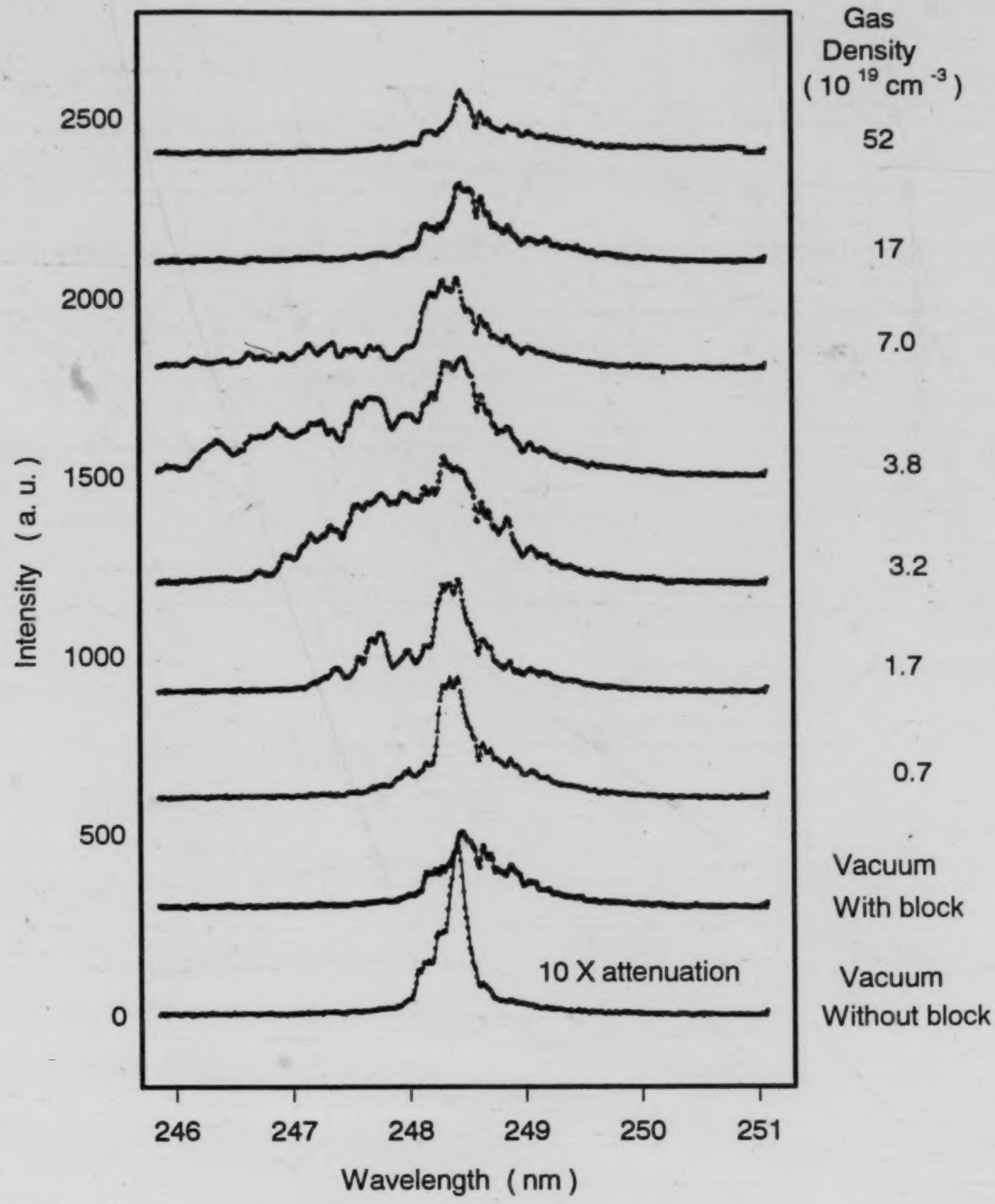

Fig. 8-7 Blue shifted spectra with a beam stop for N_2 as a function of molecular density at a vacuum intensity of $8x10^{16}$ W/cm^2.

Chapter 9

Numerical Modeling Calculations

9.1 Refraction

A simple analysis of refraction due to the electron density dependent refractive index in ATI produced plasmas can be carried out using the equations describing the paraxial propagation of Gaussian beams in a lens like medium. Such an analysis has recently been published by Fill [1] which we will follow here.

The transverse beam profile is assumed to be Gaussian with an intensity given by $I = I_0 \exp\left(-r^2/r_0^2\right)$ and a total power given by $P = I_0 \pi r_0^2$. The refractive index is approximated by its quadratic dependence (found from a power law expansion of the full profile) on axis given by

$$n(r,z) = n_0 - \left(\tfrac{1}{2}\right) n_2 r^2 \qquad (9.1)$$

The propagation of a ray along z at a distance r from the beam axis is then given by the equation

$$\frac{d^2 r}{dz^2} = -\frac{n_2}{n_0} r + \frac{\lambda^2}{4\pi^2} \frac{r}{r_0^4} \qquad (9.2)$$

In order to proceed further the degree of ionization and resultant refractive index profile must be related to the intensity. The intensity threshold for ionization to a charge state of q can be given by [2-4]

$$I_{th,q} = 4 \times 10^9 \frac{1}{q^2} U_q^4 \qquad (9.3)$$

where U_q is the ionization potential in eV. While the real ionization proceeds in discrete steps, for the present analysis we assume that the ionization potential is a continuous function of q given by a power law expression of

$$U(q) = \tilde{U}\, q^{\alpha} \qquad (9.4)$$

and that the local charge state, q, is related to the intensity by Eqns. 9.3 and 9.4. Doing so gives the charge state distribution across the beam

$$q = q_0\, I^{1/(4\alpha-2)} \qquad (9.5)$$

where

$$q_0 = 1\Big/\left(4 \times 10^9\, \tilde{U}^4\right)^{1/(4\alpha-2)} \qquad (9.6)$$

using a quadratic fit to the electron density profile given by Eqn. 9.5 and the Gaussian intensity profile the radially dependent refractive index term n_2 can be calculated. Using this result in Eqn. 9.2 and evaluating the ray trajectory for the 1/e intensity point at $r=r_0$ gives the propagation equation

$$\frac{d^2 r_0}{dz^2} = \frac{\tilde{n}_2}{4\alpha - 2} \frac{1}{r_0^{(2\alpha/(2\alpha-1))}} + \frac{\lambda^2}{4\pi^2 r_0^3} \qquad (9.7)$$

where

$$\tilde{n}_2 = q_0\left(\frac{N_a}{N_c}\right)\left(\frac{P}{\pi}\right)^{\frac{1}{4\alpha-2}} \tag{9.8}$$

and where N_a is the atomic gas density and N_c is the critical density. The second term in Eqn.9.7 describes the normal self diffraction of a Gaussian beam and the wavelength λ can be artificially chosen to give a match to the measured focal spot diameter for a given (non diffraction limited) laser beam. Eqn. 9.7 is solved numerically in Matlab using a 4th order Runge-Kutta technique for the ray propagation through the gas jet target.

In order to proceed, power law functions as given by Eqn. 9.4 are fit to the ionization potentials of the elements of interest here. Only the outer shell electrons are considered in this fit since ionization usually only occurs for these electrons. In addition, the step function to the next set of ionization potentials is quite large and would not be well described by Eqn. 9.4. In order to give more weighting to the first few ionization potentials which dominate the refraction process a least squares fit is carried out to the log of the ionization potentials rather than the ionization potentials themselves. The resultant parameters are given in Table 9.1 for the gases of interest.

A sample calculation for a peak power of P=0.2 TW in nitrogen gas using our measured gas jet density profile and an F/4.2 focal cone is given in Fig. 9-1. In vacuum the input beam would reach a focal spot of 9 μm radius at the axial position of z=0. It can be seen that severe refraction occurs for a peak atomic density of 5×10^{20} cm^{-3}, while even at a density of

Table 9.1 parameters of a power law fit to the ionization potentials of the outer shell electrons for the various gases.

Gas	$\tilde{U}$ (eV)	α
He	24.6	1.145
N	13.7	1.202
Ne	19.4	1.180
Ar	14.0	1.073

1×10^{20} cm^{-3} the focal spot radius is 22.7 μm reducing the peak focal spot intensity by a factor of 6.4 times compared to its vacuum value. The calculated peak intensities achieved when the vacuum focus is at the center of the gas jet target are plotted as a function of gas jet density in Fig. 9.2. Also shown for comparison are the peak intensities which could be achieved in a static gas target of the same peak density. As can be seen the peak intensities in the gas jet targets are much higher than could be achieved in a static gas target for densities above a few times 10^{19} cm^{-3}. Of course, less refraction and higher intensities can be achieved by using even smaller diameter gas jet targets or by focusing in the leading edge of the gas jet at the expense of obtaining a shorter interaction length.

The predicted beam diameter at the gas jet exit, z=500 μm, can be compared to the measured beam diameters for helium and nitrogen and are shown in Fig 9.3. It can be seen that the predicted diameters are smaller than the measured values for the outer refraction spot diameter for helium but agree reasonably for nitrogen. However, it must be remembered that the present model assumes a homogeneous instantaneous ionization process. The real ionization process proceeds in a stepwise fashion in the leading edge of the pulse only. Using a full time dependent calculation of the above threshold ionization process, to be described in the next section, the effective charge state of a nitrogen plasma, as seen in the frame of reference of the propagating laser pulse, is shown in Fig 9.4(a). The average charge state of the plasma given by Eqn. 9.5 is also plotted for nitrogen gas in Fig. 9.4 (b). It can be seen that the real ATI ionization profile will lead to stronger refraction of parts of the leading edge of the pulse in the rapidly ionizing regions than predicted by the above model. At the same time, the tail of the laser pulse propagates in a uniformly ionized plasma region and should experience a much lower degree of refraction. The strong refraction at the leading edge of the pulse will cause an erosion of the leading edge which will slowly work its way through the pulse. Thus it is expected that the leading edge of the pulse undergoes strong refraction leading to somewhat larger beam spots than predicted by the above simple model while the tail of the pulse may still focus to a smaller beam spot than predicted by the above model. This could explain the observed larger outer refraction spots together with the bright center spots in experimental CCD camera images given earlier.

9.2 Numerical ionization modeling code

A 1D numerical code has been written to simulate the experimental measurements of ionization blueshift and absorption. The calculation takes into account the beam intensity profile in space, the measured density profile and includes above threshold ionization, above threshold ionization heating, and inverse Bremsstrahlung heating.

The geometry of the calculation is shown in Fig. 9.5. The starting atomic density profile is given as a Gaussian with a full width at half maximum of 925 μm which gives the best fit Gaussian to the experimentally measured profile given in Fig. 7-4. The density profile is split into ndens zones of width dstepum. Typically 1000 zones of width 2 μm are chosen for the calculation giving a total simulation length of 2 mm.

The laser power is defined as a Gaussian pulse in time with a full width at half maximum given by tlasfs. The pulse is divided into nlas zones with a width of tstepfs per zone. Typically 500 zones with a width of 6.67 fs per zone are chosen. The time step per zone is chosen to match the time for the radiation to propagate one step in the spatial profile.

The intensity of the laser beam is calculated at each spatial position using a predefined beam cross-section as a function of position. This spatial dependence of beam size is chosen either as the best fit parabolic function to the experimentally measured profile given in Fig. 7-2 or the refraction beam profiles calculated in the previous section. The wavelength of each zone in the laser pulse is also stored in order to calculate the cumulative ionization induced blue shift for each local zone of the laser pulse. In this case an assumption is being made that the laser pulse is not transform limited and thus one can treat each part of the pulse distinctly. For the KrF laser pulse in the present experiment this is a reasonable assumption since it is known that KrF laser pulses produced by such DFDL dye laser front end systems are chirped and in fact can be compressed to duration on the order of 150 fs [5].

The calculation proceeds by advancing the laser pulse one step forward in the spatial profile at a time. Then the following calculations are carried out at each zone of the laser pulse or each corresponding zone of the spatial density profile.

1. The above threshold ionization for one time step is calculated using the Ammosov ionization rates given by Eqn. 2.9. The calculation is carried out using a variable step size 4th order Runge-Kutta method. The populations of all ionization levels are stored at each spatial position.
2. The ATI heating is approximated by assuming that ATI electrons are born with an average energy given by 0.15 of the ponderomotive potential of the laser beam.
3. The inverse Bremsstrahlung heating is calculated using the heating rate given by Eqn. 2.15. The high field corrections given by Eqn. 2.18 and 2.21 are also included in the heating calculation by taking whichever is the smaller of these two factors for any given time step.

4. The energy in the laser beam is reduced by the amount of energy required to heat and ionize the plasma.
5. The local time rate of change of refractive index is calculated and the corresponding incremental change in wavelength is added to each zone in the laser pulse.

After the complete laser pulse has propagated through the complete density profile the energy absorbed from the laser pulse is compared to the energy stored in the ionized plasma in order to check the conservation of energy. The spectral distribution of the output radiation is calculated by combining the spectrally shifted contributions from each laser zone weighted by the output energy of the laser zone. Various processes including ATI heating, IB heating, the high field Maxwellian correction, and the Langdon factor correction could be turned on and off using control switches iswati, iswib, iswhf, and iswla respectively. The control parameters are given in the input file b.inp while the ionization data for the desired elements in given in the file b.dat. For all the calculations presented in this section both ATI and IB heating with both the high field and Langdon correction factors were turned on.

Typical output from a calculation run for helium is shown in Figs. 9-6, 7, and 8 for a peak density of 5 x 10 ^{19} cm^{-3}, a peak laser powers of 0.025 TW and 0.25 TW and the experimental beam profile. In Fig. 9-6 the spectral blueshift for helium as a function of time is plotted against the instantaneous intensity which induces the corresponding blueshift. Fig. 9-7 shows the ionization state distribution across the gas jet after the laser beam propagates through it. Also shown in Fig. 9-7 is the calculated electron temperature. It can be seen that the peak temperatures of 75 eV and 127 eV are considerably higher than the pure ATI heating temperatures of 5.7 eV and 57 eV respectively for the peak intensities of 10^{16} W/cm^2 and 10^{17} W/cm^2 shown here. The final time integrated spectrum is shown in Fig. 9-8 together with the input spectrum. This can be compared to the measured spectra in Fig. 8-2 for helium. Note here that the lower intensity case in the above calculation utilized a laser power which was 8 times smaller than that in the present experiment and yet gives a final spectrum which is similar to that observed experimentally for this density . This is probably due to the refraction effect in the experiment which will reduce the peak intensity from its vacuum intensity as discussed in the previous section and as shown in Fig. 9-2. The lower intensity case of the present simulation can qualitatively match the experimental results for helium.

In order to understand the ionization dynamics and associated refraction effect, the beam profile through the gas jet calculated from the ionization refraction model of the previous section is used to specify the beam cross-section at each point of the gas jet. The ionization and heating code is then run to calculate the interaction with various gases at various peak densities. Figs. 9-9, 10, and 11 group together the various plots which show the evolution of the blue shifts as a function of time for low Z to high Z gases, helium, neon, nitrogen, and argon, and the corresponding ionization states. In Fig. 9-9, the set of the plots in the left column shows the instantaneous blue shifts for a laser power of 0.2 TW and pulsewidth of 1 ps at a density of $5\text{x}10^{19}$ cm^{-3} as compared to those in the right column for which a density of 5×10^{20} cm^{-3} is used. For the lower density case as in the left column it can be seen that the blue shifts occur at the leading edge of the laser pulse. Each higher ionization stage corresponds to a higher intensity point on the pulse profile and gives a peak in the blue shift as a function of time. For high Z species like argon, there are more peaks produced which show 6 times ionized argon exists. When comparing with the graphs in the right column it is interesting to note that the peaks are smeared out and the peak ionization achieved at these higher densities is less, so that a smooth increase of the blue shift as a function of time is displayed. These features can be further understood from the corresponding distribution of ionization states across the gas jet as shown in Fig. 9-10. For lower pressure case in the left column, helium can be fully ionized in the center of the gas jet and high Z species can have as many as 6 electrons being stripped. Furthermore the spatial distribution of the ionization states seems symmetrical across the gas jet with the highest ionization state being at the center of the gas jet. This is because the laser beam is not refracted or absorbed very much so that there is enough intensity to ionize the gas in the second half of the gas jet as also is evident in the power plots in Fig. 9-9. However for the high pressure case as in the right column, the highest ionization stage is three times. Contrary to the lower pressure case, the higher ionization states locate at the front of the gas jet and then lower ionization states follow consecutively into the gas jet. It always ends up with neutral gas at the end of the plotted range. This is in agreement with the He II and He I spectral measurement as shown in Fig. 7-24 where for the high density case the laser intensity decreases at the exit due to the refraction in the front of the gas jet.

Fig. 9-11 shows the time integrated blue shifted spectra. For high Z species the laser beam experiences larger shifts. As the pressure increases, the blue shifted spectra extend further towards the blue side. Qualitatively the calculated blue shifts are comparable to the measured blue shifts shown earlier in Chapter 8. However, the simulation results can not be compared to the experimental measurements in detail since the present model is limited to an average uniform beam profile when in reality we would expect different behavior in the leading and tailing edges of the pulse. Full 2D calculations would be required to fully compare to the data.

The absorption of the laser beam in the plasma is also calculated in the simulations. Two cases were calculated to compare the effect of the laser beam profile on the absorption. The first case used the symmetric portion of the experimentally measured vacuum beam profile as given in Fig. 7-2. However, the input power used was 10 times smaller than that in the experiment in order to approximately account for the expected refraction reduction in intensity. The calculated curves of transmission of KrF laser pulses through helium, neon, nitrogen and argon are shown in Fig. 9-12. Also shown in the graph are the experimental measurements from Fig. 7-25. It can be seen that for helium the calculations are in good agreement with the experimental measurements within the uncertainty of the measured data. However, for other high Z species, the calculated values of transmission are larger than the measured ones at low pressure and then become smaller at high pressure.

The second case of simulations utilized the beam profiles calculated using the refraction model presented in the previous section. The input laser power was chosen to be 0.2 TW from the experiments. Fig. 9-13 shows the computed transmission of KrF laser pulses through helium, neon, nitrogen and argon for this case. Again, there is close agreement for helium but larger differences for neon, nitrogen and argon. It is also interesting to note that the calculated values for nitrogen at densities over 2.3×10^{20} cm^{-3} approach the experimental measurements. In summary, the simulation results of absorption are in reasonable agreement with the measured data for helium in both cases. However the absorption calculations deviate from the experimental measurements for higher Z gases where refraction is stronger. In part, this is due to some refraction of laser light outside of the cone angle of the collection lens. However, this should give a discrepancy at the peak measured densities instead of the intermediate densities where the discrepancy occurs. Again, this may indicate the simple 1D model is not sufficient to interpret the experimental data and full 2D simulations including ionization and refraction are required.

An important parameter in many experiments using ATI heated plasmas is the electron temperature of the plasma. The absorption of the laser energy contributes to the rise of electron temperature in addition to providing the ionization energy. However, the temperature of the electrons is also determined by the balance between heating and conduction losses. Since the diagnostics employed here in the gas jet experiment were not designed to characterize the plasma temperature directly, the simulation results from the above 1D model will be discussed here. Fig. 9-14 shows the calculated electron temperatures for helium, neon, nitrogen and argon as a function of density using the refraction beam profile from section 9.1. The electron temperatures for the three gases all reach a peak temperature at some intermediate density and then drop off with higher density. The temperatures start out with their ATI heating values at very low density. The increase of temperature at lower densities is associated with the onset of collisional heating with increasing collision frequency in the denser plasma. The reduction of the electron temperature at higher peak densities is associated with the strong refraction which leads to the reduction of the interaction intensity.

The present model does not take into account lateral heat conduction which may be important in modifying the maximum temperatures obtained. This has already been noted in numerical simulations by Djaoui et al [6]. The following will give an estimate of the role played by lateral heat conduction. The thermal conductivity formula taken from Spitzer is [7]

$$\kappa = \varepsilon\delta_T \, 3.28 \times 10^{10} \, \frac{T_{eV}^{5/2}}{Z \ln \Lambda} \qquad \frac{\text{erg}}{\text{cm}\cdot\text{s}\cdot\text{eV}} \qquad (9.10)$$

where the correction coefficient for Z can be given by [8]

$$\varepsilon \, \delta_T \cong \frac{0.095(Z+0.24)}{1+0.24Z} \qquad (9.11)$$

The thermal diffusion coefficient is given by

$$D = \frac{\kappa}{C\rho} \quad (\text{cm}^2 / \text{s}) \qquad (9.12)$$

where C is the heat capacity and ρ is the density. The distance of propagation of a heat wave in time t can be approximated as

$$x \approx \sqrt{D\,t} \qquad (9.13)$$

The maximum diffusion lengths are given by the highest plasma temperature combined with low plasma densities. Estimates of the heat diffusion length can be made using the temperatures given in Fig. 9-14. For a fully ionized helium plasma at atomic density of 1×10^{20} cm^{-3}, taking Z=2, T_{eV}=250 eV, C~3eV/eV/atom, and $\ln\Lambda=4$, we have x=11.1 μm for a pulse duration of 1 ps. This is comparable to the beam waist radius of 15.8 in this case. For nitrogen at an atomic density of 2×10^{19} cm^{-3}, T_{eV}=350 eV, and Z=5, the heat diffusion distance is 9.6 μm. This is again comparable to the beam waist radius of 11.5 μm in this case. Thus the heat diffusion length is comparable to the plasma column width so that heat conduction should be important in reducing the temperature. However, since the collisional ionization rate is slow outside of the MPI ionized beam, it is expected that only partial ionization exists outside of the laser channel and the heat diffusion wave will have to penetrate into cold plasma with poor thermal conductivity. At the same time, from the above relations the diffusion length is proportional to the temperature to the 5/4 power. Thus a reduction in temperature by a factor of 2x will reduce the diffusion length by 2.4x making it significantly smaller than the beam radius. A 1D cylindrically symmetric hydro simulation for a neon plasma at a density of 3.5×10^{19} cm^{-3} heated by a 1 ps 268 nm laser pulse reported by Djaoui and Offenberger [6] showed a reduction of approximately 3 times in temperature due to heat conduction from a temperature of 1200 eV down to 400 eV. In that case the peak intensity was considerably higher at 4×10^{17} W/cm2 while the beam radius of 5 μm was considerably smaller than the present case. Overall it is expected that the actual temperatures will be lower than predicted in Fig. 9-14 by a factor of approximately 2.

The electron temperature has an important implication in the design of the recombination XUV lasers. For example, simulations by Burnett et al [10] show that to achieve high gains in H-like boron plasma on 3-2 and 2-1 transitions the electron temperature needs to be ~ 30 eV for an initial electron density of 10^{20} cm^{-3} or atomic density of $2.5x10^{19}$ cm^{-3}. Similarly for high gain in Li-like neon[10] electron temperatures of ~ 40 eV at an atomic density of $7x10^{19}$ cm^{-3} and an intensity of $3x10^{17}$ W/cm^2 are required. It is clear from Fig. 9-14 that because of collisional heating 1 ps KrF laser pulses can not achieve these required cold temperatures even if a factor of two reduction in temperature is included to allow for lateral thermal conduction. Recent measurements of temperatures in MPI heated neon plasmas by Blyth et al. [11] using 350 fs KrF laser pulses at an intensity of 10^{18} W/cm^2 would indicate temperatures of around 100 eV for gas densities of around $7x10^{19}$ cm^{-3} if one ignores the contribution of heating from the SRS instability which would not be a factor at a reduced intensity of $3x10^{17}$ W/cm^2. Thus, for electron densities of ~ 10^{20} cm^{-3}, laser pulses of 100 fs duration or shorter may be needed to produce a cold plasma.

Reference

1. E. E. Fill, J. Opt. Soc. Am. B 11, 2241 (1994).
2. S. Augst, D. Strickland, D. D. Meyerhofer, S. L. chin, and J. H. Eberly, Phys. Rev. Lett. 63, 2212(1989).

3. S. Augst, D. D. Meyerhofer, D. Strickland, and S. L. chin, J. Opt. Soc. Am. B8, 858(1991).
4. B. M. Penetrante and J. N. Bardsley, Phys. Rev. A43, 3100(1991).
5. S. Szatmari and F. P. Schafer, Opt. Comm. 63, 305 (1987).
6. A. Djaoui and A. A. Offenberger, Phys. Rev. E 50, 4961 (1994).
7. L. Spitzer, Physics of fully-ionized gases, Interscience, New York (1956).
8. F. J. Mayer, R. L. Berger, C. E. Max, Phys. Fluids 23, 1620 (1980).
9. N. H. Burnett and G. D. Enright, IEEE J. Quan. Electron. 26, 1797 (1990).
10. D. C. Eder, P. Amendt and S. C. Wilks, Phys. Rev. A 45, 6761 (1992).
11. W. J. Blyth, S. G. Preston, A. A. Offenberger, M. H. Key, J. S. Wark, Z. Najmudin, Phys. Rev. Lett. 74, 554 (1995).

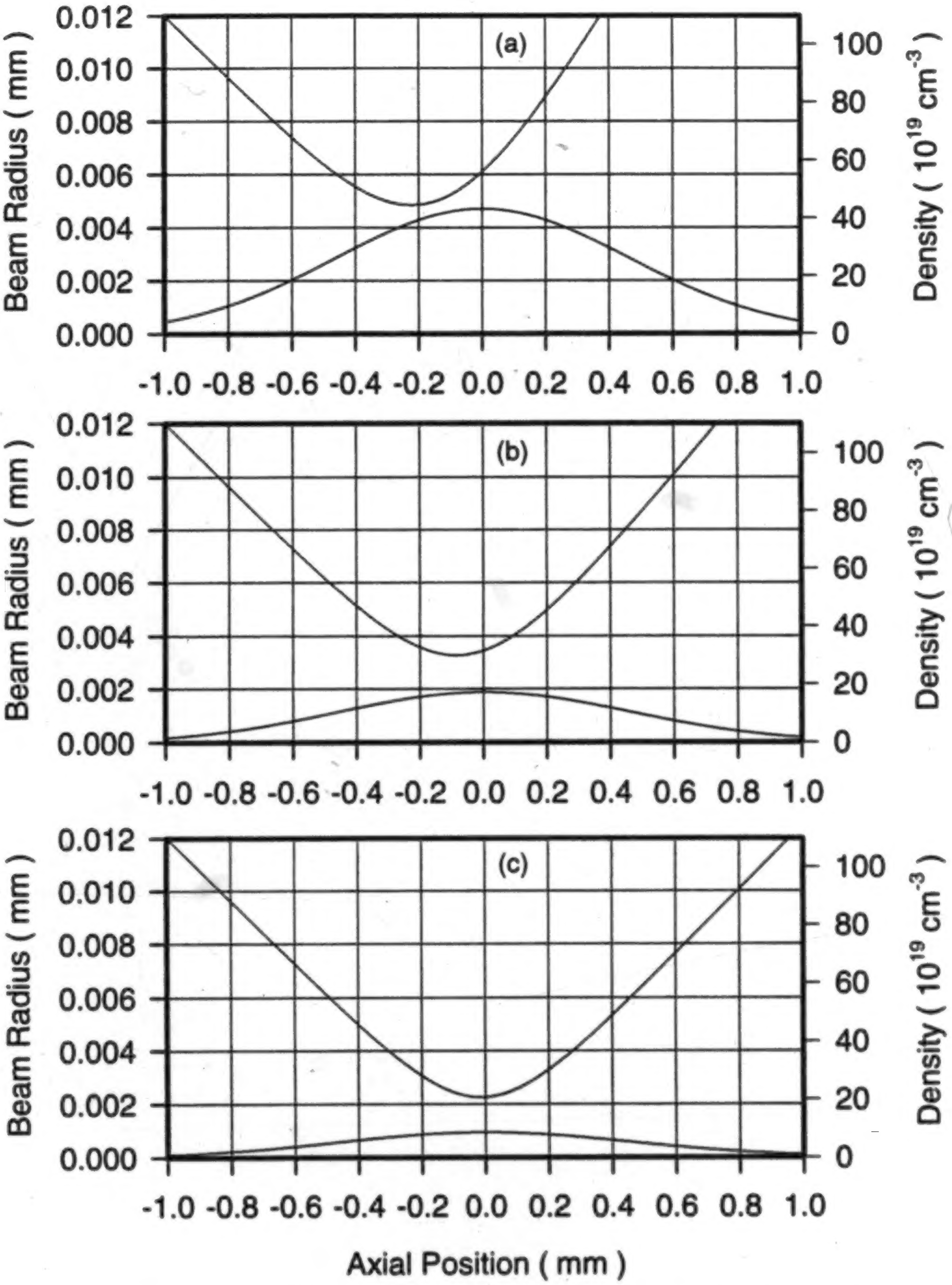

Fig. 9-1 Beam radius calculated as a function of axial position for a laser power of P=0.2 TW in a nitrogen gas jet target with peak atomic densities of (a) 5×10^{20}, (b)2×10^{20} and (c)1×10^{20} cm^{-3}. The outline of the gas jet density profile is also shown at the bottom of each plot for reference.

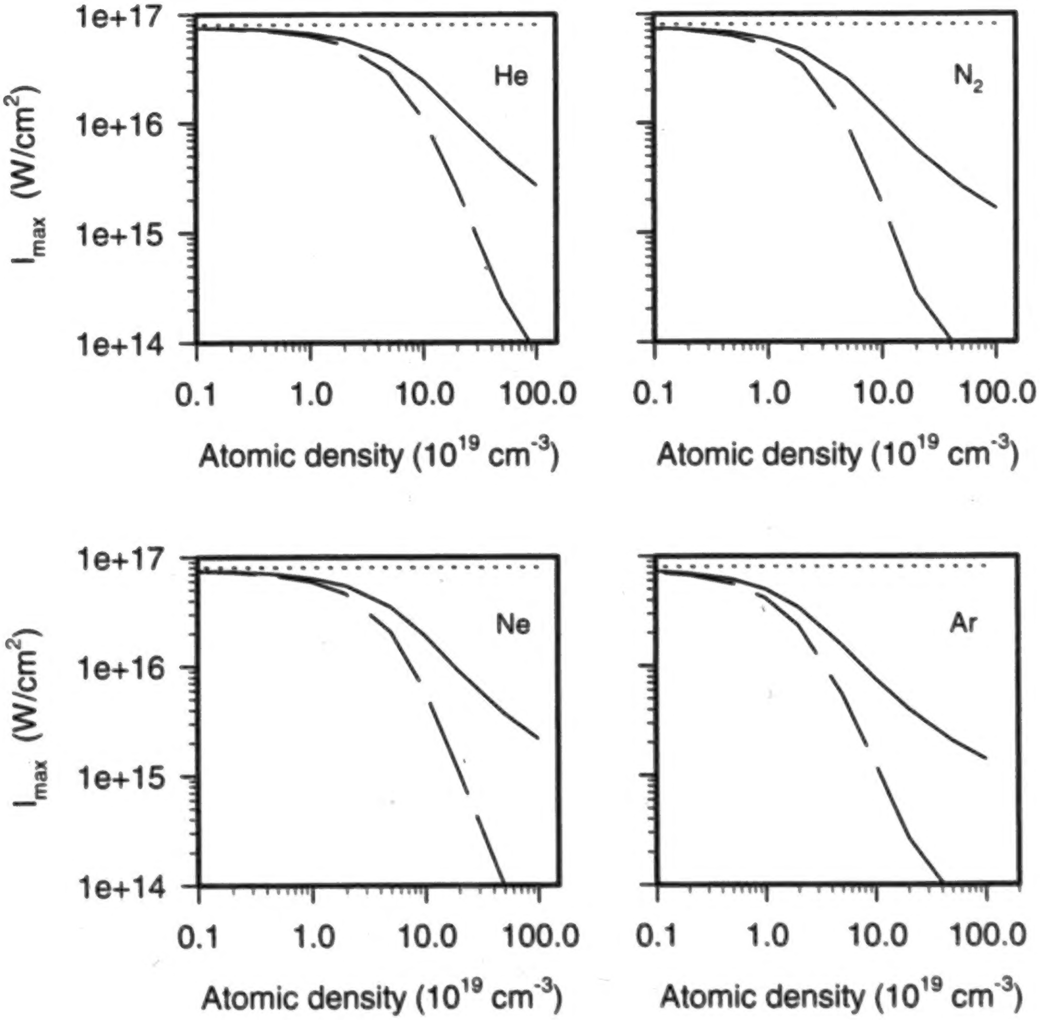

Fig. 9-2 Calculated peak intensities as a function of atomic gas jet density for a power of P=0.2 TW, an F/4.2 cone angle and a 9 μm vacuum focal radius for (a) helium, (b) nitrogen, (c) neon, and (d) argon. Also shown are the vacuum intensity (dotted line) and the peak intensity which would be achieved in a static gas target (dashed line).

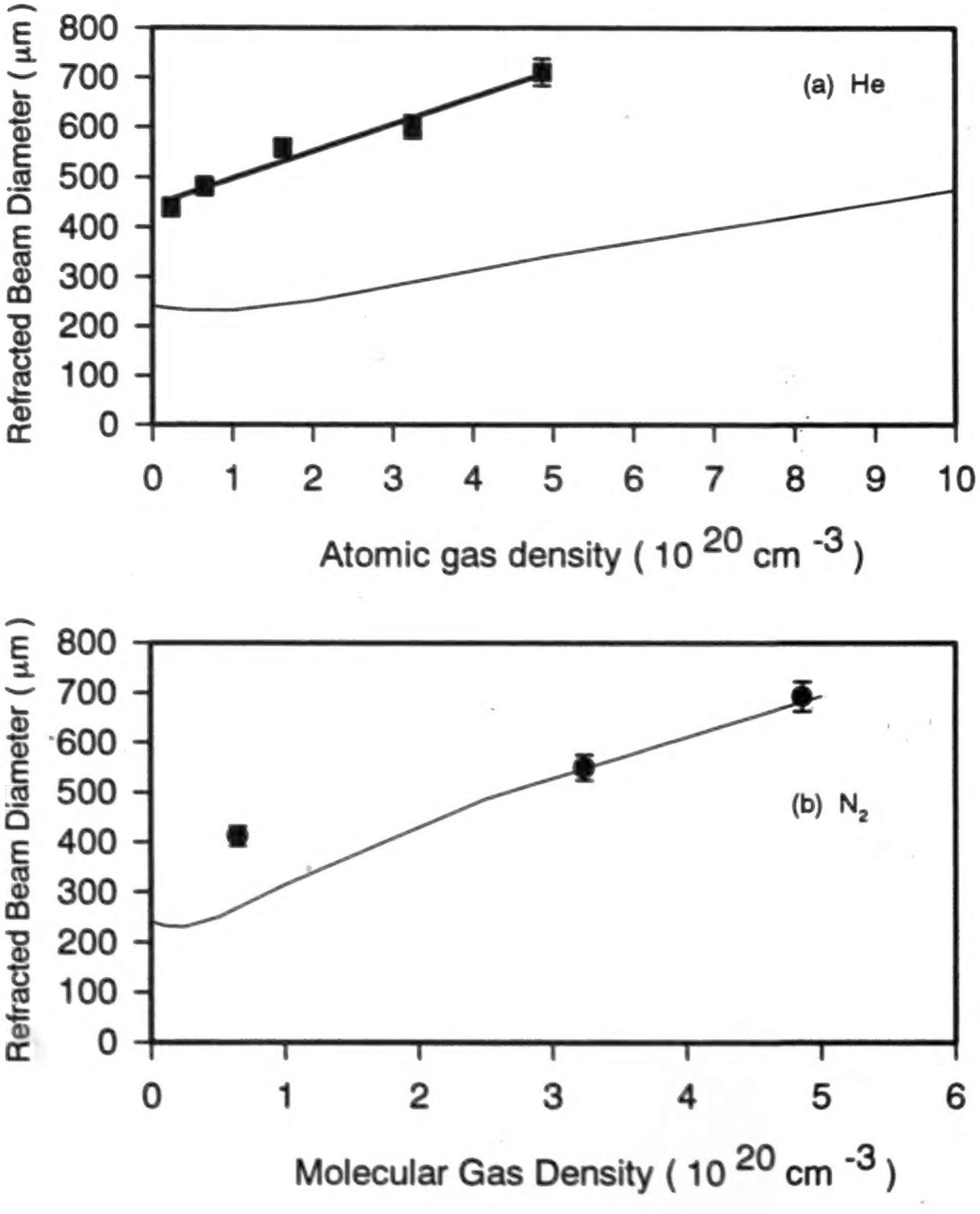

Fig. 9-3 Comparison of experimentally measured diameters of the outer refraction ring at the exit of the gas jet (solid symbols) with the calculated diameters (lines) for (a) He and (b) N_2.

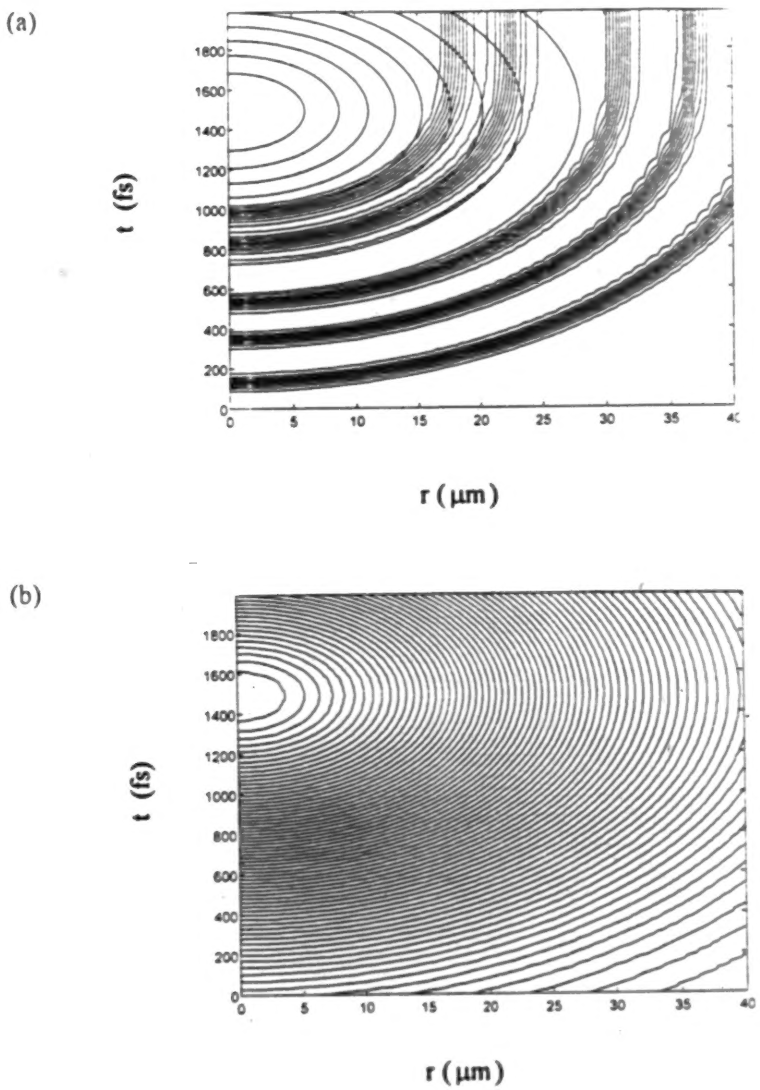

Fig. 9-4 Contour plot of average charge state as a function of position in the laser frame of reference in nitrogen gas for (a) ATI ionization based on Ammosov's rates and (b) the threshold ionization potential given by Eqn. 9.5. Intensity contours for the laser pulse are also superimposed in (a). The peak intensity is $3\text{x}10^{16}$ W/cm^2 at 1500 fs and the half intensity radius is 15 μm for a 1 ps pulse. Each contour represents a step of 0.1 in ionization stage.

(a) density profile

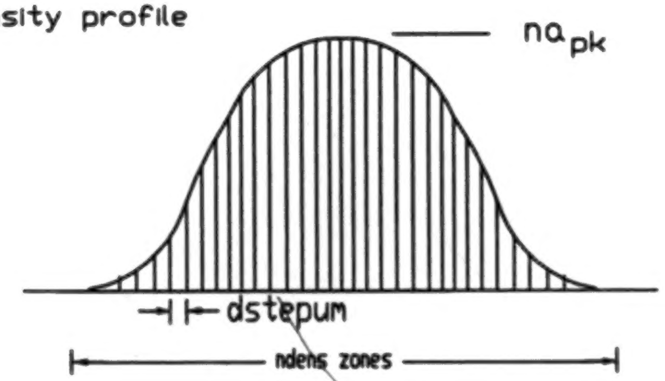
na pk
dstepum
ndens zones

(b) beam profile

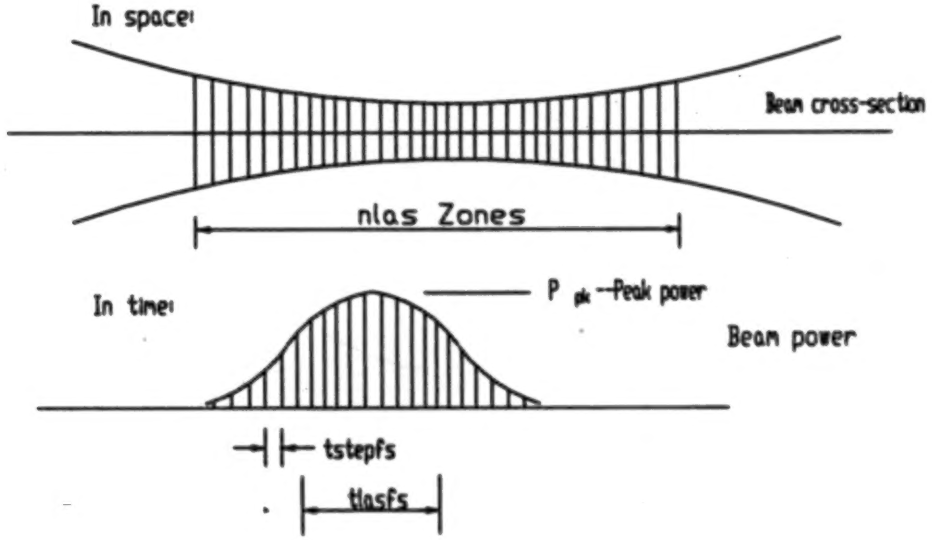
In space:
Beam cross-section
nlas Zones
In time:
P pk --Peak power
Beam power
tstepfs
tlasfs

Fig. 9-5 Geometry of 1D simulation. (a) density profile and (b) beam profile.

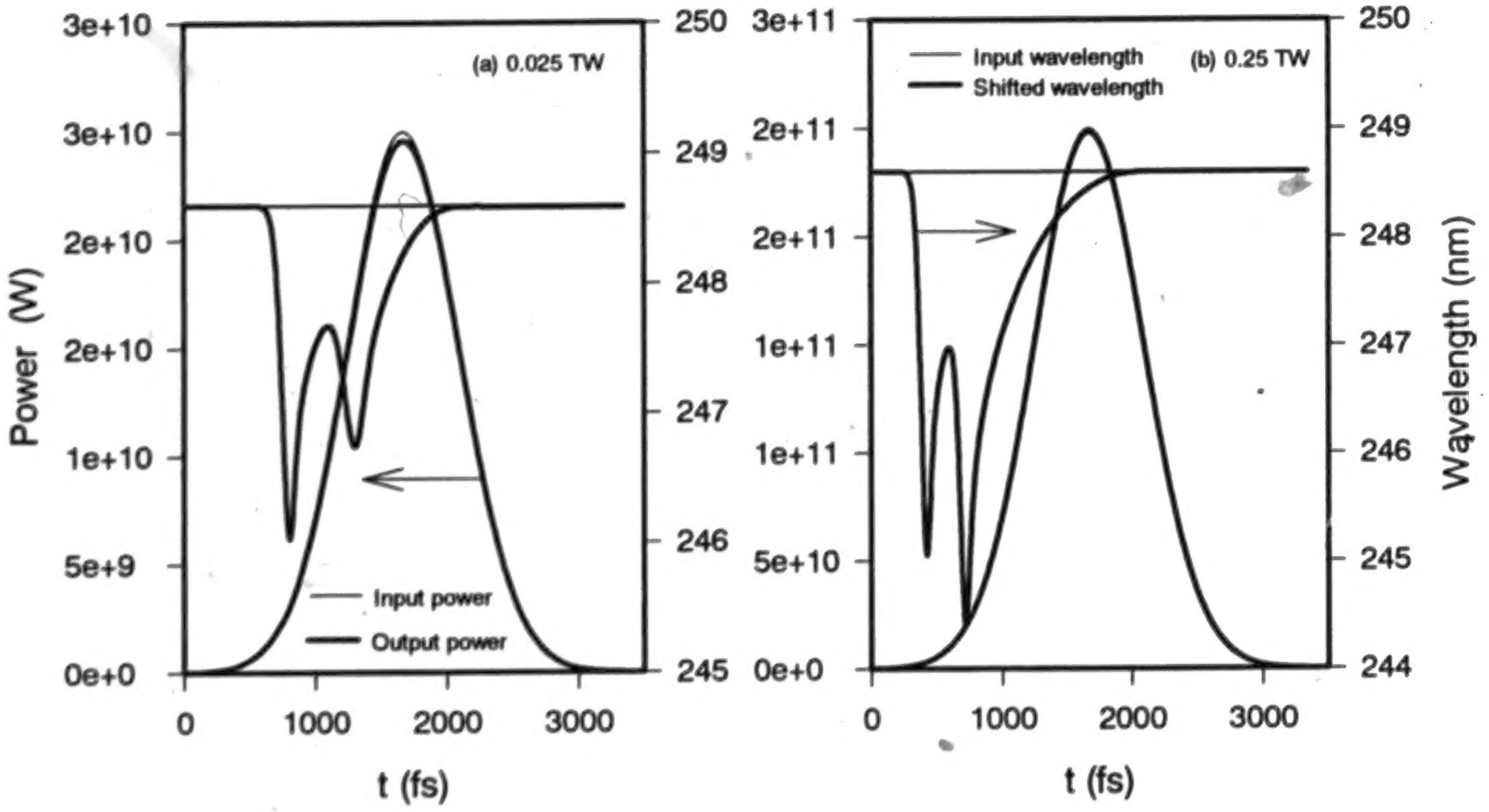

Fig. 9-6 Spectral blueshift for helium as a function of time for a density of $5\times10^{19}\text{cm}^{-3}$ and laser powers of (a) 0.025 TW and (b) 0.25 TW. Also shown is the input laser power and the laser power after absorption.

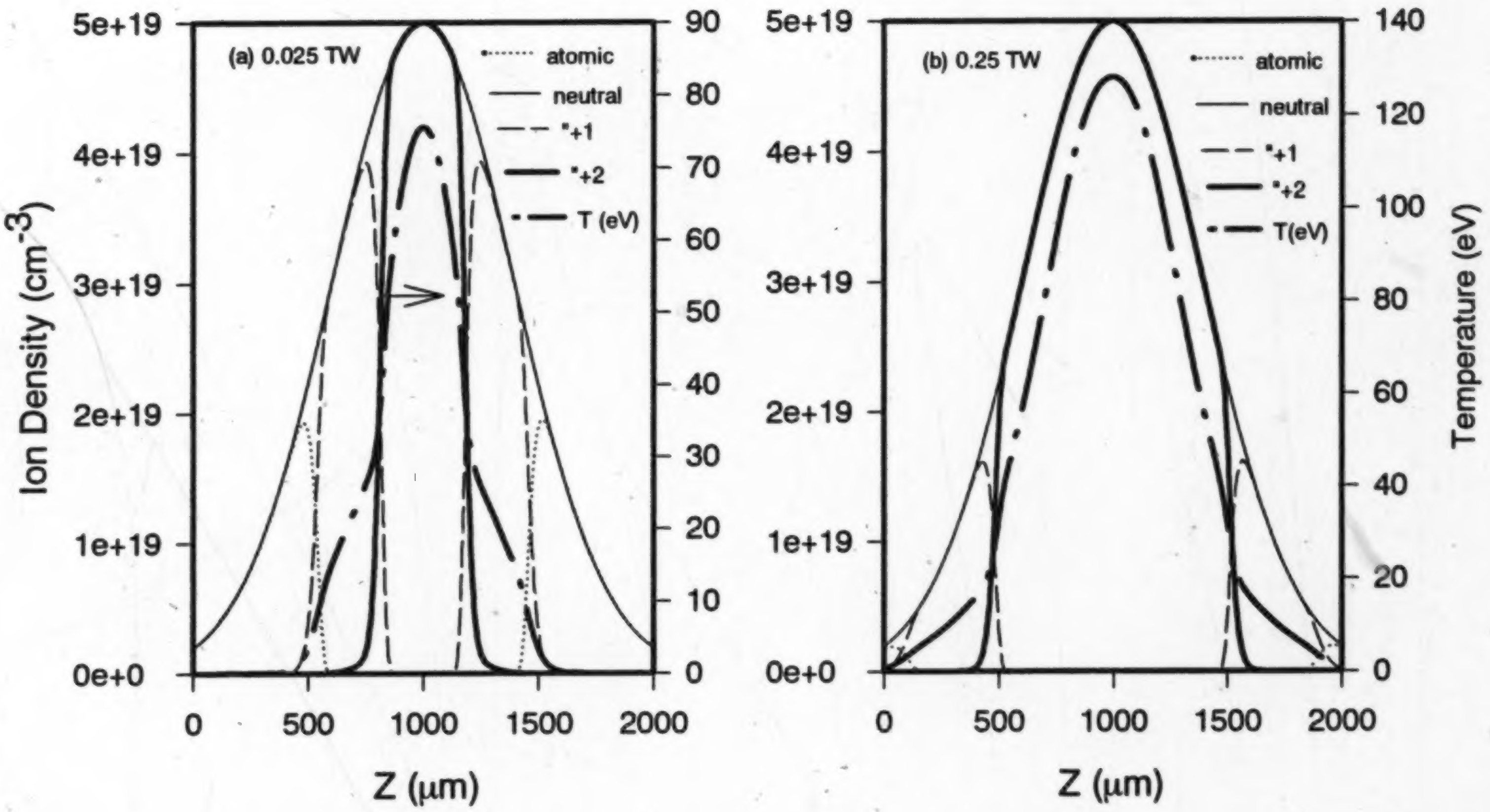

Fig. 9-7 Distribution of ionization states and electron temperature across the gas jet for helium at a peak density of 5×10^{19} cm^{-3} for peak vacuum powers of (a) 0.025 TW and (b) 0.25 TW.

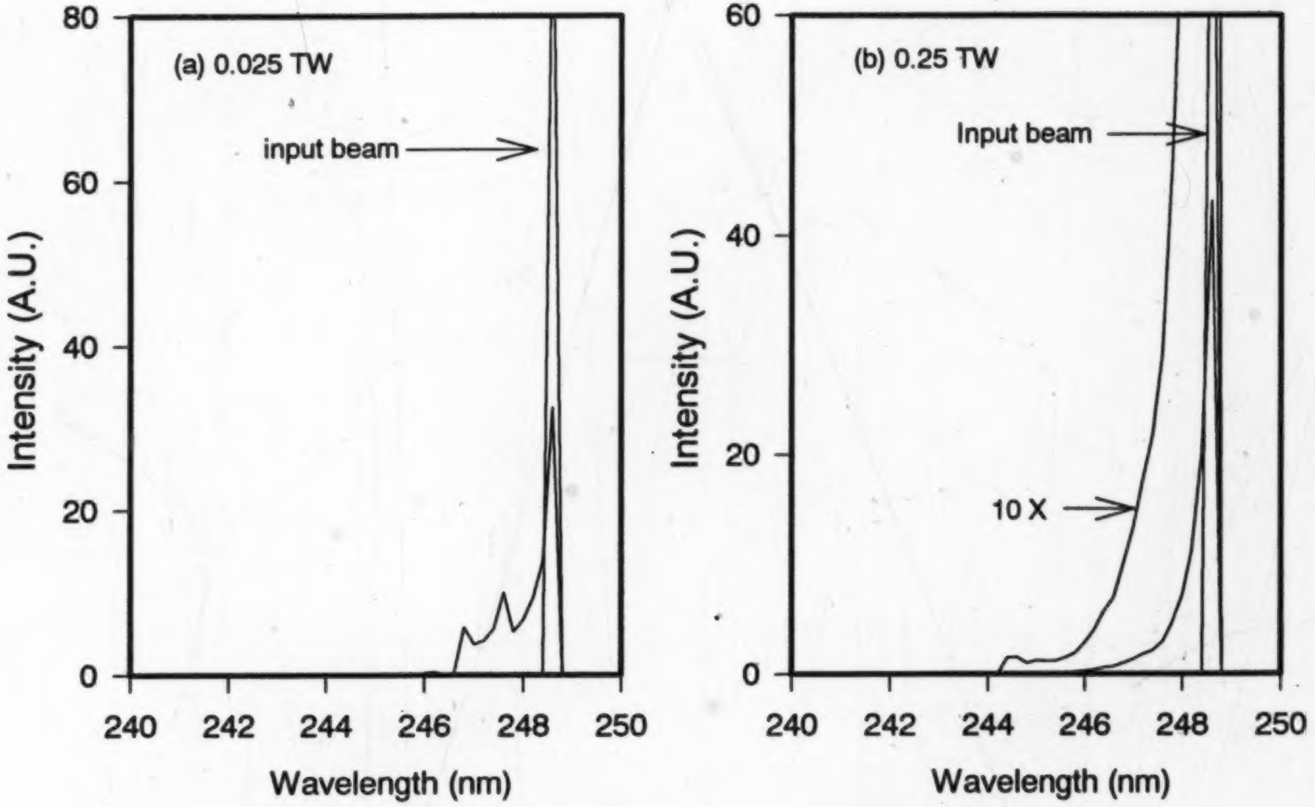

Fig. 9-8 Blue shifted spectrum for helium at a density of 5×10^{19} cm^{-3} for peak powers of (a) 0.025 TW and (b) 0.25 TW. Also shown is the input beam spectrum.

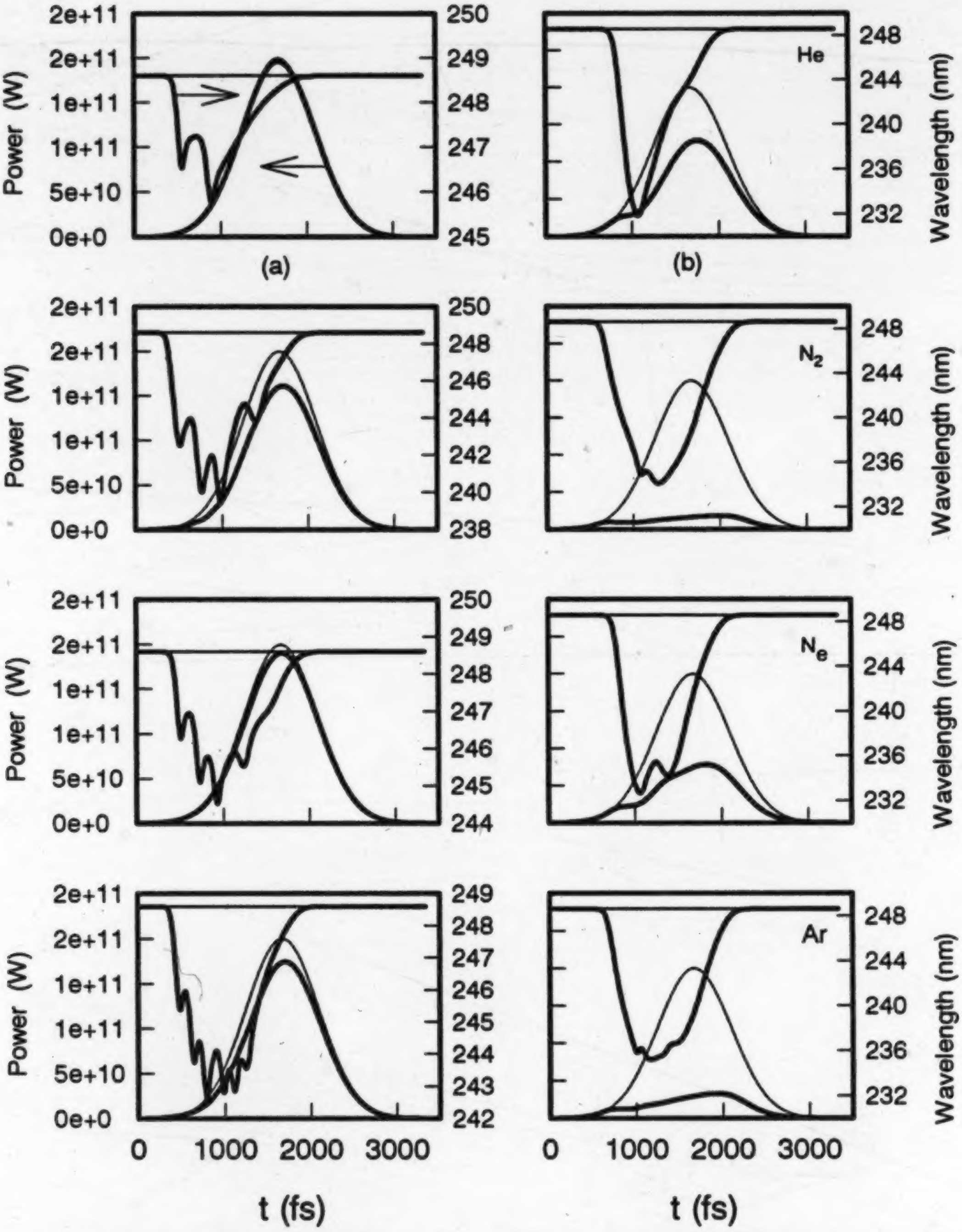

Fig. 9-9 Spectral blueshifts for He, N_2, Ne, and Ar as a function of time for a laser power of 0.2 TW at gas densities of (a) 5×10^{19}cm^{-3} and (b) 5×10^{20}cm^{-3}. Note that for N_2 it is molecular gas density. Also shown is the input power and the output laser power after absorption. Beam profiles calculated using the refraction model are used in these calculations.

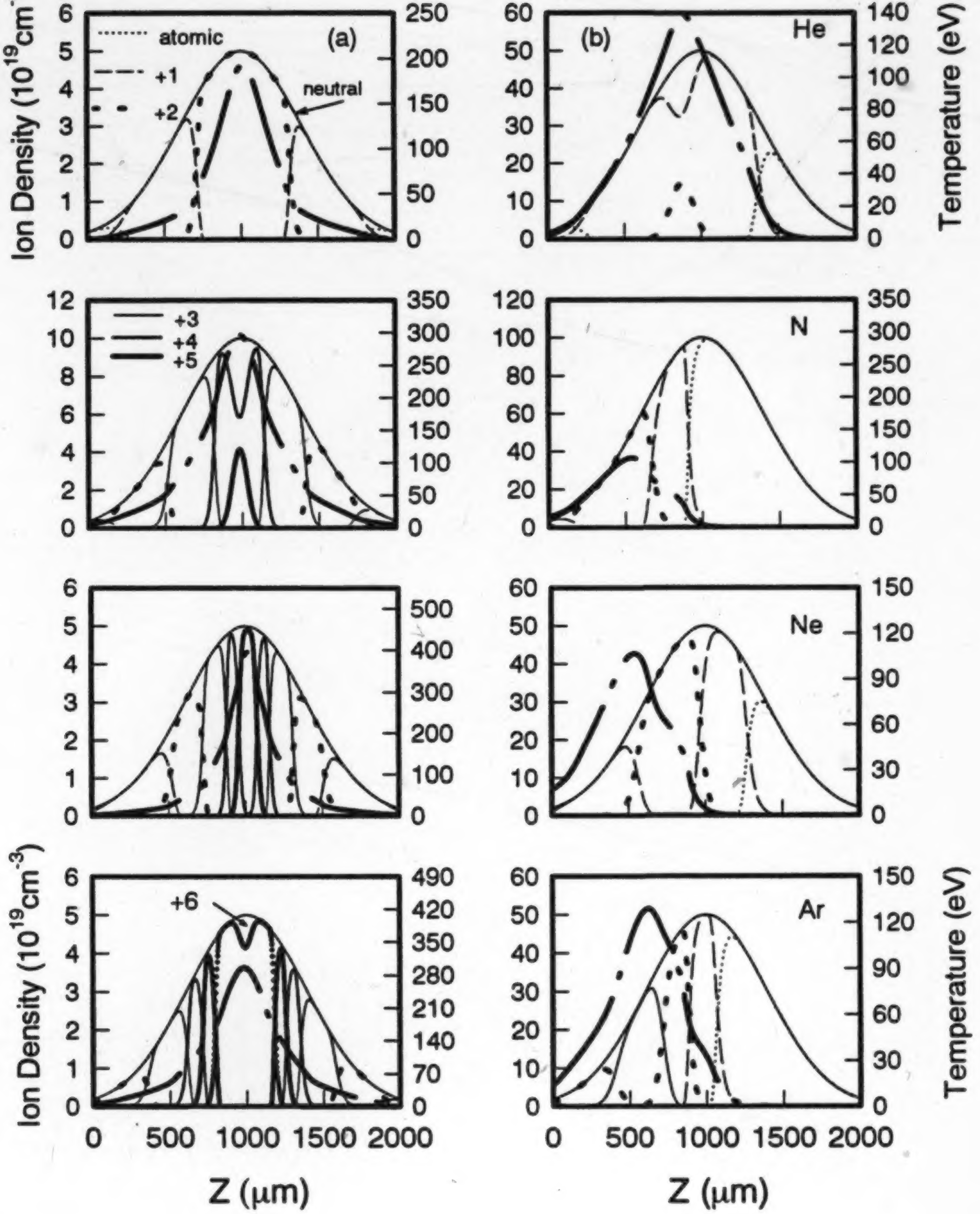

Fig. 9-10 Distribution of ionization states and electron temperature across the gas jet for a laser power of 0.2 TW at densities of (a) $5x10^{19}$ cm^{-3} and (b) $5x10^{20}$ cm^{-3} for He, N_2, Ne and Ar respectively.

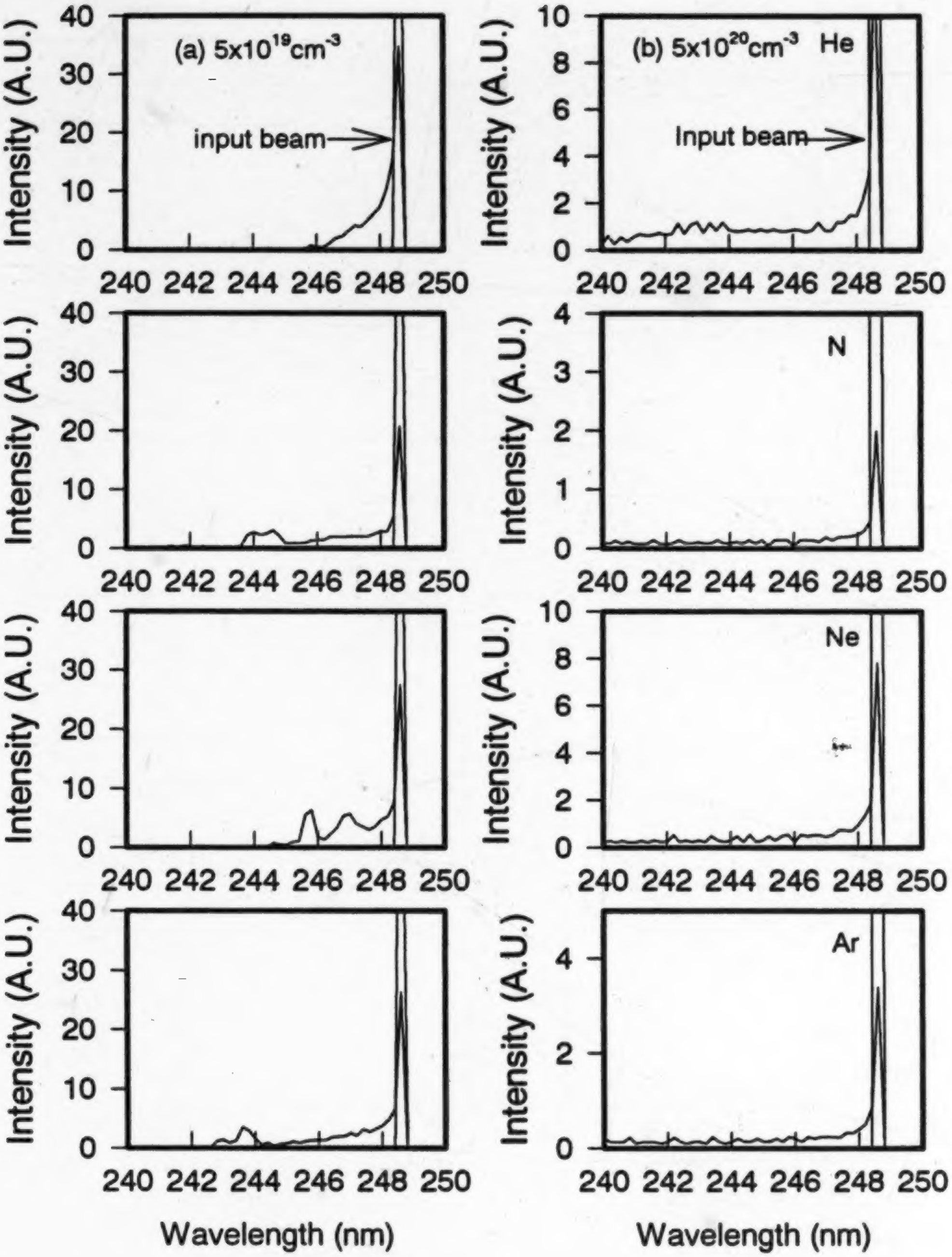

Fig. 9-11 Blue shifted spectrum for a laser power of 0.2 TW at densities of (a) $5x10^{19}cm^{-3}$ and (b) $5x10^{20}cm^{-3}$ for He, N_2, Ne and Ar respectively. Also shown is the input beam spectrum.

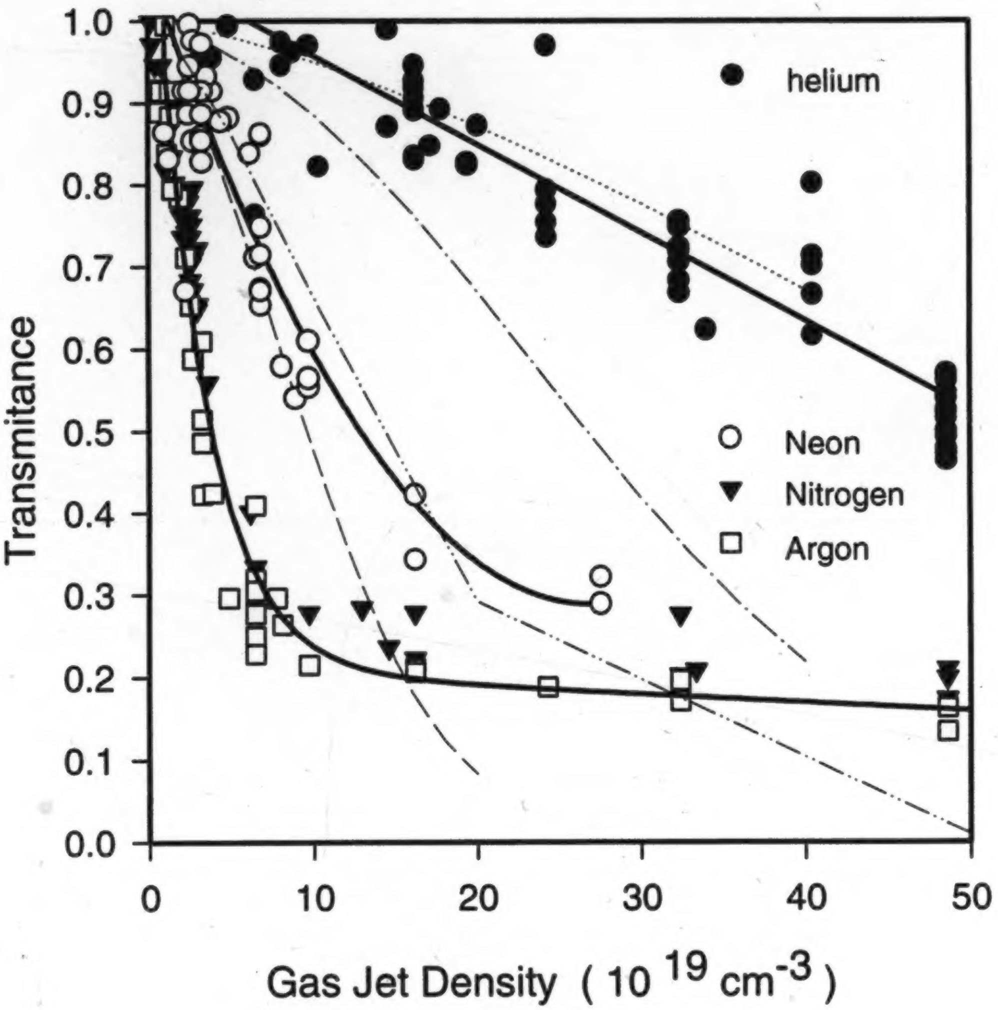

Fig. 9-12 Calculated energy transmission of KrF laser pulses through

········ He, —·— Ne, — — N_2, and —··— Ar

as a function of density using the experimentally measured beam profile as shown in Fig. 7-2 for a laser power of 0.02 TW (i.e. an effective intensity 10 times reduced from the vacuum intensity). Also shown are the measured transmission data as in Fig. 7-25. Note that for nitrogen the molecular density is used.

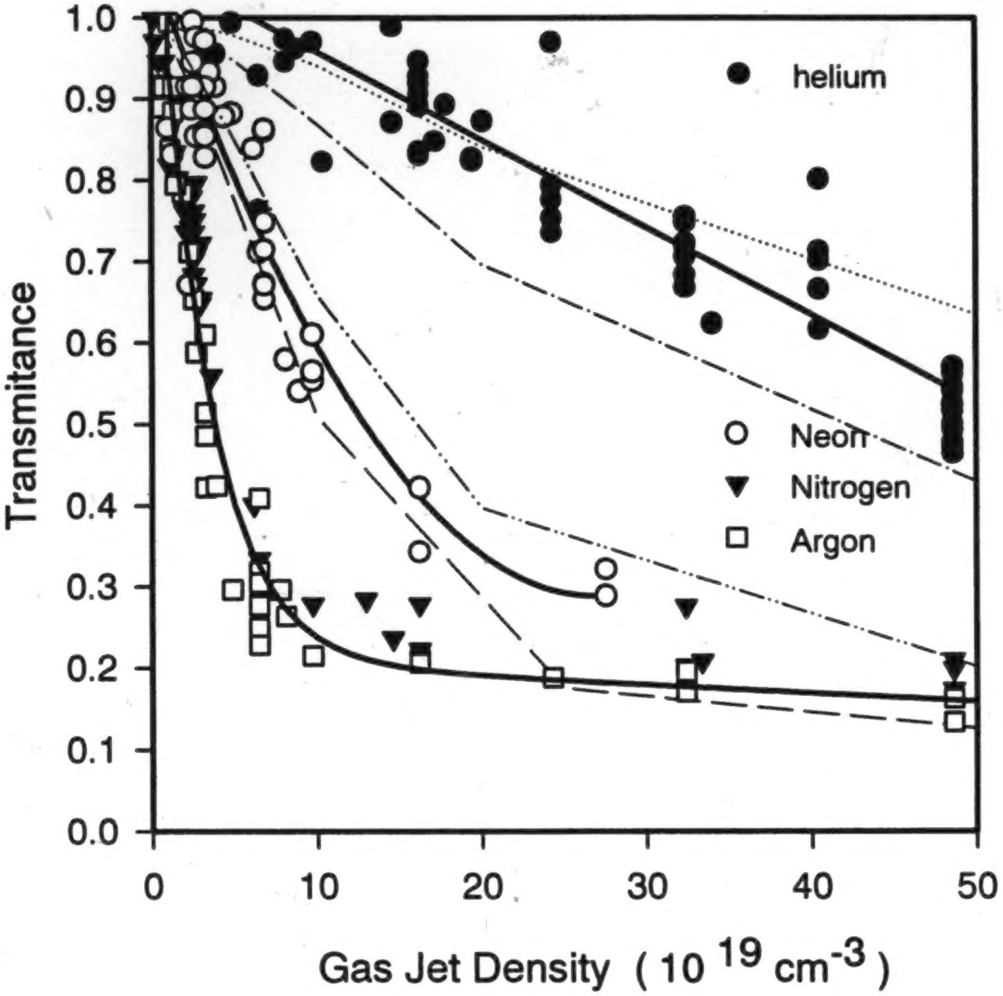

Fig. 9-13 Calculated energy transmission of KrF laser pulses through ········ He, —·— Ne, — – N_2 and —··— Ar as a function of density using the calculated beam profiles similar to Fig. 9-1 for a laser power of 0.2 TW. Also shown are the measured transmission data as in Fig. 7-25.

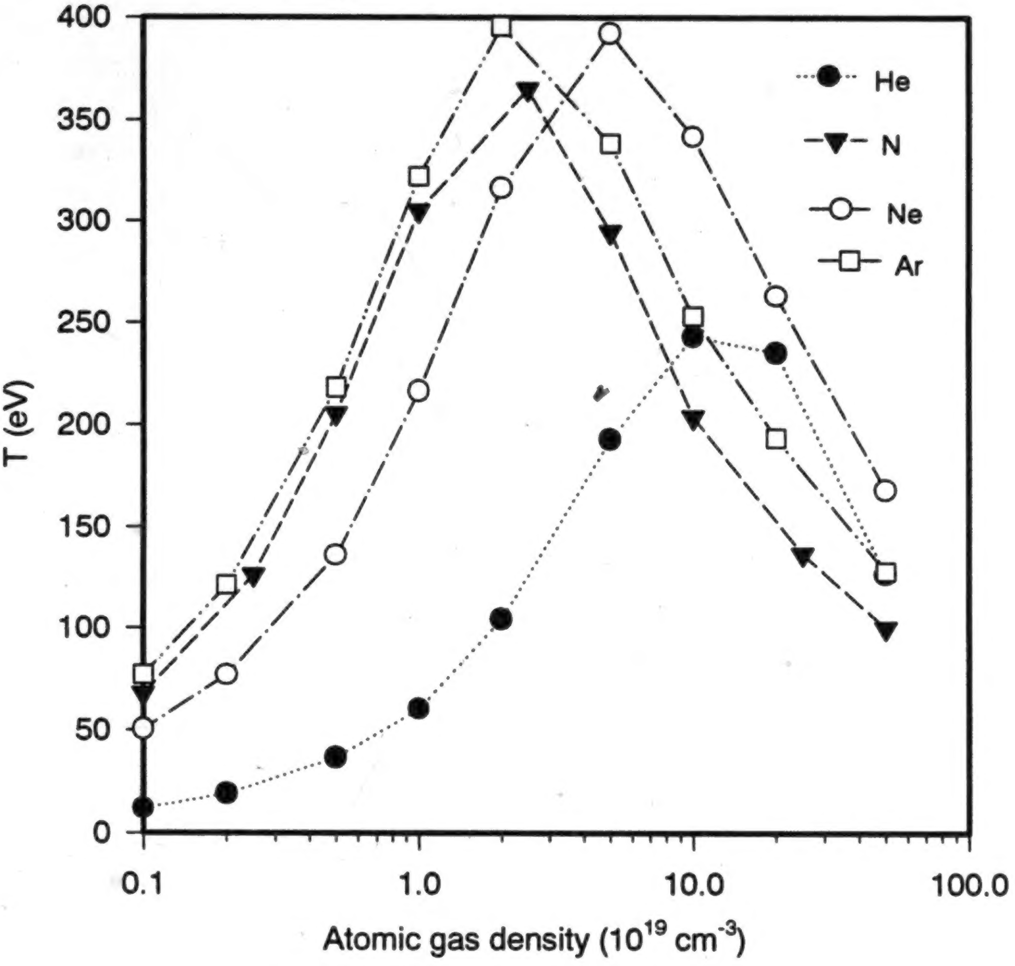

Fig. 9-14 Calculated electron temperature as a function of gas density for P=0.2 TW with the same conditions as in Fig. 9-13. Note that for nitrogen molecular gas density is used.

Chapter 10

Conclusion

A comprehensive study of the formation of high density plasma columns by means of above threshold ionization of gaseous medium and the propagation of ultrashort KrF laser pulses through such plasmas has been carried out. The investigations have employed various diagnostics including time-resolved shadowgraphy, energy balance, CCD imaging of the refracted laser beam, spectral measurements of the He II emission line, and recording of the blue shifted laser spectra. An autocorrelator was developed to characterize the KrF laser pulses using the visible fluorescence of BaF_2 and a high density gas jet was developed and characterized for the target experiments.

The formation of plasma columns via multiphoton ionization in a static gas target of either argon, helium and air was studied using 5 mJ, 6 ps KrF laser pulses focused by an f/10 lens. The results were in agreement with multiphoton ionization initiated breakdown with subsequent collisional ionization and evolution of a 400-900 μm long cylindrical blast wave channel. Such a blast wave channel would make a good guide channel for subsequent short pulses as has recently been demonstrated by Milchberg and coworkers. Refraction of the laser pulses in the static fill gas cell was identified as a limitation to achieving high intensity at the focus and obtaining long plasma channels.

A high density gas jet was developed in order to reduce the refraction of the laser pulse prior to reaching its high intensity focus. The spatial density profile of the gas jet was characterized using laser interferometry and Abel inversion of the fringe profiles. Gas densities of up to 6 x 10^{20} cm^{-3} at a distance of 200 μm above the nozzle tip were measured.

A single shot autocorrelator based on the two photon fluorescence spectra of KrF laser radiation in BaF_2 was developed and characterized to measure the subpicosecond pulsewidth . For the first time the visible fluorescence was characterized and used rather than the UV emission which previously had been used. The quadratic dependence of the fluorescence intensity on the exciting laser intensity was verified for the wavelength around 400 nm. The autocorrelator based on visible emission had a temporal resolution of 100 fs with the present optics. With optimum adjustment of the KrF laser, a pulse width of 850 fs was measured. A novel method using the fluorescence emission intensity was used to measure the two photon absorption coefficient of BaF_2, giving a coefficient of $1.3 \pm 0.4 \times 10^{-10}$ cm / W .

The study of the interaction of a picosecond high intensity (10^{17} W/cm^2 in vacuum) KrF laser pulse with the high density gas jet led to a number of key results. These results were compared to model calculations of beam refraction due to the ionization induced electron density profile and of the ionization and heating dynamics of the pulse propagating through the gas jet. In addition, the ionization induced blue shift was calculated in the modeling code.

CCD camera images taken at the exit of the gas jet gave output spot diameters of 500 to 700 μm in diameter and estimated refraction half angles of 15^0 to 20^0 for helium and nitrogen gas jet targets with gas densities of 0.5 to 5.0×10^{20} cm^{-3}. The refraction can be explained primarily in terms of the ionization induced refraction in the leading edge of the laser pulse. However, the peak intensities and densities achieved in the present experiment would lead to less than one growth length for ponderomotive filamentation which should not contribute significantly to the observed spreading of the beam. However, the scattering angles predicted by pondermotive filamentation would be comparable to the measured angles. In addition, a central bright spot was observed at the exit of the gas jet which could be indicative of some self focusing of the tail part of the incident laser pulse which would not suffer as much ionization induced refraction as the leading edge of the pulse. Detailed 2D simulations will probably be required in order to clearly identify mechanisms for this central bright spot.

Energy measurements made in an F/2.5 transmission cone angle indicate a rapid drop in transmission as a function of density for nitrogen and argon, a slower drop for neon and a much slower drop for helium. The reduction in transmission is much greater than would be expected from absorption from ionization alone which typically would be few percent for helium and on the order of 10% for the higher Z gases. From the modeling calculations it is clear that even with high field corrections there is significant IB heating of the plasma leading to a large absorption fraction and a large temperature rise in the more intense portion of the interaction. The remaining difference between the calculated transmission and measured transmission can be accounted for by refraction outside of the collection cone angle.

Additional imaging diagnostics viewed the plasma at 90^0 to the direction of propagation. The main diagnostic involved imaging onto a CCD camera using a narrow band filter with a center wavelength of 468.5 nm (the 4-3 transition of He II) and thus images of the highly ionized helium plasma regions could be recorded. These images revealed a larger diameter blast wave region in the first half of the gas jet corresponding to the enhanced heating which occurs in the refraction created beam waist region before the middle of the gas jet. Spectroscopic measurements were also made in the region of the He II line at 468.5 nm. These were measured in three directions viewing the entrance, middle and exit of the gas jet target. The spectra revealed strong emission of this He II line and little emission of the neighboring He I line at the entrance to the gas jet target while almost equal emission for the He II and He I lines are obtained at the exit of the gas jet target. This agrees with the conclusion that strong refraction leads to a reduced intensity at the exit of the gas jet.

In conclusion the formation of high density plasma columns by means of optical field ionization of gaseous medium and the propagation of ultrashort KrF laser pulses through such plasmas has been experimentally studied for both a static fill gas cell and in a high density gas jet. The measurements for the absorption, scattering, refraction, and ionization induced blue shifting in such plasmas provide better insight into the picosecond laser plasma interaction and plasma dynamics. The use of gas jet targets in the present experiments has allowed the study of high intensity interaction in a new regime where $\upsilon_{osc}/\upsilon_{th} > 1$ at electron densities of up to 0.1 n_c and laser intensity up to 10^{16} W/cm^2 for picosecond KrF lasers. However, at these high densities the peak achievable intensity is reduced by up to an order of magnitude or more from its vacuum value. Such intensities achieved in the gas jet are still an order of magnitude higher than could be achieved in a static gas cell.

It is clear that guiding plasma channels will be essential for the formation of long scale length high intensity interaction regions. At the same time, the results are in agreement with model calculations showing significant heating of the plasma up to several hundred electron volts for the higher Z gas cases. These temperatures are clearly much too high for XUV recombination laser schemes and indicate that shorter pulses, on the order of 50 fs in duration and lower interaction densities will be required in order to maintain the cold temperatures required for XUV lasers. It is hoped the results can be used for comparison with detailed numerical studies in future to further understand the physics of the laser plasma interaction and will be useful for the investigation of XUV lasers and inertial confinement fusion research.